

# Development of Ferromagnetic Metallic Glasses into Low Loss Power Transformer Cores

Thesis by  
Michael Floyd

In Partial Fulfillment of the Requirements for the  
degree of  
Doctor of Philosophy

CALIFORNIA INSTITUTE OF TECHNOLOGY  
Pasadena, California

2018  
Defended 29 September 2017

© 2018

Michael Floyd

All rights reserved

To Sarah

## ACKNOWLEDGEMENTS

First of all, I would like to thank Professor William Johnson for guiding me as my advisor during my time at Caltech. Professor Johnson has been a constant during my graduate career, always inspiring me with his own enthusiasm and motivating me to study more so that I can understand a tenth of what he does. Bill has always been there with his office door open, allowing me to ask him questions about problems I am having and allowing me to listen to him describe the most recent bit of theory he is trying to come up with. I came to Caltech to work with Bill and I have loved every moment of being in his lab.

To offer a balance to all of Professor Johnson's sage advise and theoretical ideas, Dr. Marios Demetriou has been there for me as a guiding hand and mentor. Marios has been there for me from the first day I volunteered in the lab to the writing of this thesis. He has helped me to grow as an experimentalist and as a scientist; guiding me through my research projects and pushing me to always do more. While Bill has constantly inspired me to learn more, Marios has always helped me to overcome the problems I encounter and offer me advise on how to continue.

I would like to thank all of the members of the Johnson group. Andrew Hoff has often been the sole group member that is around, meaning that he is the one I have turned to when the equipment stops working or I have a random idea that I want to bounce off of someone. Thank you for getting me to go to all the networking events and career fairs, that motivation helped me to finish up my work here at Caltech. Dr. Georg Kaltenboeck taught me much about the processing of metallic glasses, and helped me to first understand the aspects of magnetism in my project. I'd like to thank Joanna Kolodziejska, who helped me navigate the pitfalls of TAing APh 105, as well as for showing continued interest in my projects and progress. Thank you to Dr. Doug Hofmann, and Dr. Scott Roberts, whose work at JPL has

inspired me to think of all the possible applications of metallic glasses. Thanks to Dr. Xiao Liu, who did the ground work on my project, enabling me to have a clear path and scope for my project. I would like to also thank Pam Albertson, for ensuring that all my orders were paid and that all the grant money was coming in. And lastly, from the Johnson group, I would like to thank Dr. Dale Connor for being around and always being willing to listen.

I would like to thank the visiting scientists to the group as well, specifically Prof. Konrad Samwer and Prof. Marc Nicolet. They have stayed in our group for many months at a time and I was lucky to have them around to broaden my perspective and understanding.

I would like to thank some of the other groups on campus, specifically the Goddard group, the Fultz group, and the Faber group, all three of which have helped me either through collaboration, use of their equipment, or through talking with them about research ideas.

I would like to thank everyone at Glassimetal Technologies, especially Dr. Joe Schramm, Dr. Glenn Garrett, and Dr. Jong Na. Working with them inspired me to get a PhD in the first place, and their continued advise helped me as I progressed. I would also like to thank Dr. Na for providing the material for my wedding bands.

I would like to thank my thesis committee as well, Professor Julia Greere, Professor Kathy Faber, and Professor Keith Schwab. The time that they have dedicated to helping me publish this thesis and graduate from Caltech has been indispensable.

Many of the experiments that were carried out would have been impossible without Dr. Yunibin Guan and Darryl Witherbee. Their expertise in SIMS and EDM allowed my experiments to be carried out, and often helped out when I showed up at a moments notice.

I would like to thank Sarah for being there through the thick and thin of my

time as a graduate student. Every day, she would listen to the inane things which occurred in lab, even though I know she could care less about how I spent 4 hours trying to fix a vacuum pump. Sarah is my motivation for all that I do, and without her I would have become lost many times in the last four years. Thank you for helping me to stay motivated, and for distracting me when I needed to not stress over things so much. I know I can count on you as I move on to my next endeavor.

My parents have always been there for me, and their support has meant a lot to me. They have let me stay with them when I needed a place to sleep, fed me when I've needed a meal, and supported me in everything that I have done. Their love and support has been constant, and has helped me as I've worked on my PhD. My brother and sister have also been very supportive of me, while also making sure I never get too full of myself.

Thanks to Dylan Tozier for being with me throughout my career at Caltech, from visiting days to my thesis defense. Dylan has grounded me with lots of video games, trips to the Huntington Gardens or the Rathskeller, and weekly lunches. Dylan has made my time at Caltech truly enjoyable.

I would also like to thank all my other friends at Caltech, especially Nick, Nate, and Andrew. They were a lot of help when we all were struggling through classes our first year and for prepping for candidacy during our second. They have been steadfast friends and I will be sorry to no longer be around them.

This research was supported by the IIVI Foundation and by the Global Power Technology Group. I would lastly like to thank Dr. Carl Johnson, who believed in our work and ensured that we kept our funding throughout the project.

## ABSTRACT

Currently, 3% of energy losses in the U.S. electrical grid occur at power transformers. With a transition to Metglas, transformer efficiency could be increased, but is Metglas the best replacement material for power transformers?

With this in mind we develop a Fe-based metallic glass for its glass forming ability and soft magnetic properties. During this development we identify a redox reaction of boron oxide by Si during melt fluxing of the Fe-based glass, which promotes an unexpected exchange of Si and B in the alloy. Taking this reaction into account, a unique optimization strategy is implemented, enabling oxide purification of the melt coupled with a significant but predictable shift in composition. This leads to an optimized Fe-based glass demonstrating a global peak in glass forming ability. Following boron oxide fluxing in the high temperature melt, alloy with composition  $\text{Fe}_{57.5}\text{Co}_{20.2}\text{Si}_{10.2}\text{B}_{2.05}\text{P}_{10.05}$  transforms to  $\text{Fe}_{57}\text{Co}_{19.2}\text{Si}_{6.8}\text{B}_{7.4}\text{P}_{9.6}$ , and increases its critical rod diameter from 1 mm to 5 mm. The alloy also demonstrates excellent soft ferromagnetic performance characterized by a magnetic saturation of 1.53 T.

While developing the above alloy, we also analyzed the effect of varying thickness of a  $\text{Fe}_{68}\text{Mo}_4\text{Ni}_3\text{Co}_5\text{Si}_1\text{P}_{11.5}\text{C}_5\text{B}_{2.5}$  transformer core as a function of frequency to discover if there was a minimum in the losses. We did not find a single minimum, but found that the optimal thickness exhibits a logarithmic dependency on frequency. This dependence suggests the optimal thickness of a core ranges from 100 – 400  $\mu\text{m}$ , instead of in the < 50  $\mu\text{m}$  range currently used. These larger optimal thicknesses are unexpected if anomalous losses are not considered, but the dominance of the anomalous losses at low frequencies, or for thin samples, validates the need for thicker power transformers. While other amorphous metals and casting techniques will yield varying results, the logarithmic dependence on frequency and the 100 – 400  $\mu\text{m}$  optimal thickness range should be broadly applicable.

## PUBLISHED CONTENT AND CONTRIBUTIONS

- [1] J.H. Na, M. Demetriou, M. Floyd, A. Hoff, G. Garrett, and W.L. Johnson. “Compositional landscape for glass formation in metal alloys”. In: *Proc. Natl. Acad. Sci.* 111 (2014), pp. 9031–9036. doi: 10.1073/pnas.1407780111.

Michael Floyd participated in the conception of the project, manufactured the specimens for testing, analyzed the compositional variance in GFA, and carried out secondary data analysis.

- [2] J.H. Na, M. Floyd, D. Lee, M.D. Demetriou, W.L. Johnson, and G. Garrett. *Melt Overheating Method for Improved Toughness and Glass-Forming Ability of Metallic Glasses*. US Patent US 2014/0202596 A1, 7/24/14.

Michael Floyd developed the initial hypothesis, participated in the conception of the project, and carried out the experiments to determine the critical temperatures.

## TABLE OF CONTENTS

Acknowledgements . . . . .	iv
Abstract . . . . .	vii
Published Content and Contributions . . . . .	viii
Table of Contents . . . . .	ix
List of Illustrations . . . . .	xi
List of Tables . . . . .	xvi
List of Equations . . . . .	xvii
Nomenclature . . . . .	xix
Chapter I: Introduction . . . . .	1
1.1 Overview of Metallic Glasses . . . . .	1
1.2 Alloy Development . . . . .	10
1.3 Magnetics and Metallic Glasses . . . . .	17
1.4 Review of Past Work on Ferromagnetic Metallic Glasses . . . . .	29
1.5 Key Contributions . . . . .	34
Chapter II: Alloy Development of a Fe-based metallic glass with excellent soft ferromagnetic properties . . . . .	36
2.1 Abstract . . . . .	37
2.2 Introduction . . . . .	38
2.3 Method . . . . .	43
2.4 Results . . . . .	44
2.5 Conclusion . . . . .	53
Chapter III: The affect of boron oxide flux, B <sub>2</sub> O <sub>3</sub> , on glass formation and properties . . . . .	54
3.1 Abstract . . . . .	54
3.2 Introduction . . . . .	56
3.3 Materials and Method . . . . .	58
3.4 Results . . . . .	59
3.5 Conclusion . . . . .	69
Chapter IV: Processing and machining of cores for magnetic testing . . . . .	70
4.1 Injection Molding . . . . .	71
4.2 Stress Annealing . . . . .	75
4.3 Electric Discharge Machining . . . . .	81
4.4 Magnetic Measurements . . . . .	83
4.5 Magnetic Annealing . . . . .	87
Chapter V: Minimizing Losses in Ferromagnetic Metallic Glass Cores . . . . .	90
5.1 Abstract . . . . .	90
5.2 Introduction . . . . .	91
5.3 Methods . . . . .	93
5.4 Results . . . . .	94

5.5 Conclusion . . . . .	103
Chapter VI: Conclusion and Continuation of this Thesis . . . . .	104
6.1 Conclusion . . . . .	104
6.2 Development of Amorphous, Ferromagnetic Wires . . . . .	106
6.3 Mechanics of Fe-based metallic glasses . . . . .	109
6.4 Modeling of Losses . . . . .	111

## LIST OF ILLUSTRATIONS

<i>Number</i>	<i>Page</i>
1.1 X-Ray Diffraction scan of an amorphous metal. . . . .	2
1.2 TTT-diagram of the cooling path required for a molten alloy to become a metallic glass. . . . .	3
1.3 The rate of change in volume differs between "phases". . . . .	5
1.4 Differential scanning calorimetry scan of a metallic glass. The glass transition temperature ( $T_g$ ), crystallization temperature ( $T_x$ ), solidus temperature ( $T_s$ ), and liquidus temperature ( $T_l$ ) are identified by arrows. . . . .	6
1.5 Binary eutectic phase diagram, displaying a eutectic composition. This eutectic composition is characterized by a minimum in the liquidus. . . . .	12
1.6 Cusp in the glass forming ability of a Ni-based metallic glass as the boron concentration is varied following this formula, $\text{Ni}_{69}\text{Cr}_{8.5}\text{Nb}_3\text{P}_{19.5-x}\text{B}_x$ [27]. . . . .	14
1.7 Island in the glass forming ability of an Ni-based glass. GFA varies with both the chromium concentration and the niobium concentration [27]. . . . .	16
1.8 Fe-Co section of the Slater-Pauling Curve showing a peak of $2.5\mu_B/\text{atom}$ occurring at $\text{Fe}_2\text{Co}$ [34]. . . . .	21
1.9 Depiction of the difference in the hysteresis curve between a hard and soft magnet. A soft magnet has a narrower curve due to its small coercivity. . . . .	23
1.10 Cross-section of a toroidal core with a laminae or rectangular cross-section. . . . .	25
1.11 Diagram of a transformer. . . . .	27

1.12	Schematic of results from paper by Schwarz [46]. While the eddy current losses decrease with the core thickness, the total losses increase due to increasing anomalous losses. . . . .	33
2.1	A Copper mold used in copper mold casting of bulk metallic glasses.	39
2.2	A photo of two thin walled quartz tubes with differing diameters, and a quartz capillary. . . . .	40
2.3	Data on the effects of the overheating temperature on the glass forming ability and toughness of an alloy [66] . . . . .	42
2.4	Fe-B phase diagram adapted from [68], through the use of the ASM Phase Diagram database. . . . .	44
2.5	Peak in the glass forming ability of the Fe-based alloy as we vary the cobalt concentration following: $Fe_{77-x}Co_xSi_8B_{15}$ . There is no obvious cusp in the glass forming ability as described by Na[27], but rather a plateau ranging from 17-27% Co. . . . .	46
2.6	Cusp in the glass forming ability of the Fe-based alloy as we vary the cobalt concentration. We follow the formula: $Fe_{77-x}Co_xSi_{7.5}B_{5.5}P_{10}$ .	49
2.7	Hysteresis curve for $Fe_{57}Co_{20}Si_{7.5}B_{5.5}P_{10}$ run at 50 Hz and 25 kA/m. This alloy has a magnetic saturation of 1.57 T. . . . .	51
2.8	Permeability and coercivity of $Fe_{57}Co_{20}Si_{7.5}B_{5.5}P_{10}$ as a function of frequency. At a DC frequency $Fe_{57}Co_{20}Si_{7.5}B_{5.5}P_{10}$ has a permeability of 58,480 and a coercivity of 2.3 A/m . . . . .	52
3.1	Dependence of the critical rod diameter of Fe-Co-Si-B-P alloys on the atomic concentration of B in the fluxed and unfluxed alloy with Si being substituted by B in the alloy. The unfluxed alloys follow $Fe_{57}Co_{19.2}Si_{14.2-x}B_xP_{9.6}$ while the fluxed alloys follow $Fe_{57.5}Co_{20.2}Si_{(12.3-x)}B_xP_{10}$ . . . . .	60

3.2	Calorimetry scans at 20 K/min of: (a) the alloy having the peak GFA in the fluxed series, $\text{Fe}_{57.5}\text{Co}_{20.2}\text{Si}_{10.2}\text{B}_{2.1}\text{P}_{10}$ , and (b) the alloy having the peak in the unfluxed series, $\text{Fe}_{57}\text{Co}_{19.2}\text{Si}_{6.8}\text{B}_{7.4}\text{P}_{9.6}$ . The $T_c$ , $T_g$ , $T_x$ , $T_s$ , and $T_l$ are identified by arrows. . . . .	62
3.3	Change in boron and silicon in $\text{Fe}_{57.5}\text{Co}_{20.2}\text{Si}_{10.2}\text{B}_{2.1}\text{P}_{10}$ as a function of fluxing time as measured by SIMS. . . . .	63
3.4	Ellingham diagram showing the free energy of boron, silicon, and their oxides over a broad range of temperatures [77]. . . . .	64
3.5	Calorimetry scans around the melting temperature of various fluxing states of alloy $\text{Fe}_{57}\text{Co}_{19.2}\text{Si}_{6.8}\text{B}_{7.4}\text{P}_{9.6}$ : (a) no fluxing, (b) 1 hour fluxing, (c) 2 hours fluxing, (d) 5 hours fluxing, (e) 10 hours fluxing, and (f) 21 hours fluxing. The arrows designate the liquidus temperatures. . . . .	66
4.1	Casting box used to injection mold Fe-based samples into disc and toroidal geometries. Samples are heated by an inductive coil, while the temperature is measured by a pyrometer. . . . .	72
4.2	Copper mold used to injection mold ferromagnetic metallic glass disks. . . . .	73
4.3	Injection cast metallic glass disc of $\text{Fe}_{68}\text{Mo}_4\text{Ni}_3\text{Co}_5\text{Si}_1\text{B}_{2.5}\text{P}_{11.5}\text{C}_5$ . This sample will then be machined into a toroidal core. . . . .	74
4.4	Cross section of an 11 mm cast rod of $\text{Fe}_{68}\text{Mo}_4\text{Ni}_3\text{Co}_5\text{Si}_1\text{B}_{2.5}\text{P}_{11.5}\text{C}_5$ . This rod was cast in a quartz tube and quenched in water. . . . .	76
4.5	Cooling profile of a the cross section of a cylindrical rod. At time 0, the sample has et to be cooled and the temperature is constant across the rod. At time 1, the sample has been quenched and the exterior of the rod has dropped below $T_g$ and solidified, but the interior of the rod is still molten. At time 2 and 3, the rod is still cooling, with the rod solidifying from the outside. At time 4, the rod has cooled to room temperature and is now completely solid. . . . .	77

4.6	Loss curves for $e_{68}\text{Mo}_4\text{Ni}_3\text{Co}_5\text{Si}_1\text{B}_{2.5}\text{P}_{11.5}\text{C}_5$ on a plot of total losses per kg per cycle versus the frequency. As the stress annealing time increases, the losses decrease until they reach a plateau at a stress anneal time of 30 minutes. Similar effects are seen for $\text{Fe}_{57}\text{Co}_{19.2}\text{Si}_{6.8}\text{B}_{7.4}\text{P}_{9.6}$ .	78
4.7	Impact of stress annealing for 45 minutes at 60K below $T_g$ on the permeability and losses of a toroidal core of $\text{Fe}_{68}\text{Mo}_4\text{Ni}_3\text{Co}_5\text{Si}_1\text{B}_{2.5}\text{P}_{11.5}\text{C}_5$ . Similar effects are seen for $\text{Fe}_{57}\text{Co}_{19.2}\text{Si}_{6.8}\text{B}_{7.4}\text{P}_{9.6}$ .	80
4.8	EDM holder and cut core. (a) The steel base of the final iteration of holder and the entirety of the first iteration. (b) The graphite top of the final iteration on the sample holder. (c) A cut toroidal core with a wall thickness of 250 microns.	82
4.9	Wound toroidal core.	83
4.10	Total losses per kg versus frequency. This is the raw data assembled from the hysteresisgraph with each data point being a hysteresis curve.	84
4.11	Power law fit of the losses per cycle versus frequency data is in red. Also plotted, in black, is the hysteresis losses for the sample.	86
4.12	Effect of magnetic annealing on the losses per cycle in $\text{Fe}_{68}\text{Mo}_4\text{Ni}_3\text{Co}_5\text{Si}_1\text{B}_{2.5}\text{P}_{11.5}\text{C}_5$ .	89
5.1	Losses per cycle as a function of frequency for $\text{Fe}_{68}\text{Mo}_4\text{Ni}_3\text{Co}_5\text{Si}_1\text{B}_{2.5}\text{P}_{11.5}\text{C}_5$ of varying core thickness, ranging from 0.18 mm to 0.65 mm. At high frequencies the traditional viewpoint of eddy current losses dominating is correct.	95
5.2	Losses per cycle as a function of frequency at low frequencies for $\text{Fe}_{68}\text{Mo}_4\text{Ni}_3\text{Co}_5\text{Si}_1\text{B}_{2.5}\text{P}_{11.5}\text{C}_5$ of varying core thickness, ranging from 0.18 mm to 0.65 mm. The transition in efficiency begins to become apparent at these frequencies.	96

- 5.3 Losses per cycle versus the thickness of  $\text{Fe}_{68}\text{Mo}_4\text{Ni}_3\text{Co}_5\text{Si}_1\text{B}_{2.5}\text{P}_{11.5}\text{C}_5$  toroidal cores, at a frequency of 250 Hz and a max magnetization of 0.1 T. The minimum was found through the use of a smoothing spline. 97
- 5.4 Optimal thickness of a stress annealed core made out of  $\text{Fe}_{68}\text{Mo}_4\text{Ni}_3\text{Co}_5\text{Si}_1\text{B}_{2.5}\text{P}_{11.5}\text{C}_5$  versus the frequency that the core is run at. The fit of the data is logarithmic in nature. . . . . 99
- 5.5 Optimal thickness as a function of the maximum magnetization. The slope of the optimal thickness curve steepens as  $B_m$  increases. . . . 100
- 5.6 Magnetic annealing shifts the optimal thickness curve to a lower thickness range by decreasing  $W_a$ , while not affecting  $W_e$ . . . . . 102

## LIST OF TABLES

<i>Number</i>	<i>Page</i>
1.1 Experimental resistivities(at RT) of metallic glasses and crystalline silicon steel. All resistivities are in Ohm-meters. . . . .	23
1.2 Nominal alloys of interest in the literature. This is a brief overview of their magnetic properties. . . . .	31
1.3 Compositions of the two alloys developed from our new understanding of fluxing, along with their key material properties. . . . .	35
2.1 Effect on the critical rod diameter of replacing phosphorous with silicon and boron. All reported compositions are in atomic percent and all critical rod diameters are for quartz tubes. . . . .	48
2.2 Effect on the critical rod diameter of replacing silicon with boron. All reported compositions are in atomic percent and all critical rod diameters are for quartz tubes. . . . .	48
2.3 Effect on the critical rod diameter of the metal to metalloid ratio. All reported compositions are in atomic percent and all critical rod diameters are for quartz tubes. . . . .	48
3.1 Change in critical rod diameter, and concentrations of B and Si due to fluxing in Pd-based and Fe-based metallic glasses. All alloys were fluxed under the same conditions, and changes in composition were measured by SIMS. . . . .	67

## LIST OF EQUATIONS

1.1	Gibbs free energy . . . . .	11
1.2	Entropy . . . . .	11
1.3	Relationship between the critical cooling time of a rod and its diameter.	14
1.4	Heisenberg Hamiltonian for a two electron system. . . . .	18
1.5	Exchange energy to deal with antisymmetry of wave function. . . . .	18
1.6	Magnetic field in a ferromagnetic element . . . . .	19
1.7	Stoner Criterion . . . . .	20
1.8	Ohmic Heating . . . . .	24
1.9	Basic equation for Eddy Current Losses in a toroidal core . . . . .	24
1.10	Geometric factor to account for the cross-sectional area of the toroidal core. This goes from 6 for a ribbon to 16 for a circle . . . . .	25
1.11	Skin depth, accounting for the penetration of the magnetic field as a function of the frequency . . . . .	25
1.12	Eddy Current Losses with the skin depth and frequency corrections .	26
1.13	Power from the flow of electricity . . . . .	27
1.14	Ohm's Law . . . . .	27
1.15	Power lost due to resistance . . . . .	28
1.16	Total ( $P_t$ ) losses are a combination of the hysteresis ( $P_h$ ), eddy current ( $P_e$ ), and anomalous ( $P_a$ ) losses . . . . .	31
1.17	Total ( $W_t$ ) losses per cycle in a transformer core . . . . .	31
2.1	Equation to predict the ratio of metals to metalloids for the alloys eutectic composition. . . . .	45
2.2	Relative permeability is the ratio permeability of the conducting medium to the permeability of free space . . . . .	50
3.1	Redox reaction occurring when Si-containing alloys are fluxed with boron oxide . . . . .	64

4.1	Opposing magnetic field created by internal stresses interacting with magnetostriction. . . . .	75
4.2	General form of the losses per cycle versus frequency curves. . . . .	85
4.3	Applied field, assuming the path length is along the outer diameter of a 4 mm toroid. . . . .	88
5.1	General equation to fit the optimal thickness as a function of frequency. This works well in the fitted regimes, but will not apply at every frequency. . . . .	98
6.1	Volume to surface area ratio for a transformer with a circular cross-section. . . . .	107
6.2	Volume to surface area ratio for a transformer with a rectangular cross-section . . . . .	107
6.3	Equating parameters from the previous two V:SA equations. . . . .	107
6.4	V:SA ratio of a transformer with a circular cross-section will be less than that of a transformer with a rectangular cross-section. . . . .	107

## NOMENCLATURE

- Alloy Development.** A systematic process during which the glass forming ability of the alloy is optimized.
- Anomalous Losses.** Poorly understood losses which are related to the frequency of the domain wall rotation and the geometry of the sample.
- Bohr Magnetron ( $\mu_B$ ).** The unit which represents the magnetic moment of a single electron.
- Bulk Metallic Glass.** A metallic glass alloy with a critical rod diameter above 3 mm..
- Coercivity ( $H_c$ ).** The magnetic field needed to fully demagnetize a magnetic material. Also the x-intercept on a hysteresis curve.
- Critical Rod Diameter.** The largest diameter at which a rod of a given composition can be formed as a metallic glass with no crystalline inclusions. See Glass Forming Ability.
- Crystallization Temperature ( $T_x$ ).** The temperature during heating of the glass at which the crystallization process begins.
- Domain.** An area of a material where the orientation of the atomic magnetic fields are parallel. The size of a domain can range from a small section of the part to its entirety.
- Eddy Current Losses.** The losses predicted from Maxwell's equations and generated from inductance of a magnetic material.
- Eutectic.** A composition where there is both a low in the melting temperature and where the solidus and liquidus are at the same temperature.
- Ferromagnetic.** A material that can spontaneously self-magnetize.
- Glass Forming Ability (GFA).** The capability of a composition to resist crystal nucleation/growth and form an amorphous solid. Also referred to as Critical Rod Diameter.
- Glass Transition Temperature ( $T_g$ ).** The temperature at which the viscosity of the liquid reaches  $10^{12}$  Pa·s. At this temperature, the alloy will not flow during any lab time scale.
- Hysteresis Losses.** The time independent losses generated by the thermodynamically irreversible rotations of the domain walls.

**Hysteresisgraph.** The device used in this thesis to measure the magnetic properties of a material..

**Liquidus Temperature ( $T_l$ ).** The temperature at which the material transitions from being a both a solid and a liquid to only a liquid.

**Magnetic Annealing.** Applying a magnetic field while also raising the material to an elevated temperature that is below its  $T_g$ . This is done to impart a preferred orientation for the magnetic domains.

**Magnetostriction.** The strain response in a material when the magnetic moments are ordered and aligned..

**Max Magnetization ( $B_m$ ).** The highest magnetization that the material is raised to. The max magnetization is usually well below the saturation magnetization, and is used to compare materials with different saturation magnetizations.

**Metallic Glass.** A metallic alloy lacking any long-range ordering of its atoms, thus giving it unique properties.

**Permeability ( $\mu$ ).** Also talked about as the relative permeability, this is the response of a material to an applied magnetic fields with higher permeabilities corresponding to higher magnetizations for a given field.

**Power(Electrical).** Rate that electrical energy flows past a given point.

**Quench.** The act of rapidly cooling a material from a raised temperature. A fast quench rate is necessary to vitrify a metallic glass from its liquid state.

**Redox Reaction.** A reaction in which one molecule is reduced and another is oxidized.

**RT.** Room Temperature or 293K.

**Saturation Magnetization ( $B_s$ ).** The highest magnetization that a given material can reach in an infinite magnetic field. In the traditional picture of the hysteresis curve, this is also the its apex.

**Solenoid.** A loop of wire that generates a magnetic field inside of it when an electric current passes through the wire.

**Solidus Temperature ( $T_s$ ).** The temperature at which the material transitions from being only a solid to being both a solid and a liquid.

**Stoner Parameter ( $I$ ).** A measure of the Coulombic interactions used to determine if an element is ferromagnetic.

**Stress Annealing.** Raising a material to an elevated temperature that is below its  $T_g$ , in order to remove any internal stresses inside of the sample.

- $T_{GFA}$ .** The critical glass forming temperature, above which the alloy must be overheated in order to achieve its maximum GFA..
- $T_{tough}$ .** The critical toughness temperature, above which the alloy must be overheated in order to achieve its maximum toughness..
- Thickness.** Thickness refers to the wall thickness of a transformer core, or half the difference of the outer and inner diameter, as displayed in Figure 1.10.
- Total Losses.** The losses generated when a material is magnetized and demagnetized. This is the sum of the hysteresis losses, the eddy current losses, and the anomalous losses.
- Transformer.** An electrical device that changes the voltage of the electricity passing through it.
- Vitrify.** Convert into a glass, usually by cooling from the liquid state.
- Voltage.** The difference in electrical potential between two points.

*Chapter 1*

## INTRODUCTION

**1.1 Overview of Metallic Glasses**

Before we can move on to anything else, we must address what a metallic glass is. Metallic glasses share the features of both a metal and a glass, but have more in common with metals. They still share electrons in the same manner, they are usually alloys primarily consisting of transition metal elements, and their electrical, optical, and mechanical properties are comparable to those of other metals. The big difference from conventional metals is in the atomic structure, where a metallic glass has a non-crystalline structure similar to a oxide glass. While a crystalline metal's atoms are arranged in a periodic structure, usually as face-centered cubic (FCC), body-centered cubic (BCC), or hexagonal close packed (HCP), a metallic glass has a random structure with no long-range order. The distance between atoms can be described by a radial distribution function that is determined by the X-Ray diffraction pattern of the alloy, as seen in Figure 1.1. The lack of structure can also be seen in a high resolution TEM image, with the crystalline metal exhibiting a clearly periodic structure, and the amorphous metal showing no visible patterns [1]. This randomness in the structure, along with its global homogeneity and lack of defects, is responsible for the unique properties of metallic glasses.

The first metallic glass was discovered by Professor Pol Duwez at the California Institute of Technology in 1960 [2]. The alloy,  $\text{Au}_{75}\text{Si}_{25}$ , was synthesized at ultra-high cooling rates,  $>10^6\text{K/s}$ , and formed as a  $10\mu\text{m}$  thick foil. The ability to form a metallic glass stems from this super fast cooling; by bypassing the nose of the Time-Temperature Transition (TTT) diagram, crystallization can be avoided and a vitrified glass "phase" is formed, as seen in Figure 1.2. This work by Duwez

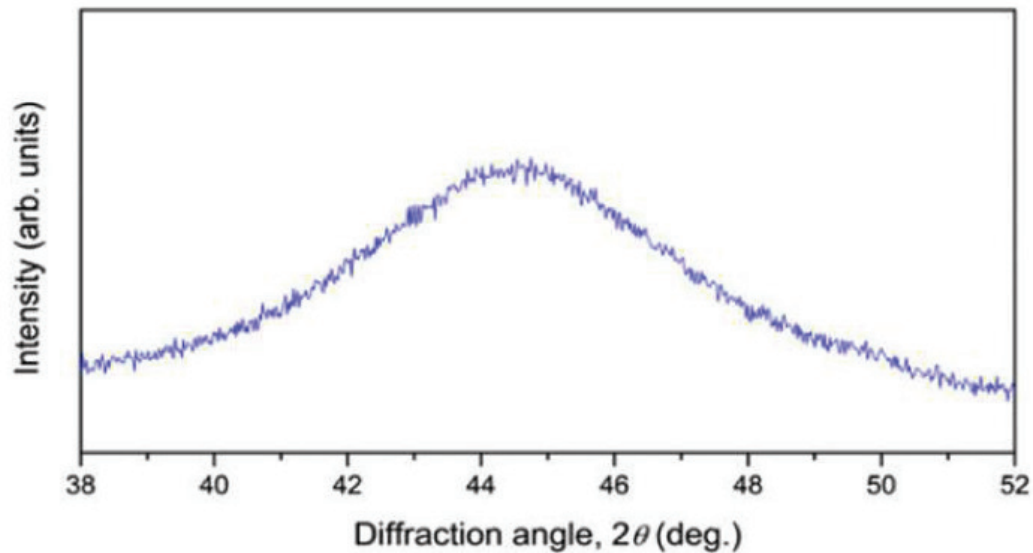


Figure 1.1: X-Ray Diffraction scan of an amorphous metal.

sparked a large amount of scientific and commercial research into metallic glasses, investigating their unique properties and basic physical phenomena. The next major advancement occurred several years later in 1969, with Turnbull laying out the fundamental framework for forming metallic glasses [3]. In the early 1980's, metallic glasses found their first large-scale commercial application with Metglas. Metglas is the trade name for a family of Fe- and Co- based metallic glasses used for their soft magnetic properties. Even though Metglas is limited to ribbons with thicknesses below  $50\mu\text{m}$ , it found a niche market which allowed for its commercial development and use. During the 70s and 80s, a large number of other alloy systems were developed, but it wasn't until the late 1980s and early 1990s that another major breakthrough occurred. Before then, only Pd- and Pt- based glasses could be formed with a glass forming ability above 2 mm, with all other systems stymied below this threshold [4]. Professor William Johnson at the California Institute of Technology [5] and Professor Akihisa Inoue at Tohoku University [6] discovered that the crystallization kinetics<sup>1</sup> could be sufficiently frustrated to allow for metallic

<sup>1</sup>These discoveries were in Zr- and Al- based systems, and started another wave of exploration for glass forming systems with a variety of metal bases.

glasses to form at much lower cooling rates of  $\sim 10\text{k/s}$  or less. This allowed for the formation of the first commercial bulk metallic glasses, and gave rise to the present era of metallic glasses. In this era, further development of metallic glasses has not been limited by their glass forming abilities. Instead the economics, processability, added value, and usefulness of the material are the limiting factors. All of these new issues are being explored by different companies, with mixed success, but there is reason to believe that the commercial future of metallic glasses is near.

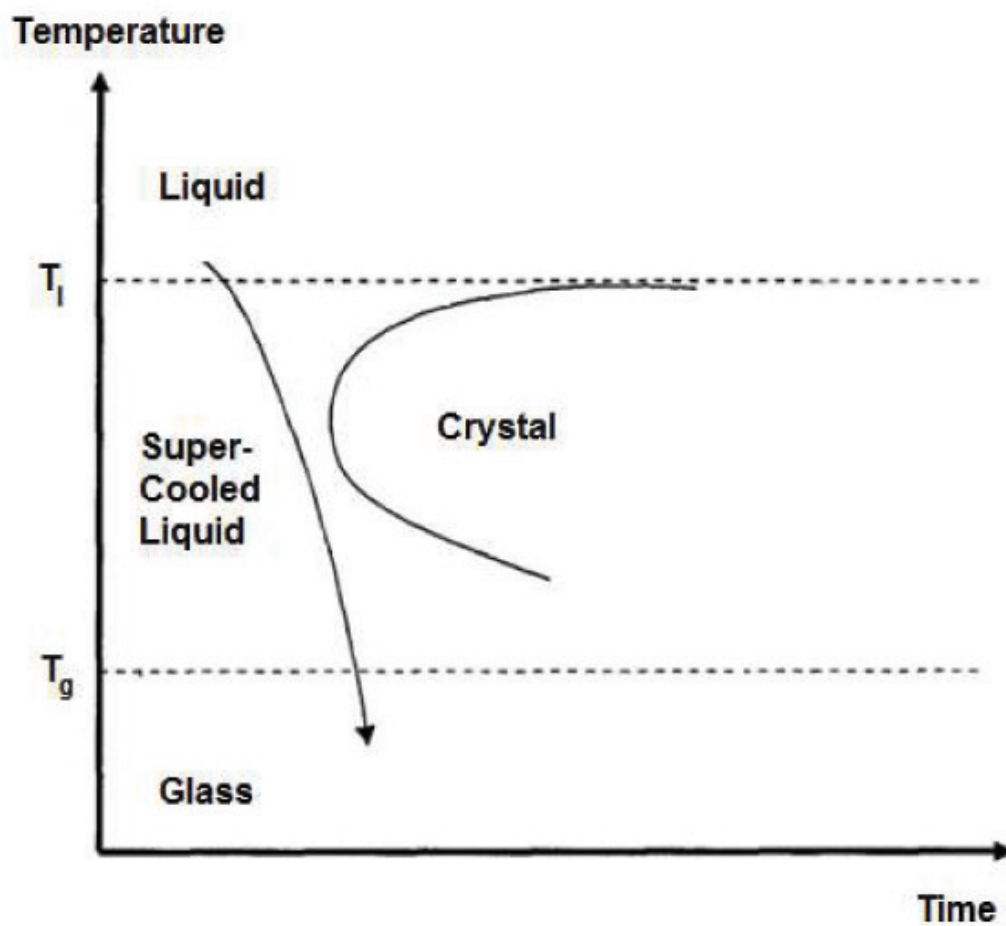


Figure 1.2: TTT-diagram of the cooling path required for a molten alloy to become a metallic glass.

### 1.1.1 Properties of a Metallic Glass

The majority of a metallic glass's unique properties arise from either the glass transition temperature ( $T_g$ ), or the random, homogeneous structure. The glass transition is a feature unique to metallic glasses among other metals and alloys, but is shared with other oxide glasses and thermo-plastics.

Formally,  $T_g$  is the temperature where the viscosity of the super-cooled liquid reaches  $10^{12}$ Pa·s. At this viscosity, the alloy is essentially a solid, and the glass will remain stable for extended periods of time<sup>2</sup>. In Figure 1.3, we can see that the rate of change in the volume as a function of temperature remains constant while the alloy is in a liquid or molten phase. If the alloy bypasses crystallization by transforming into a super-cooled liquid, then there is an abrupt change in thermal expansion at  $T_g$  as the liquid vitrifies. Upon heating past  $T_g$ , a metallic glass will crystallize and its specific volume will fall, which leads to a loop in the specific volume as a glass is cooled and heated. As seen in Figure 1.4, during differential scanning calorimetry (DSC) the metallic glass is heated at a constant rate<sup>3</sup>. Upon reaching  $T_g$ , there is an observable change in the heat flow prior to the crystallization of the glass. While there are these distinct differences between the glass, liquid, and crystal, the glass is not a distinct phase. The glass transition does not show the hallmarks of a true phase, since the thermal expansion coefficient and the heat capacity change continuously as the alloy goes through the glass transition temperature<sup>4</sup>.

In the DSC scan shown in Figure 1.4, there are four temperatures of interest, demarcated by arrows:  $T_g$ , the crystallization temperature ( $T_x$ ), the solidus temperature ( $T_s$ ), and the liquidus temperature ( $T_l$ ). While the  $T_g$  can shift due to the heating rate of the sample, with faster heating rates corresponding to higher  $T_g$ 's, the heating rate here is 20 K/s, which is standard for the literature. The  $T_g$  relates to the most

---

<sup>2</sup>A metallic glass will not flow during any observable laboratory time scale.

<sup>3</sup>The standard heating rate for DSCs scans in the metallic glass community is 20K/min.

<sup>4</sup>There is an ongoing discussion of whether or not there is a phase change, but this is still unresolved.

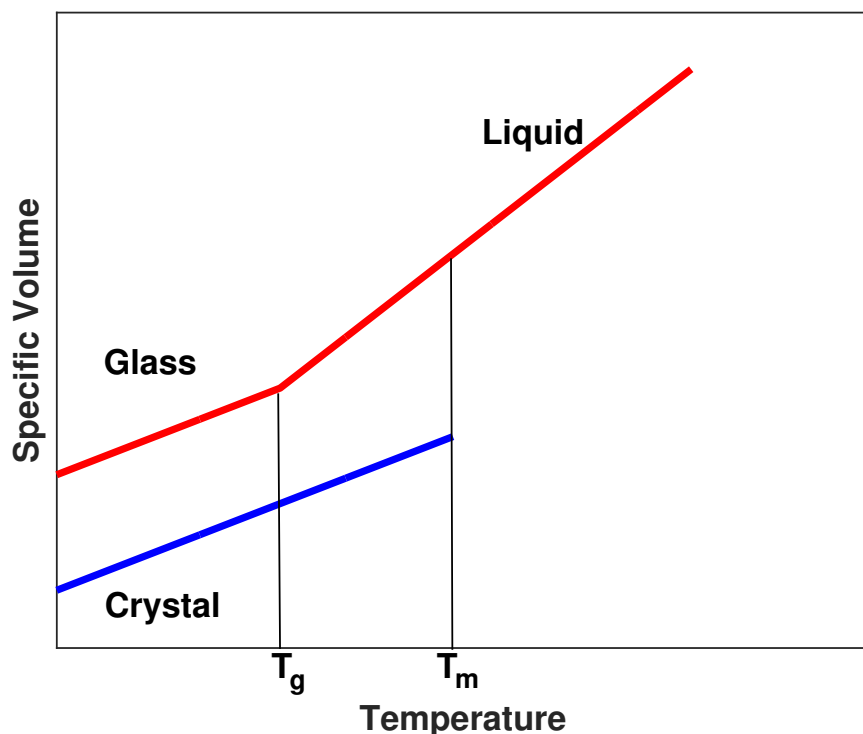


Figure 1.3: The rate of change in volume differs between "phases".

interesting properties for metallic glasses, including their processability. When the glass is heated above  $T_g$ , its viscosity rapidly decreases. By processing and cooling the glass in less than the amount of time it takes to crystallize, it can be shaped or formed into complex parts, allowing for processing in a manner normally associated with thermos-plastics. Another temperature that can be assessed from the DSC scan is the Turnbull parameter, or the reduced glass transition temperature ( $T_{rg}$ ). The  $T_{rg}$  is the ratio of the glass transition temperature to the liquidus temperature, with a ratio that approaches  $2/3$  considered an indicator for easy glass formation [7], [8]. This Turnbull parameter is often used as a predictor of bulk glasses in the past, but more recent work suggests only a general guideline at best.

The second major characteristic of metallic glasses is their random, homogeneous structure. This is due to the speed at which metallic glasses are cooled, and the disordered liquid phase that they are cooled from. During quenching, atoms in

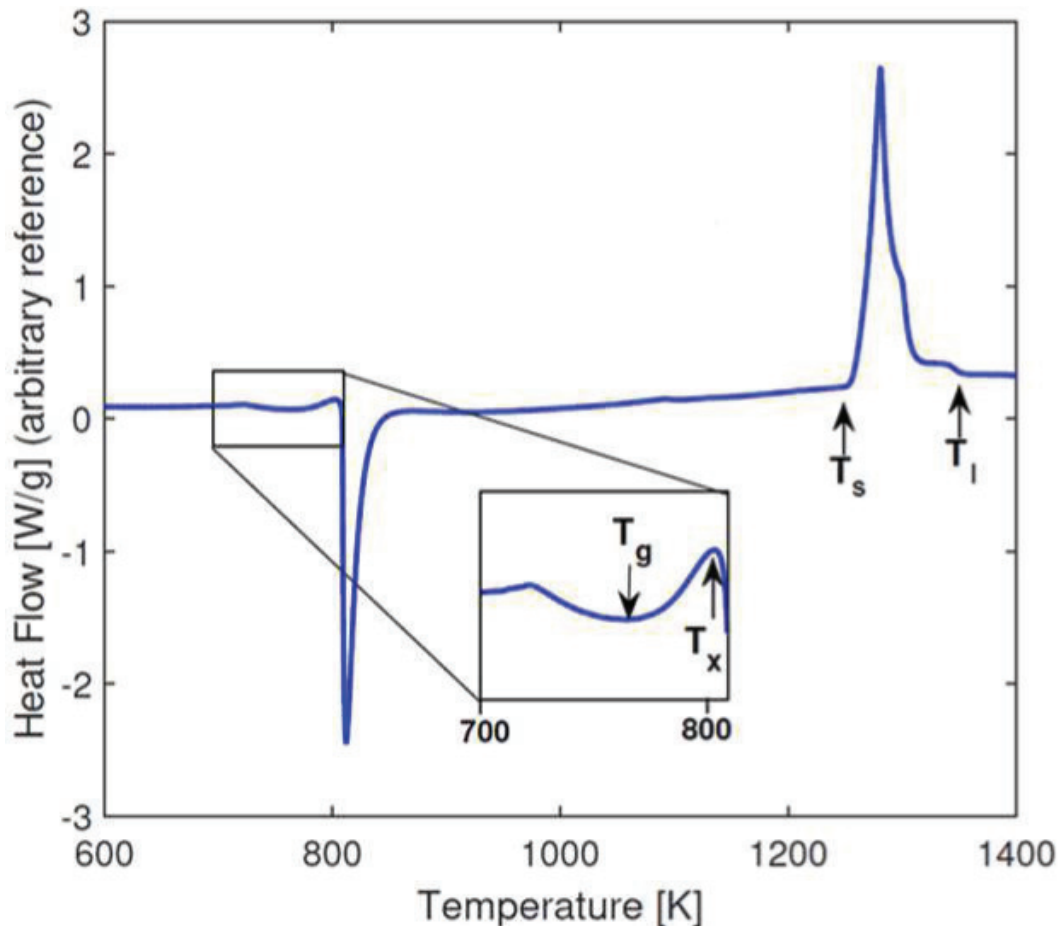


Figure 1.4: Differential scanning calorimetry scan of a metallic glass. The glass transition temperature ( $T_g$ ), crystallization temperature ( $T_x$ ), solidus temperature ( $T_s$ ), and liquidus temperature ( $T_l$ ) are identified by arrows.

the liquid cannot rearrange themselves into periodic structures in the time-scale of cooling, giving the metallic glass a metastable "liquid" structure. The lack of topologically identifiable defects in this random structure leads to its unique mechanical properties, with its strength approaching that of the ideal strength, while at the same time leading to the lack of ductility found in most alloys [9]. The lack of grain boundaries and dislocations, along with a metallic glass's homogeneity, lead to their excellent corrosion resistance in comparison to their crystalline counterparts [10]. This global homogeneity also contributes excellent soft magnetic properties, with magnetic metallic glasses being homogeneous on the same length scale as the magnetic correlation length [11]. Finally, the randomness of the structure leads to high

electron scattering [12], causing metallic glasses to have several times the electrical resistance, and a lower thermal conductivity than their crystalline counterparts [13].

### **1.1.2 Attempts at Commercialization**

There have been multiple attempts to commercialize metallic glasses, and while some have turned into successful endeavors, none of them have transformed metallic glasses into a household name. There are many reasons for the lack of adoption of metallic glasses, but the three I will highlight are cost, processability, and scale. To explore these limitations, I will explore each as a case study of a company, the unique metallic glass property that was being utilized, and how the attempt failed. Chronologically we first come upon commercial Metglas, which is utilized for its magnetic properties. Metglas production by continuous casting was first developed in the 1970s [14], but it wasn't until the 1980s that it became a commercially viable product. The Metglas trade name encompasses a range of amorphous metals, either Fe-based, Ni-based, or Co-based, which fall within a window of magnetic and mechanical properties, but with each having a specific target application. The most interesting properties are their high magnetic saturation, low magnetic losses, and limited glass forming ability. These magnetic properties have enabled their growth into various market sectors, with the largest sector being the power distribution transformer market. Here, Metglas currently consists of up to 15% of the market in some countries [15]. While Metglas would allow for a more efficient power distribution grid [16], there are two factors which have limited Metglas' utilization: the price of sheet material and the intransigence of the utility market. The current generation of power transformers consisting of Si-steel (which has a production cost an order of magnitude below Metglas's) are still performing well within their lifespan, thus limiting Metglas to around 5% of the market. Without the current economic conditions dramatically changing, Metglas will continue to have a limited impact in the power transformer market.

The second commercialization attempt I examine is the case of Liquidmetal Technology, their attempts to change the golf club market, and how they were stymied by their chosen processing mechanism. With the advent of the Zr-based bulk metallic glass, Vitreloy, by Bill Johnson in the 1990s, Liquidmetal started up and had an alloy to utilize in a range of sporting goods applications, with one of those being golf clubs. This avenue was based on several novel properties of Vitreloy: compared to the previous bulk glasses their raw materials were cheap<sup>5</sup>, amorphous parts could be formed out of Vitreloy having complex geometries and large thicknesses, and they had a unique combination of strength and elastic energy storage density [17]. This combination of properties allowed for the casting of golf club heads and, paired with a good marketing campaign, led to much excitement over their production. Unfortunately the excitement was unfounded since Vitreloy was not ready for the mass market. Liquidmetal attempted to use die casting for golf club head production, which led to a low yield rate of usable golf club heads. The problem with die casting metallic glasses is threefold, all of which stem from injecting a very hot liquid into a die [18]. The first problem is the flow of the liquid into the mold; the low viscosity liquid splashes and beads, creating flow lines, stress fields, and porosity. All of these may lead to catastrophic failure of the part. The second problem is that the mold must absorb large amounts of heat from the liquid. This limits the cooling rates that are accessible, thus limiting the thickness of the amorphous parts that can be cast. The heat withdrawal problem also limits the aspect ratio of castable sections, since the mold is designed to withdraw heat as quickly as possible, high aspect ratio sections can preemptively vitrify the liquid and prevent the mold from filling. The final problem is with the mold itself and tool life, both of which are severely degraded by casting with such a hot liquid. These technical problems stopped Liquidmetal from widespread success, but due to the

---

<sup>5</sup>The other large glass formers of the day contained either large amounts of noble metals, or contained rare earth elements.

unique material properties, i.e. the elastic strain limit of metallic glass<sup>6</sup>, the clubs were still popular. Liquidmetal ended up being a victim of Vitreloy's outstanding material properties though, when the PGA Tour effectively banned metallic glass clubs in 1997 by placing a limit of the coefficient of energy restitution for golf clubs [18].

These two attempts to turn metallic glass materials into a commercial product have shaped the newest companies entering the metallic glass market. These companies have learned from the failures and limitations of Metglas and Liquidmetal Technologies, and now are pursuing a different approach. That new avenue continues to build off of the unique properties of metallic glasses, but now focuses on the development of processing techniques to fabricate metallic glasses into high quality net shape parts. By doing so they hope to overcome two problems from the past: cost and fabrication. On the production side, these new companies are developing novel production methods based around metallic glasses unique properties and limitations. By creating methods similar to plastic injection molding, metallic glasses can be fabricated into complex, net-shape parts at a low cost and with few production defects. However, such processes are in the process of being scaled up, and it has yet to be determined which process, if any, will be successful. This leads us to the issues of cost viability for these new production techniques. Commercial viability will ultimately hinge on: (1) identifying products where the cost of the material is not the primary factor driving the cost of the product, and (2) finding incumbent parts that require expensive machining and fabrication steps. By looking at products where the material cost is not a large percentage of the total cost, the additional cost of making the part out of a metallic glass is negated. And by targeting complex parts that currently require expensive machining, net-shape metallic glass parts may be cheaper to produce at large scales.

---

<sup>6</sup>This allowed for metallic glass drivers to hit the ball much further than crystalline metal drivers.

## 1.2 Alloy Development

Having detailed some of the broader characteristics and issues of metallic glasses, I move on to a more in-depth introduction to the technical background needed to understand my work. The first subject is alloy development, which we pursue in a systematic, reproducible manner to design metallic glasses with unique and desired properties.

### 1.2.1 Basic Tenets

To design a metallic glass with high glass forming ability, there are several basic tenants that are followed by a majority of researchers in the field. They are (1) have a large atomic size difference among the elements that compromise the alloy, (2) have at least a four component system, (3) have a negative heat of mixing among the constituent elements, (4) remove oxides and other crystalline debris from the melt through the use of flux, and (5) begin with a composition lying near a deep multicomponent eutectic<sup>7</sup> [19, 20, 21]. Note that tenant (4) only pertains to metallic glasses that contain specific oxide forming elements. Each of these rules affects either the thermodynamics of crystallization, the time in the super-cooled liquid range, or kinetics of the molten alloy[22, 23, 24].

Rule (1) is fairly straightforward: by having a large atomic size difference among the constituent elements, the packing density of the super-cooled liquid is increased, thereby increasing the liquid stability and decreasing the driving force for the nucleation and growth of a crystal. This increase in packing density can be seen when a radial distribution function is used to model the packing of a metallic glass [22].

The thermodynamic perspective allows us to understand how both rule (2)

---

<sup>7</sup>Detailed analysis for the effect of the first three rules on the glass forming ability has been modeled by several groups.

and rule (3) increase the glass forming ability. This can be seen by looking at their role in reducing the Gibbs free energy [22],  $\Delta G$  of the alloy, where:

$$\Delta G = \Delta H - T \cdot \Delta S \quad (1.1)$$

By having a lower Gibbs free energy for the transition from the super-cooled liquid to the crystalline stage, the crystal is less energetically favorable and the "C"-shaped TTT-diagram for crystal nucleation is shifted to the right. This increases the time before crystallization, allowing for a thicker glass to be formed at lower cooling rates and larger processing windows. To increase the negativity of the Gibbs free energy, either the enthalpy can be decreased or the entropy can be increased. Rule (3) directly deals with the enthalpy, by decreasing the enthalpy of mixing, the overall liquid enthalpy can be decreased. Similarly, rule (2) deals with the entropy. By increasing the number of elements in the alloy we also increase the number of chemical microstates. We can write the entropy as:

$$\Delta S_{mix} = k_b \sum_{\alpha=1}^M c_{\alpha} \ln(c_{\alpha}) \quad (1.2)$$

where  $k_b$  is the Boltzmann constant,  $\alpha$  runs over the "M" components, and  $c_{\alpha}$  is the concentration of each component in the alloy. This mixing entropy increases as the number of elements in the alloy increases.

Rule (5) is often equivalent to another rule, which states that the alloy should roughly contain 80 at.% metal elements and 20 at.% metalloid elements [20]. Our variation is based on this, but differs in the fact that we find that the optimum metalloid percentage can vary by as much as  $\pm 5\%$ . What actually matters is that the composition is close to that of a eutectic composition. In Figure 1.5, we have a plot of the temperature versus the composition for a binary system. For any given composition, the alloy will progress from a liquid to a solid as the

temperature decreases, with the eutectic composition having no liquid-solid solution. The eutectic composition also has the lowest melting temperature for the binary alloy<sup>8</sup>. When we move from a binary alloy, like the one presented in Figure 1.5, to a more complex multicomponent system the eutectic may still exist, and will be a local or global minimum in the liquidus temperature. By melting at this lower temperature, we can shrink the super-cooled liquid region between  $T_g$  and  $T_l$ , and increase the time available for a glass to form before crystal nucleation.

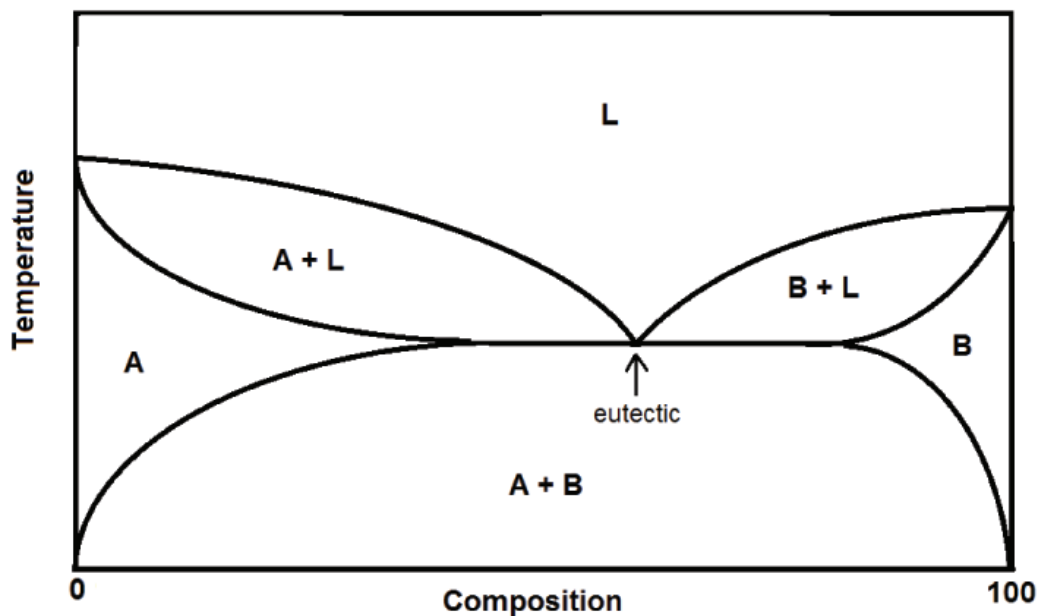


Figure 1.5: Binary eutectic phase diagram, displaying a eutectic composition. This eutectic composition is characterized by a minimum in the liquidus.

Rule (4) is the only rule which is not broadly applicable to all metallic glasses, with some alloy systems not impacted by the fluxing procedure, and other systems having adverse effects from it. Fluxing was first used in metallic glasses in 1984 by Turnbull [3], and has been employed widely since due to its dramatic effects on reducing heterogeneous nucleants. For example boron oxide flux,  $B_2O_3$ , is melted with the alloy, and resides on top of the metal<sup>9</sup>. While in contact with the molten

<sup>8</sup>In more complex systems, multiple eutectic compositions may exist, along with eutectoid compositions.

<sup>9</sup>This is similar to the slags seen in traditional metal processing.

alloy, oxide particles are removed by absorption into the flux, thus enabling better glass forming ability [25, 26]. This occurs by an unknown mechanism, but I believe that this is most likely due to the oxide particles being able to lower their interfacial free energy by moving out of the molten metal alloy and into the liquid oxide flux. Another possible mechanism is that the oxide particles actually dissolve as oxygen is removed from the alloy by the flux in a redox reaction. By removing the oxide particles/oxygen, there is a reduction in the overall number of heterogeneous nucleation sites, and thus a greater barrier to the formation of the crystalline phase by homogeneous nucleation<sup>10</sup>. By combining all five of these rules, metallic glasses with larger glass forming ability can be created, but these rules are by no means absolute. Each one of them has exceptions and examples that do not run counter to the rule, thereby making the development of glass forming alloys much more complicated.

### 1.2.2 Cusps in GFA

Another technique for discovering the largest possible glass forming ability for a given system is through the search for sharp cusps in the glass forming ability. This requires us to have a very systematic and reproducible approach to carrying out alloy development. The idea of cusps is fairly novel to metallic glasses, partially due to the lack of such systematic methods for alloy development in the past. These cusps, illustrated in Figure 1.6, occur as the composition of the alloy is varied following a given formula, i.e.  $\text{Ni}_{69}\text{Cr}_{8.5}\text{Nb}_3\text{P}_{19.5-x}\text{B}_x$ . In Figure 1.6, there is a steep, exponential rise in the glass forming ability as the system approaches 3 at.% boron, and then an exponential decline in the glass forming ability as the system moves away from that composition. These cusps are believed to arise from the nucleation of two different crystalline phases, or the variation in the driving

---

<sup>10</sup>From a derivation of the Gibbs free energy for homogeneous versus heterogeneous nucleation, it can be seen that more energy is required to nucleate a crystal under homogeneous nucleation.

force for nucleation as the composition varies and nucleation transitions from one crystalline phase to the other [27]. From the derivation of the cooling time,  $\tau_c$ , required to cool a rod by conduction with diameter,  $d$ , we find that:

$$\tau_c \approx d^2 \quad (1.3)$$

This is the actual relationship between the glass forming ability and the critical rod diameter, where the critical rod diameter is  $d$  and the glass forming ability is  $\tau_c$ . The cusp seen in Figure 1.6 is actually much steeper when one examines the variation of the nucleation time as a function of the composition. With the nucleation time in mind, instead of the critical rod diameter, the cusp increases by an order of magnitude as the boron composition changes by 1.5 at.%. These large cusps over small composition changes have been overlooked in many metallic glass systems, where the researchers varied compositions in steps of 5 or 10 at.% [28].

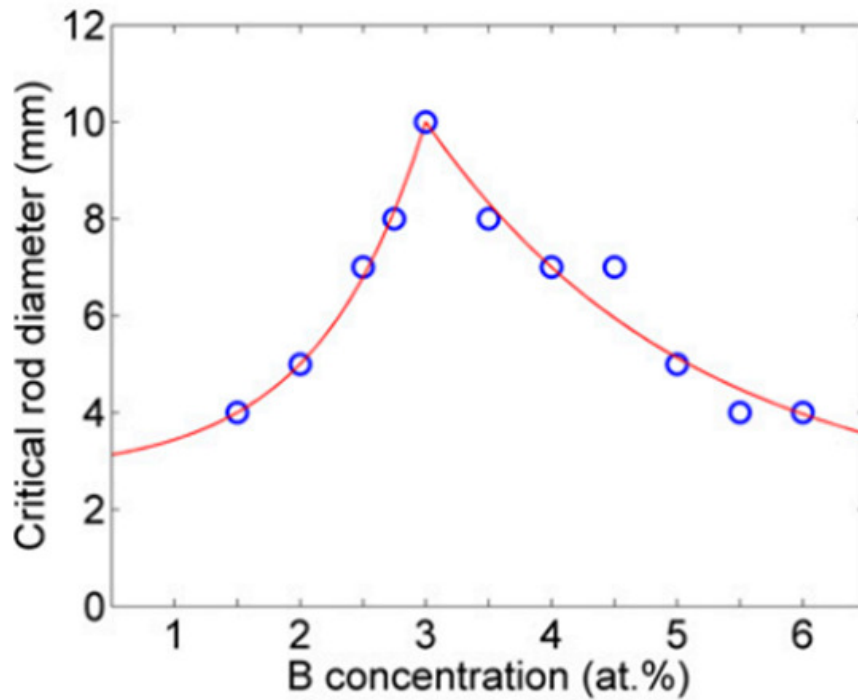


Figure 1.6: Cusp in the glass forming ability of a Ni-based metallic glass as the boron concentration is varied following this formula,  $\text{Ni}_{69}\text{Cr}_{8.5}\text{Nb}_3\text{P}_{19.5-x}\text{B}_x$  [27].

Besides the exceptional steepness in the glass forming ability as a function of composition, the picture of a cusp is not yet complete. Using the knowledge of cusps is complicated by the fact that these cusps arise not only in a single composition space, but also in higher dimensional composition spaces as seen in Figure 1.7 [27]. Figure 1.7 illustrates an island in the critical rod diameter where the critical rod diameter demonstrates a two-dimensional cusp as niobium and chromium are varied. This critical rod diameter map was created by making and measuring the critical rod diameter of over 50 compositions, since there has yet to be a predictive means to assess glass forming ability. By finding these "islands" of higher glass forming ability in multidimensional composition spaces, global maximums are easier to find. However, the complexity of multicomponent systems, with some having 7 elements, ensures such systems cannot be fully explored. With the knowledge of the basic rules governing GFA, and the ability to systematically map GFA, an optimized glass former can be developed.

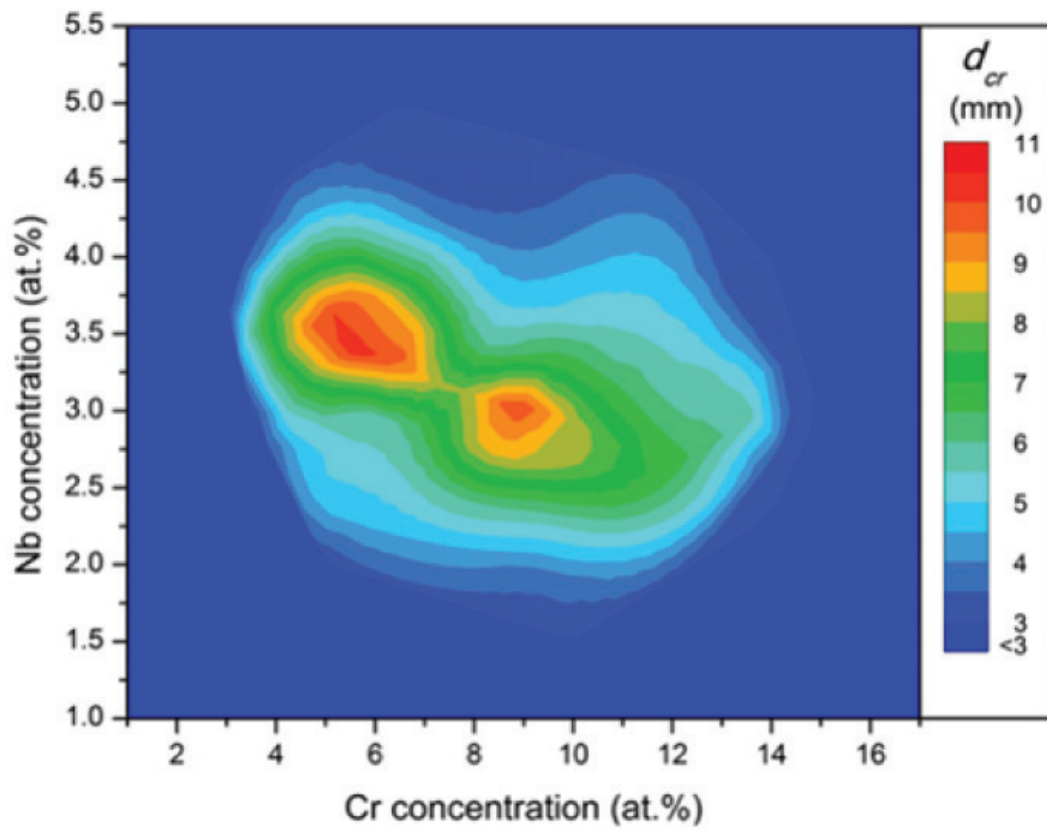


Figure 1.7: Island in the glass forming ability of an Ni-based glass. GFA varies with both the chromium concentration and the niobium concentration [27].

### 1.3 Magnetics and Metallic Glasses

There are several types of magnetism that can exist in a material: paramagnetism, diamagnetism, ferromagnetism, antiferromagnetism, etc. Of the the types though, it is mainly ferromagnetism that mankind has focused on for the past 2500 years [29], and ferromagnetism will also be the focus of this thesis. Ferromagnetism was the first type of magnetism to be discovered, partially due to the strength of a ferromagnetic field in comparison to paramagnetism or diamagnetism. It also was discovered due to the commonality of magnetite,  $\text{Fe}_3\text{O}_4$ , across Turkey and the Mediterranean. Magnetite is a naturally occurring magnetic material, and while being a curiosity for some time, it eventually found use making compasses. Pieces of iron would be rubbed with the magnetite to magnetize the iron, and for thousands of years this was the only way to magnetize a material. However, in 1825 this changed when Oersted discovered that electricity and magnetism were related with the invention of the electromagnet [29]. With this invention, the field of magnetism realized a renaissance, and the principles behind magnetism were explored.

#### 1.3.1 Ferromagnetism

The first attempt that came close to explaining the origins of ferromagnetism was Pierre Weiss's theory on molecular fields developed in 1906 [30]. His theory contained two tenants. First, that ferromagnetism originated from a molecular field, which was strong enough that molecules could magnetize their neighbors, and the rest of the material without the aid of an applied field. Secondly, that instead of a single magnetic field permeating throughout the material, the material was divided into domains, each with their own magnetic field. Before being rubbed with magnetite or having an electromagnet applied to them, the domains would be magnetized in random directions so that the overall field canceled itself out. However, when a magnetic field was applied to the material, the domains would

reorient themselves in the direction of the applied field, and form one unified domain. Molecular field theory did prove to be correct on a number of issues, namely the idea of domains in a magnetic material, how paramagnetism behaves, and the transition to ferromagnetic behavior at the Curie temperature. But the major tenant of molecular fields was problematic, and with Heisenberg's model for quantum mechanics, a better picture for the origin of magnetism emerged<sup>11</sup>.

With the advent on quantum mechanics, and the knowledge of electrons and atomic interactions that came with that, there was finally a model that could explain the origins of magnetism. Magnetism primarily originates from two sources related to electrons: their spin and their orbital momentum. The magnetic moment,  $\mu$ , which is a measure of the contribution of each atom to the magnetic field of the material is proportional to the sum of these contributions. In addition to this, theories on the indistinguishability of particles and the exchange interaction between atoms, allows for a good model to be developed. If we first look at a two electron system, the Hamiltonian yields:

$$H = \frac{p_1^2}{2m} + \frac{p_2^2}{2m} - \frac{z \cdot e^2}{r_1} - \frac{z \cdot e^2}{r_2} + \frac{e}{|r_1 - r_2|} \quad (1.4)$$

where p is the momentum of the electron, m the mass, z the number of nearest neighbors, r the radius, and e the charge of an electron. This ends up having spin dependence caused by the need for antisymmetry of the total wavefunction. With that in mind we need to add an exchange energy, U:

$$U = -2\sum_{i,j} S_i S_j J_{ij} \quad (1.5)$$

where the sum includes the interactions between all electrons, S is spin of the electron, and J is the exchange integral. If we change this basic model to include

---

<sup>11</sup>A special thanks to Keith Schwab, who helped me to understand this during his class on magnetism.

more than two electrons, and to only include identical<sup>12</sup> nearest neighbors, due to the exponential tail of the wave function that falls off quite rapidly with increased distance, then we end up with the magnetic field,  $B$ , equal to:

$$B = \frac{2z \cdot J_{ij} \cdot S_i}{g\mu_B} \quad (1.6)$$

where  $g$  is roughly equal to 2 and  $\mu_B$  is the Bohr magneton<sup>13,14</sup>. This can be related to the definition for the magnetic field derived from the Curie-Weiss law, yielding a relation between the Curie temperature,  $T_c$ , and the quantum mechanical model for ferromagnetism. Using the exchange integral, we also come upon the first explanation of the origins of ferromagnetism, represented in the Bethe-Slater Curve. This model looks at the interatomic radius and the overlap of 3d electrons. If the atomic radius is too small then the overlapping electrons favor antisymmetric spins, and the element is antiferromagnetic. However, as the radius increases the exchange integral remains strong enough for an interaction to occur, but the overlap is small yielding the three ferromagnetic elements (Fe, Ni, and Co) [31]. As we continue moving to the right in the periodic table, the exchange integral weakens resulting in ferrimagnetic or non-magnetic elements.

So far we have been dealing with localized models for magnetism, with the electrons being associated with a given atom. Given that most of the elements/alloys which are of interest for magnetics are metals, this does not make as much sense as modeling the electrons as shared throughout the material. This leads to a second model for ferromagnetism coming from band theory. While band theory is usually thought of in relationship to semiconductors and insulators, it also explains the exact magnetic moments of iron, nickel, and cobalt. The first criteria found in the band

<sup>12</sup>Constraining our system to be one element.

<sup>13</sup>All equations in this section are from my notes from Applied Physics 114C, taught by Professor Keith Schwab at Caltech.

<sup>14</sup> $\mu_B = \frac{e\hbar}{2m_e}$ , where  $e$  is the charge of an electron,  $\hbar$  is the Planck constant, and  $m_e$  is the mass of an electron.

model is that only partially filled subshells contribute to magnetism since these are the open energy levels that electrons can move to. This corresponds to both the 3d and 4s subshell whose energy levels overlap to a large extent. The 4s subshell has higher overall energy levels though, thus enabling the filling of the 3d subshell first [32]. These vacancies in the subshells, along with the high energy density of the 3d subshell, allow for a spin imbalance to easily occur promoting ferromagnetism. These factors allow the band model to predict with a high degree of accuracy the magnetic moment for Fe, Ni, and Co [29]. If we change the model slightly, then we can use the density of states at the Fermi energy,  $g(E_f)$ , and the stoner parameter,  $I$ , to get the resulting Stoner Criterion:

$$I \cdot g(E_f) > 1 \quad (1.7)$$

where only if this criterion is met, will a transition metal be ferromagnetic. While there is some disagreement over whether the band theory or the localized electron model is correct, it is the author's opinion that the band theory better explains ferromagnetism in metallic elements and alloys since the model of sharing electrons is aligned with the other electrical and thermal properties of the metal.

So far we have only discussed ferromagnetism in elements that are not alloyed, but ferromagnetism also exists in multicomponent alloy systems. Most of the time, these alloys are a combination of Fe, Co, or Ni with each other, or a small percentage of a non-ferromagnetic element, but that are also cases of ferromagnetic alloys which do not contain any ferromagnetic elements [33]. And while iron has the highest magnetic moment per atom of any element<sup>15</sup>, certain alloys result in higher magnetic moments than that. Figure 1.8 is a plot of the magnetic moment per atom as a function of cobalt composition for the Fe-Co binary alloy. This is merely a portion of the Slater-Pauling curve, which displays the experimental results for a

<sup>15</sup>Iron has a magnetic moment of  $2.2\mu_B$  per atom.

number of binary alloys. While cobalt has a lower magnetic moment than iron, by adding cobalt to iron, the magnetic moment of the alloy increases with a peak occurring at a ratio of 2:1 iron to cobalt.

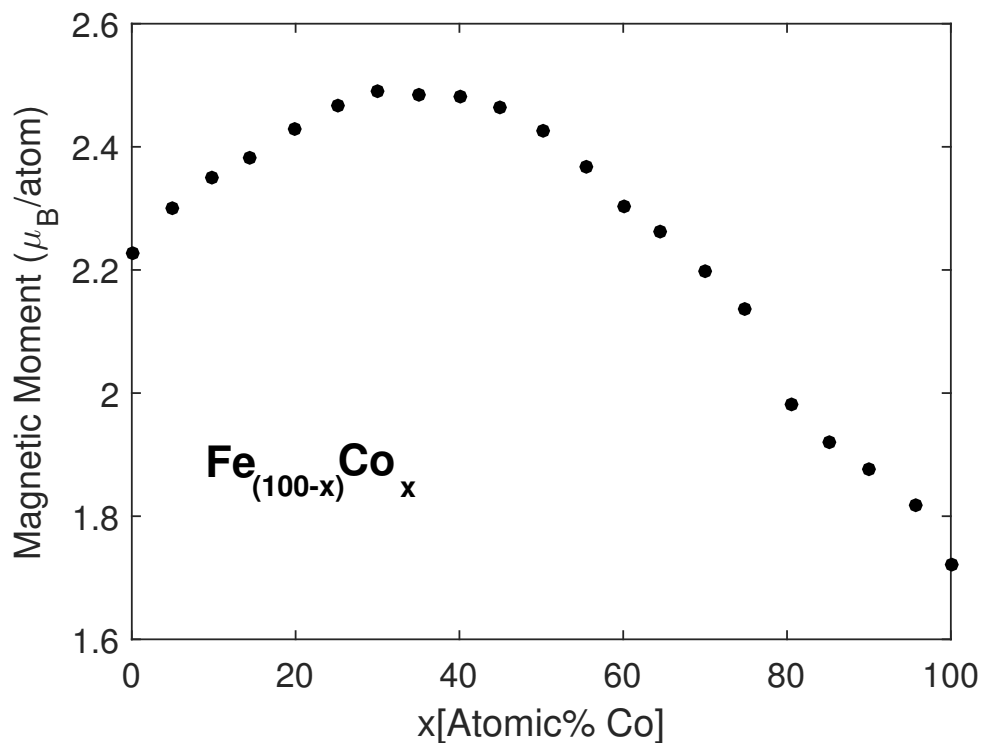


Figure 1.8: Fe-Co section of the Slater-Pauling Curve showing a peak of  $2.5\mu_B$ /atom occurring at Fe<sub>2</sub>Co [34].

### 1.3.2 Ferromagnetic Metallic Glasses

After metallic glasses were first developed by Pol Duwez in 1960, there was some debate over whether or not ferromagnetism could exist in them. This debate centered on if the amorphous structure of the glass would interfere with the exchange interaction between atoms. Later that same year though, Gubanov submitted a theory on amorphous ferromagnets, in which he found that there was no requirement for periodicity in the derivation for ferromagnetism [35]. Here, he presumed metallic glasses are made up of multiple types of atoms, but that only ferromagnetic atoms would be accounted for in terms of nearest neighbors. Taking

this one step further with the assumption that an amorphous metal would have a density corresponding to the radial distribution function, he could derive the Curie temperature for the metallic glass. With this theory in the literature, exploration for a ferromagnetic metallic glass began, with the first one, an Fe-P-C alloy, being discovered by Pol Duwez in 1967 [36]. This discovery highlighted the excellent soft magnetic properties of metallic glasses prompting interest in the commercial applications of these glasses. Since then a number of other ferromagnetic metallic glasses have been discovered, falling into either the transition metal-metalloid class, i.e. Fe-P-C, or the rare earth-transition metal class, i.e. Gd-Co [37].

Ferromagnetic metallic glasses are primarily of interest due to their excellent soft magnetic properties and for applications in those fields. Currently, soft magnetic metallic glasses are used in a wide variety of applications including the utility grid and consumer electronics as transformers, inductors, and amplifiers. The term "soft" magnet is in contrast to a "hard" magnet, where a soft magnet has a small coercivity and can easily change or lose its magnetization, and a hard magnet has a large coercivity, enabling it to keep its magnetization even when an opposing field is applied <sup>16</sup>. A schematic of the difference in the hysteresis curve of each can be seen in Figure 1.9, where the x-intercept represents the coercivity.

The soft magnetic properties of metallic glasses originates from two things: the homogeneity of the alloy, and the lack of large-scale defects. Metallic glasses have some chemical ordering on over a short range [38], but have atomic homogeneity at length scales comparable to the magnetic correlation length [39], giving them a low coercivity and a high permeability. In addition to this, metallic glasses lack dislocations, grain boundaries, and other extended defects associated with crystalline metals. As the domain walls move through the material, they interact with these defects<sup>17</sup>, and more energy is required to move them over the defect than

---

<sup>16</sup>The term soft and hard magnet originates from the first magnetic materials and the physical hardness of each type of magnetic material.

<sup>17</sup>In the traditional view of magnetic domain walls, defects and grain boundaries act as pinning

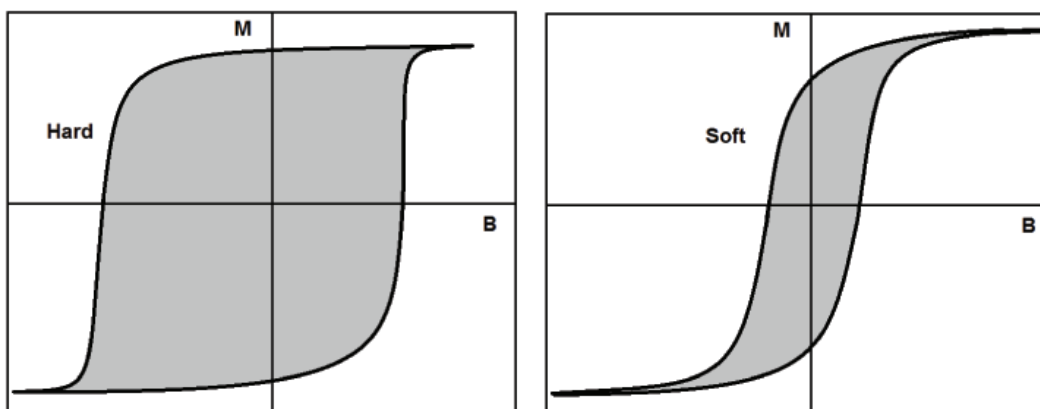


Figure 1.9: Depiction of the difference in the hysteresis curve between a hard and soft magnet. A soft magnet has a narrower curve due to its small coercivity.

through an ideal material. The lack of extended defects enables metallic glasses to have a low coercivity and be more efficient soft magnets. Two other properties of metallic glasses also contribute to their usefulness as soft magnets. They have no magnetocrystalline anisotropy due to their random structure, and this random structure also leads to large electrical resistivities [40], as seen in Table 1.1. The large resistivities are several times larger than those of the corresponding crystalline alloy, and lead to lower eddy currents in the material.

Composition	Electrical Resistivity [Ohm-m]
$\text{Fe}_{57.5}\text{Co}_{20.2}\text{Si}_{10.2}\text{B}_{2.1}\text{P}_{10}$	$1.34\text{e-}6$
$\text{Fe}_{68}\text{Mo}_4\text{Ni}_3\text{Co}_5\text{Si}_1\text{B}_{2.5}\text{P}_{11.5}\text{C}_5$	$1.38\text{e-}6$
$\text{Ni}_{80}\text{P}_{20}$	$1.35\text{e-}6$ [41]
$\text{Pd}_{40}\text{Ni}_{40}\text{P}_{20}$	$1.29\text{e-}6$ [42]
$\text{Fe}_{80}\text{B}_{20}$	$1.18\text{e-}6$ [43]
M4-grade silicon steel	46 [44]
H2-grade silicon steel	46 [44]

Table 1.1: Experimental resistivities(at RT) of metallic glasses and crystalline silicon steel. All resistivities are in Ohm-meters.

### 1.3.3 Eddy Currents

Eddy currents arise when there is a time changing magnetic field inside of conducting medium as can be derived from Faraday's law of induction. They are circular loops of electrical current that travel perpendicular to the direction of the changing magnetic field. As the eddy currents flow through the material, they generate Ohmic heat due to the resistance of the material:

$$\dot{Q} = \rho J^2 \quad (1.8)$$

Conversely, a large resistivity decreases the size of the eddy currents by reducing the flow of the electrons in the first place. A key reason for the use of metallic glasses as soft magnetic materials is their low eddy current losses. In addition to metallic glasses having high resistivities, their traditionally low glass forming ability is not always a disadvantage. Metglas is made into laminated cores, with alternating layers of nonconducting medium and metallic glass, a ~25 micron thick ribbon. Since the eddy currents are circular in nature and are reliant on the conducting, cross-sectional area that they can flow through, by separating the conducting layers, the eddy currents can be minimized. With the cross-sectional geometry of a toroidal core illustrated in Figure 1.10, the contributions to the eddy currents can be displayed in this equation [45]:

$$W_e = \frac{(\pi^2 f B_m^2 \tau^2)}{\beta R \rho} \quad (1.9)$$

where  $B_m$  is the max induced magnetization,  $\tau$  is the thickness as shown in Figure 1.10,  $R$  is the electrical resistivity,  $\rho$  is the density, and  $\beta$  is a geometric coefficient.  $\beta$  can range from 6 for ribbons to 16 for circular cross-sections, with  $\beta$  being equal

to [46]:

$$\beta = \frac{6}{1 - 0.633 \frac{\tau}{h} \tanh\left(1.58 \frac{h}{\tau}\right)} \quad (1.10)$$

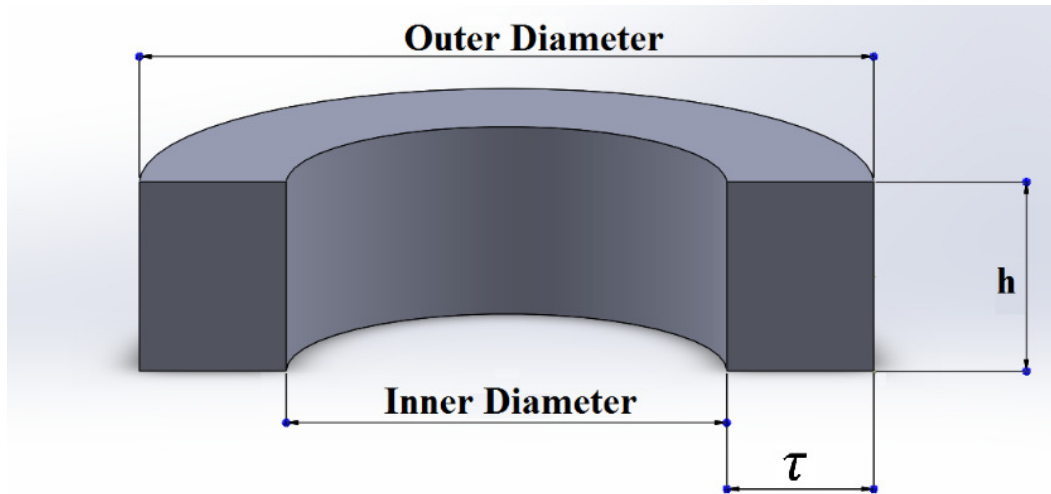


Figure 1.10: Cross-section of a toroidal core with a laminae or rectangular cross-section.

Equation 1.9 is only valid when the magnetic field can fully penetrate the thickness of the toroid. As the frequency of the time changing magnetic field increases, the domain walls in the material cannot flip fast enough if they are far from the surface of the material. This leads to a penetration depth, or skin depth,  $\delta$ , which shows the amount of material affected by the magnetic field and is expressed as [47]:

$$\delta = \sqrt{\frac{R}{\pi \mu_0 \mu_r f}} \quad (1.11)$$

where  $\mu_0$  is the permeability of free space, and  $\mu_r$  is the relative permeability. At low frequencies, the skin depth is greater than the thickness of the magnetic part and the inductive effects of eddy currents can be disregarded. This leads to Equation 1.9 being valid at low frequencies, but to correctly model  $W_e$  for any given frequency,

it changes to [48]:

$$W_e = \frac{3 \sinh(x) - \sin(x)}{x \cosh(x) - \cos(x)} \frac{(\pi^2 f B_m^2 \tau^2)}{\beta R \rho} \quad (1.12)$$

where  $x = \frac{\tau}{\delta}$ . These equations are the basis of modeling eddy current losses in a magnetic alloy. Nowhere in these equations is the periodicity or structure of the material referenced so the eddy current equations could be applied to both crystalline and amorphous materials. The one thing not taken into account is the dependence of some of the material properties. The density, resistivity, and permeability are all functions of the temperature, and the permeability is also a function of the frequency<sup>18</sup>.

### 1.3.4 Transformers

Transformers are a very large sector of soft magnetic components, and are the main soft magnetic application that I have focused on during my research. Transformers work in a very simple manner to change the voltage of electricity coming in at a different voltage, see Figure 1.11, but only work with AC currents. Electricity first comes in through the "primary" set of wires that is wrapped around one side of the transformer. This in turn generates a magnetic field every time the AC current switches direction, since the wire acts as a solenoid. The material switches the direction of its magnetic field at the same frequency as the primary current, which in turn generates an induced electric current in the secondary winding. If the number of windings differs between the primary and secondary winding then the voltage will be changed, with a larger number of secondary turns increasing the voltage and vice versa. The inefficiencies in this system come from the inherent electrical resistance in the wire, as well as from losses (eddy current losses among

---

<sup>18</sup>This frequency dependence of the permeability leads to problems fitting the data. In the magnetic samples we test in later chapters, the calculated eddy current losses exceed the measured total losses at high frequencies.

others) inside the transformer.

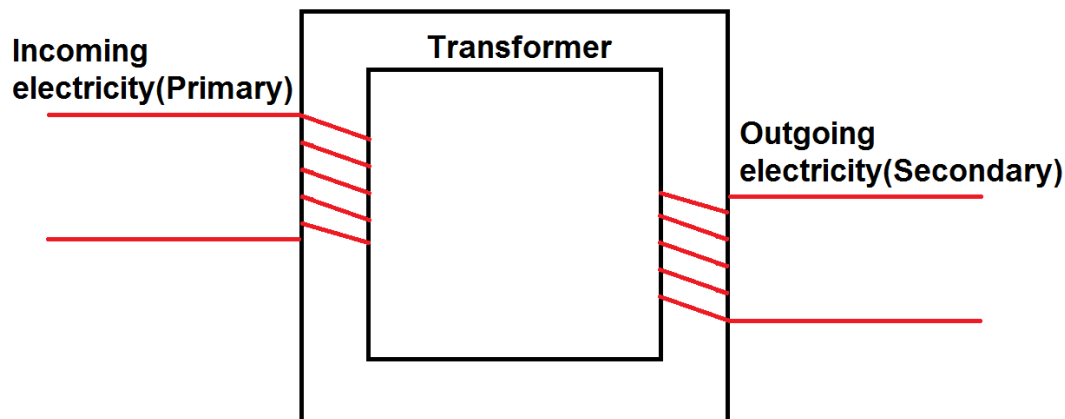


Figure 1.11: Diagram of a transformer.

Transformers best known application is on the power grid, with the trash can sized cylindrical metal boxes of the power lines being the user side transformer to transform the high grid transmission voltage of the electricity down to a usable voltage for your house or business. In addition to these transformers, there are transformers at substations that take in electricity from very high voltage, long distance power lines and transform it to a lower voltage for a city's power lines. Transformers are also at power plants to step up electricity from the generators to the transmission voltage. All of this is part of a system to efficiently transmit electricity from power plants to its end-use. The main reason why electricity is transformed to a high voltage is due to these equations:

$$P = V \cdot I \quad (1.13)$$

where P is the power, or rate at which the electrical energy flows, V is the voltage, and I is the current. This pairs with Ohm's Law:

$$I = \frac{V}{R} \quad (1.14)$$

where  $R$  is the resistance of the transmission medium, and the combination of the two equations yields:

$$P = I^2 \cdot R \quad (1.15)$$

So to maximize the amount of energy transmitted, while minimizing the amount of energy lost, the voltage of the electricity should be very large. These equations are for DC electricity, and while the grid in the U.S. uses AC electricity at 50 or 60 Hz, the conclusions drawn from here are applicable to AC as well. This system is the most efficient way to transmit electricity, but it does come with some inherent flaws. The one that matters to us is the current inefficiencies in transformers. Currently most transformers in the U.S. are made out of silicon-steel, which has a magnetic saturation of 2.03 T [44], and is roughly 97% efficient [16]. If silicon steel was to be replaced by Metglas, the best amorphous alternative, then the efficiency would increase to about 99.4%, but this has not occurred to any large degree in the U.S. due to the economics of the situation. If the price of metallic glass transformers were to decrease relative to silicon steel, or other factors began to contribute, i.e. global warming, then a transition to a more efficient transformer would be prudent and economical.

## 1.4 Review of Past Work on Ferromagnetic Metallic Glasses

Studies on ferromagnetic metallic glasses have been performed since the first days of metallic glasses. They have generally focused on the glass forming ability first, and once that plateaus, then the magnetic properties. In this thesis we follow a similar trend of first developing ferromagnetic metallic glasses for their glass forming properties and then narrowing in on the best magnetic material.

### 1.4.1 Alloy Development

Earlier in the introduction I described the history of metallic glasses and the initial development of Metglas, but since then there have been many advancements to the glass forming ability, soft magnetic properties, and other properties of ferromagnetic metallic glasses. The first push after the advent of Metglas<sup>19</sup>, Fe<sub>80</sub>B<sub>20</sub>, was to see what effect metalloids would have on the soft magnetic properties. The iron-boron system was first investigated [49] showing that the Fe:B ratio of 80:20 yielded a maximum in the saturation, striking a balance between a high Curie temperature and high ferrous metal percentage. From here the effects of phosphorous, carbon, and silicon were investigated as a function of their concentration. These elements were shown to either increase the magnetic saturation, or not effect it at their optimal concentrations for glass forming ability [50]. This is due to their expansion of the average Fe-Fe interatomic distance, or the lack of effect on it<sup>20</sup>. In addition to the investigation of the effect of metalloids, the role that cobalt and nickel play on the magnetic properties was also investigated. Ni- and Co- based ferromagnetic metallic glasses were developed in their own right, as well as how they impacted Fe-based alloys. The addition of cobalt yielded the highest saturation metallic glass of the time, Fe<sub>69</sub>Co<sub>18</sub>B<sub>13</sub>, but decreased the glass forming ability due

---

<sup>19</sup>While Metglas now is the trademark name for a number of different metallic glasses, initially it only referred to Fe<sub>80</sub>B<sub>20</sub>.

<sup>20</sup>From the initial theory on ferromagnetism in amorphous metals, we know that only the nearest neighbor interactions of ferromagnetic elements matters.

to the low metalloid percentage. This work paved the way for the high saturation Metglas, 2605, that was then developed [50]. Nickel on the other hand, does not increase the saturation of Fe-based metallic glasses at any concentration, and once the nickel concentration passes a certain threshold, the saturation decreases [51]. In addition to the magnetic properties being explored at this time, work was done to also improve and understand the mechanical properties, namely the ductility, but unfortunately Fe-based metallic glasses have remained brittle to this day<sup>21</sup>.

After the initial push to investigate Metglas and other Fe-based glasses, the development of bulk metallic glasses in the 90s sparked a secondary wave of research focusing on the glass forming ability of ferromagnetic glasses. In this wave, the role that nonferrous metals could play in enhancing the glass forming ability and other material properties was of primary interest, and while the magnetic saturation would decrease from their addition, some of the other magnetic properties could also be improved. The effects of W [52], Dy [53], Ga [54], Nb [55], Mo [56], Cr [57], and many other metals were explored with a wide range of effects, with nominal alloys shown in Table 1.2. These additions have the general property of increasing either the glass forming ability, the mechanical properties, or secondary magnetic properties (i.e. permeability, coercivity), but decreasing the magnetic saturation. In addition to this, there have been more recent attempts to increase glass forming ability without the use of nonferrous metals in attempts to retain a high magnetic saturation [28, 58, 59, 60].

#### **1.4.2 Losses**

The other foundational work that my research is based on pertains to the electrical losses in metallic glasses. I have already discussed eddy current losses, which have traditionally been assumed to be the primary loss, but this is just one

---

<sup>21</sup>While the ductility of metallic glasses as a whole has increased in the past two decades, Fe-based glasses have lagged behind in their increases to toughness. This is thought to be caused by the chemical bonds in Fe-based metallic glasses.

Composition	Critical Rod Diameter [mm]	Magnetic Saturation [T]
Fe <sub>81</sub> Si <sub>5.5</sub> B <sub>10</sub> P <sub>3.5</sub> [58]	ribbon	1.70
Fe <sub>76</sub> Si <sub>9</sub> B <sub>10</sub> P <sub>5</sub> [59]	2.5	1.51
Fe <sub>76</sub> Si <sub>5.7</sub> B <sub>9.5</sub> P <sub>5</sub> C <sub>3.8</sub> [60]	3	1.44
Fe <sub>75</sub> Mo <sub>4</sub> Si <sub>3</sub> B <sub>4</sub> P <sub>10</sub> C <sub>4</sub> [56]	4	1.27
Fe <sub>66</sub> Co <sub>10</sub> Mo <sub>4</sub> Si <sub>3</sub> B <sub>4</sub> P <sub>9</sub> C <sub>4</sub> [28]	6	1.19
Fe <sub>73.5</sub> Nb <sub>2</sub> Si <sub>3.3</sub> B <sub>5.5</sub> P <sub>8.7</sub> C <sub>7</sub> [55]	3	1.12

Table 1.2: Nominal alloys of interest in the literature. This is a brief overview of their magnetic properties.

type of loss. The total power loss ( $P_t$ , in units of W/kg) is an important figure of merit due to its relevance for the performance of soft magnets, and incorporates the three subsidiary loss types:

$$P_t = P_h + P_e + P_a \quad (1.16)$$

where  $P_h$ ,  $P_e$ , and  $P_a$  denote the hysteresis, eddy current, and anomalous losses. To find the total power losses per cycle ( $W_t$ , in units of J/kg)<sup>22</sup>, Equation 1.15 can be divided by frequency,  $f$ , to get

$$W_t = W_h + W_e + W_a \quad (1.17)$$

where the total losses per cycle,  $W_t$ , are a combination of the hysteresis,  $W_h$ , eddy current,  $W_e$ , and anomalous  $W_a$  losses. The hysteresis losses represent the losses at 0 Hz, and constant with frequency. Hysteresis losses originate from the magnetization of the material, from the rotation of the magnetic domains and their coalescence into a unified domain[29]. This time-independent rotation must overcome inherent fields in the material, as well as material imperfections, which causes the rotation to

<sup>22</sup>We will be using losses per cycle as the standard measure of the losses for a material.

be an irreversible process [61]. Hysteresis losses are usually considered inherent to the material, and inconsequential in comparison to eddy current losses. Anomalous losses have also been considered inconsequential, and were introduced to remedy inconsistencies between theory and experiments carried out on eddy currents[62]. These losses are surmised to originate from the velocity of the domain wall, the collapse of individual domains, or the interaction between the domain walls and the surface. Unfortunately, despite eighty years of study they are still not well understood, and only basic equations map their general reliance on frequency, max magnetization, and geometry[63].

The idea that eddy current losses are the only losses of consequence has started to be upended though, with work on how the total losses are dependent on the geometry first bringing this to light. This change in thought can be seen in a paper by Schwarz [46], and Figure 1.12. Schwarz found that even though the eddy current losses decrease with decreasing thickness, the anomalous losses increase. This leads to a higher total loss for thinner samples, and contradicts the traditional picture of eddy current loss dominance. It is this paper that spurred our interest in bulk metallic glasses as power transformers, leading us to believe that more efficient metallic glass power transformers could be made with bulk metallic glasses instead of ribbons.

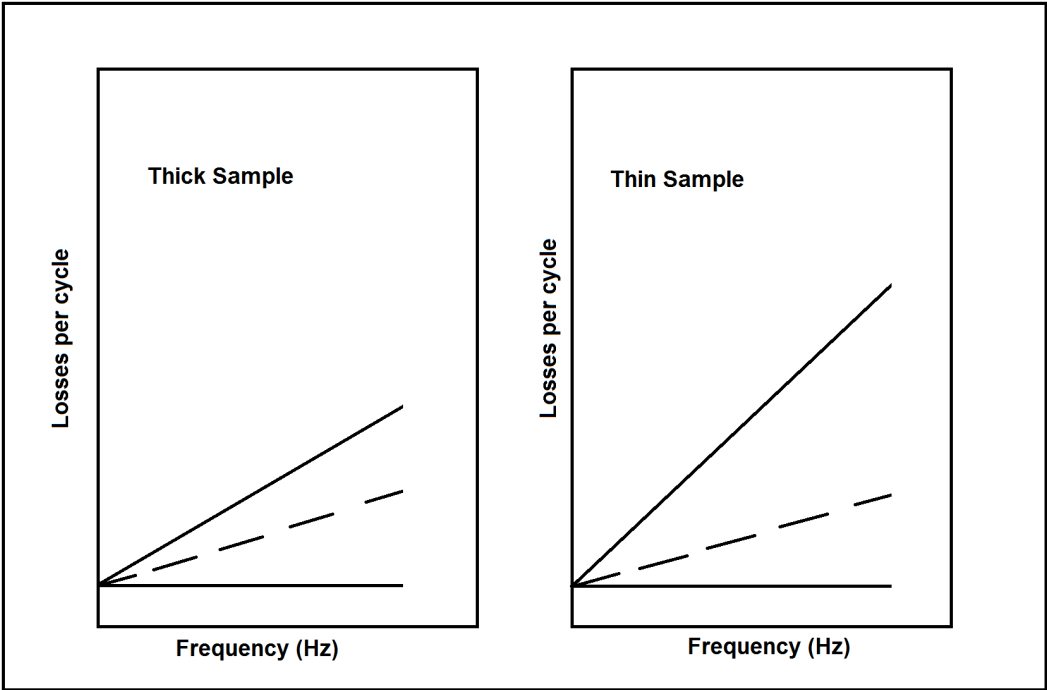


Figure 1.12: Schematic of results from paper by Schwarz [46]. While the eddy current losses decrease with the core thickness, the total losses increase due to increasing anomalous losses.

## 1.5 Key Contributions

The key contributions made in this thesis fall into three categories: (1) the development of an Fe-based metallic glass system which combines a large glass forming ability with a high magnetic saturation, (2) the creation of processing procedures for magnetic metallic glasses and the discovery of a chemical reaction in a known fluxing procedure, and (3) further discovery of the underlying losses which control the efficiency of power transformers.

Chapter 2 outlines the development of a ferromagnetic metallic glass. We focus on three properties during alloy development: (1) glass forming ability greater than 3 mm, (2) magnetic saturation above 1.2T, and (3) the exclusion of non-ferrous metals<sup>23</sup>. The alloy that is developed has a composition of  $\text{Fe}_{57}\text{Co}_{20}\text{Si}_{7.5}\text{B}_{5.5}\text{P}_{10}$ , and meets all three of the criteria with a critical rod diameter of 4 mm, and a magnetic saturation of 1.57. This alloy is unique in its combination of high saturation and large critical rod diameter. Unfortunately, this alloy also has issues with reproducibility, which are further explored in Chapter 3 where the reproducibility issues are solved and a different alloy in the same family is presented.

Chapter 3 delves into the process of fluxing, and the chemical reactions potentially occurring at this stage. The classical view of fluxing is found to be lacking when silicon is present, with Si causing a redox-reaction to occur with the flux. The change in the composition due to the reaction is explored, and then utilized in the alloy development of the nominal alloys listed in Table 1.3. We also found this reaction to be present during the fluxing of other metallic glasses<sup>24</sup>, both Pd-based and Ni-based.

Chapter 4 moves into the processing and machining of cores for magnetic testing, and is mostly a methods section for Chapter 5. We explore several different

---

<sup>23</sup>This is to cut down on the cost of the material, to increase the saturation, and is an exercise in utilizing several alloy development tools that we have begun to use.

<sup>24</sup>These alloys have been used/fluxed for over 30 years

Composition	Critical Rod Diameter [mm]	Magnetic Saturation [T]
$\text{Fe}_{57.5}\text{Co}_{20.2}\text{Si}_{10.2}\text{B}_{2.1}\text{P}_{10}$	5	1.53
$\text{Fe}_{68}\text{Mo}_4\text{Ni}_3\text{Co}_5\text{Si}_1\text{B}_{2.5}\text{P}_{11.5}\text{C}_5$	12	1.15

Table 1.3: Compositions of the two alloys developed from our new understanding of fluxing, along with their key material properties.

methods to make a core, and why we choose to cast in quartz tubes. We go on to describe how and why we anneal (both stress and magnetic annealing) the magnetic cores. In addition, we outline the machining method used, Electric-Discharge machining, and the reasoning behind using this process. Finally, we will introduce the magnetic testing performed on the magnetic cores, and describe the process for assembling the magnetic plots used throughout this thesis.

Chapter 5 focuses on minimizing the losses in a core. We first develop the theory around the other types of losses in a core, and how they can be reduced before we develop a hypothesis for their minimization. This theory is based on Schwarz's paper[46], and presents the idea of how a varying thickness yields a minimum in the total losses. Our initial hypothesis of a minimum in the losses at a given thickness is proved albeit with some caveats. We also theorize on the origin of this minimum in the total losses originating from the eddy current losses and anomalous losses being dominant in different geometries.

Finally, Chapter 6 offers my concluding thoughts. Future research topics that could be explored based on my work are brought up, and the contributions of my work are summarized.

*Chapter 2***ALLOY DEVELOPMENT OF A FE-BASED METALLIC GLASS  
WITH EXCELLENT SOFT FERROMAGNETIC PROPERTIES**

The impetus for this chapter and for other chapters in this thesis came from talks between Dr. Carl Johnson and Professor William Johnson. Dr. Carl Johnson represented the II-VI Foundation and was interested in projects relating to improved materials for energy storage and transmission as it related to the grid. He came to Professor Johnson looking for a metallic glass which could outperform the current best material, Metglas. It was from here that our original hypothesis emerged: that a bulk metallic glass could be developed which exhibited excellent soft magnetic properties while still forming a bulk metallic glass. This initial meeting spurred years of future collaboration, yielded multiple papers, and is responsible for the majority of the work I have done at Caltech. In this section we expanded on the two initial characteristics of the metallic glass to add: an alloy with a low price per pound, and an alloy which could be produced on a commercial scale. We hypothesized that we could do this by keeping out all non-ferrous metals, which can aid in glass forming, but decrease the magnetic saturation and are typically more expensive. By pairing this restriction with the alloy development tools that I had previously worked on, we eventually succeeded in our goals.

## 2.1 Abstract

A bulk metallic glass with a high glass forming ability, and excellent soft-magnetic properties was developed with a composition of  $\text{Fe}_{57}\text{Co}_{20}\text{Si}_{7.5}\text{B}_{5.5}\text{P}_{10}$ . A 4 mm rod was cast through a refined fluxing procedure and without the inclusion of nonferrous transition metals. The cobalt concentration was optimized for glass forming ability and coincided with a peak in the Slater-Pauling curve. This resulted in an alloy with a magnetic saturation of 1.57 T, coercivity of 2.3 A/m, relative permeability of 58,480, and Curie temperature of 730 K. This is the highest saturation for a ferromagnetic bulk metallic glass (critical rod diameter  $\geq 3$  mm) reported to date.

## 2.2 Introduction

Ferromagnetic metallic glasses have been of interest since their discovery in 1967 [2], due to their low coercivities and high magnetic permeabilities, arising from atomic homogeneity at length scales comparable to the magnetic correlation length [39]. These soft magnetic properties have led to their widespread use in automotive magnetics, magnetic sensors, power supplies, and power transformers [64]. Currently, commercially available ferromagnetic metallic glasses are produced via the rapid quench process of melt spinning, producing cooling rates ranging between  $10^4 - 10^6$  K/s. These rapid cooling rates are required for glass formation [15], but also limit the thickness of the metallic glass ribbon to micrometer thicknesses. To decrease the cooling rate requirements, and increase the critical casting thickness of these metallic glass ribbons, nonferrous metals such as Ga [46], Cr [65], Nb [55], Mo [56], and Zr [21] have been added to great effect. While being beneficial to the glass forming ability, they also come with the side-effect of decreasing the magnetic saturation, as these non-ferrous metals tend to reduce the magnetic moment per atom of the alloy. Li et al [59] found that the critical casting thickness can be increased without the use of non-ferrous metals by utilizing recent alloy development techniques. Using this idea, we create a ferromagnetic metallic glass with both a large glass forming ability and a high magnetic saturation. This expands the possible applications for ferromagnetic bulk metallic glasses and furthers the understanding of alloy development for metallic glasses.

In our research, we attempted to develop a Fe-based metallic glass both a large critical casting thickness and good soft-magnetic properties. To do this we constrained our optimization process to exclude nonferrous transition metals; this restriction limits the glass forming ability, but maintains a high magnetic saturation. Using Na et al.'s idea of a compositional landscape [27], we optimized the alloy composition to fall between competing crystalline phases and on a cusp in GFA.

This cusp roughly corresponded to the peak in magnetic moment found in the Slater-Pauling curve[34], which occurs at a 2:1 iron to cobalt ratio. Through these development models, along with our quenching and overheating methods, we developed a ferromagnetic bulk metallic glass with a composition of  $\text{Fe}_{57}\text{Co}_{20}\text{Si}_{7.5}\text{B}_{5.5}\text{P}_{10}$ . This novel composition has a magnetic saturation of 1.57 T, DC coercivity of 2.3 A/m, DC permeability of 58,480, and GFA of 4 mm; a unique combination of high magnetic saturation and large GFA.

### 2.2.1 Quenching

There are three major ways that metallic glasses have been historically quenched: spin-casting, copper mold casting, or quartz casting. Spin-casting<sup>1</sup> was not the first quenching method developed, but it was widely used to achieve the necessary cooling rates for glass formation in the early days of metallic glasses. The other two quenching techniques were pioneered in the 1980s, during the advent of bulk metallic glasses, and are commonly used today for alloy development. Copper mold casting, as seen in Figure 2.1, is used more commonly than quartz casting due to its ease of use and ability to handle most elements. It utilizes an Arc-melter to

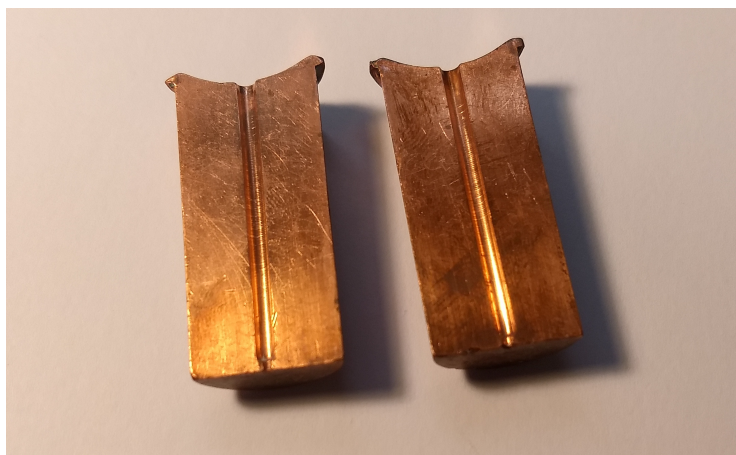


Figure 2.1: A Copper mold used in copper mold casting of bulk metallic glasses.

---

<sup>1</sup>Also known as melt-spinning.

melt the alloy, and then uses suction casting to vitrify the molten alloy. In addition to being able to reuse the molds, spin-casting also has a very high cooling rate due to the high thermal conductivity of the copper<sup>2</sup>, especially if the alloy wets the surface of the mold. Despite this, our group no longer utilizes copper mold casting for alloy development for two reasons: (a) the arc used to melt the alloy can easily evaporate the phosphorous contained in some alloys, and (b) since the alloy is injected and cooled in one step, the alloy does not cool solely by conduction, and is instead dependent flow of the liquid into the mold and convection.

Instead our group has utilized the quartz-casting method. There are several downsides to this approach, namely: (1) lower cooling rate due to the low conductivity of quartz, (2) new tubes must be made for each casting, and (3) alloys that easily form oxides can react with the quartz. Although we constantly need new tubes,



Figure 2.2: A photo of two thin walled quartz tubes with differing diameters, and a quartz capillary.

our lab makes our own quartz tubes, as seen in Figure 2.2, allowing us to make

---

<sup>2</sup>Copper has a thermal conductivity(K) of  $\sim 400 \frac{W}{m-K}$ .

any geometry needed at a moments notice. By using quartz tubes and capillaries we also decouple the heat transport from flow of the material, allowing for more reproducible cooling. In quartz casting, we inject the molten alloy into the quartz tube using an argon back-pressure, and then quench filled tube in a proprietary, water-based solution. This allows us to measure the differences in glass forming ability more exactly since we only are dealing with heat transport by conduction. The liquid in the tube is essentially quiescent<sup>3</sup> during cooling. Therefore, the cooling rate is governed by a transient solution to the Fourier heat flow equation, which is both predictable and reproducible.

### 2.2.2 Overheating

Another process that we undertake during alloy development is the overheating of the molten alloy [66]. As seen in Figure 2.3, there is a dramatic shift in both the glass forming ability and the toughness of the alloy depending on the overheating temperature that the alloy is quenched from. While the liquidus of the alloy in Figure 2.3 is  $\sim 870^{\circ}\text{C}$ , there is a large change in the glass forming ability which takes place at an overheating temperature of  $\sim 1125^{\circ}\text{C}$ . We term this secondary temperature the critical glass forming temperature ( $T_{GFA}$ ). This change in the glass forming ability is thought to be caused by the further melting trace oxide phases, inclusions that act as heterogeneous nucleation sites below some threshold overheating temperature. The other temperature of note, which we term the critical toughness temperature ( $T_{tough}$ ) occurs at  $\sim 1250^{\circ}\text{C}$ , and is caused by a further melting of impurity phases in the melt. These inclusions seem to act as stress concentrators, or crack nucleation sites, which lower the fracture toughness of the metallic glass. By casting our alloys above these two temperatures we can ensure that the properties measured are not affected by inclusions in the material, allowing for more systematic alloy development.

---

<sup>3</sup>Does not flow.

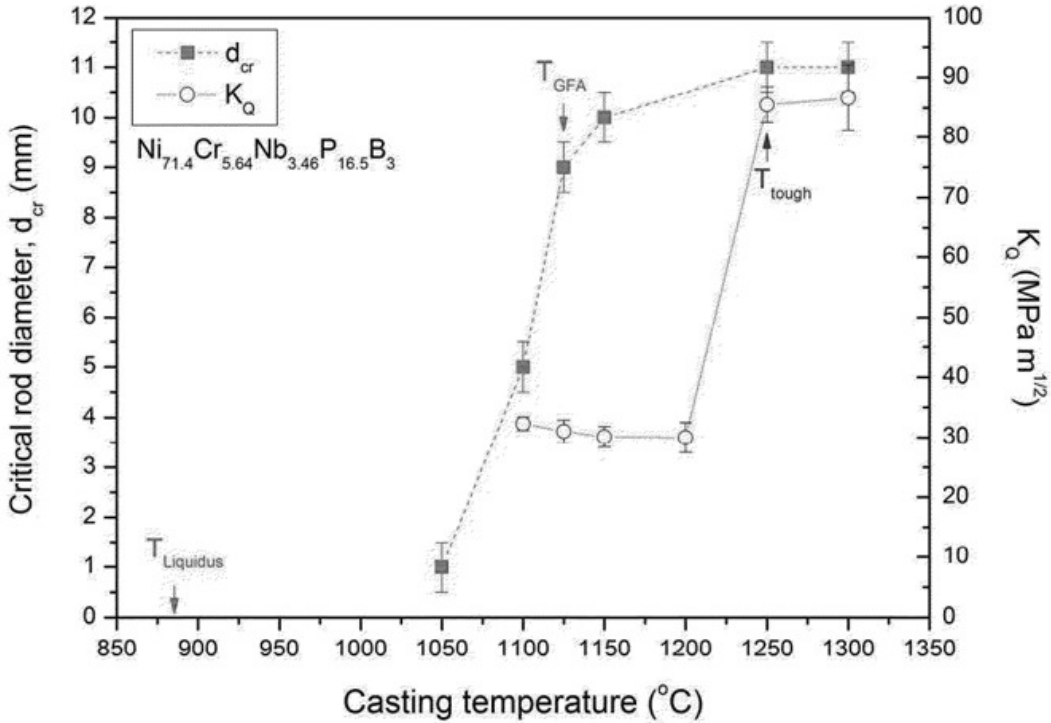


Figure 2.3: Data on the effects of the overheating temperature on the glass forming ability and toughness of an alloy [66]

### 2.3 Method

Metallic glass ingots were prepared by induction melting mixtures of the appropriate amounts of iron (99.95%), cobalt (99.95%), boron (99.5%), silicon (99.9999%), platinum (99.99%), palladium (99.995%), and phosphorous (99.999%) in sealed quartz tubes under an Ar atmosphere [67]. With these compositions being in nominal atomic percent. The ingots were fluxed with dehydrated boron oxide in a vertical tube furnace at 1300°C for 20 minutes and quenched. The molten alloy is then heated to 1400°C and allowed to equilibrate before being injected into a quartz tube using an argon back-pressure. It is subsequently water quenched from 1400°C.

The amorphicity of the quenched rods was evaluated using X-ray diffraction (XRD) with Cu- $K\alpha$  radiation. Differential scanning calorimetry (DSC), at a heating rate of 20K/min, was used to determine the Curie temperature ( $T_c$ ), glass transition temperature ( $T_g$ ), crystallization temperature ( $T_x$ ), solidus temperature ( $T_s$ ), and liquidus temperature ( $T_l$ ) for each composition. For magnetic testing, 4 mm rods were stress annealed at 60 K below  $T_g$  for 45 minutes to relax any quenched-in internal stresses induced by the rapid cooling process [46]. Disks sectioned from a 4 mm rod were electric discharge machined into toroids having an external diameter of 3.95 mm, an internal diameter of 3.4 mm, and a height of 0.84 mm. The toroids were then wrapped with a 30-AWG insulated copper wire producing 20 primary turns and 20 secondary turns. The magnetic properties of the cores were characterized using a Walker AMH-200k-S Hysteresisgraph at 50 Hz frequency and 25 kA/m magnetic flux, and the permeability/coercivity were measured as a function of frequency.

## 2.4 Results

To achieve a large GFA we followed the general guidelines for alloy development: (1) start with a composition near a deep eutectic, (2) have at least a four component system, (3) have negative heats of mixing among the constituent elements, (4) remove impurities from the melt through a combination of flux and overheating, and (5) have a large size difference among the elements[21],[20]. We started with a eutectic composition of  $\text{Fe}_{83}\text{B}_{17}$ . As seen in Figure 2.4, the iron-heavy eutectic composition has a low liquidus temperature, thus shrinking the temperature range needed to cool through to achieve a glass. We started with boron instead of another metalloid element since that is the base for Metglas [15], and the addition of boron has limited effect on the ferromagnetism beyond diluting the iron concentration.

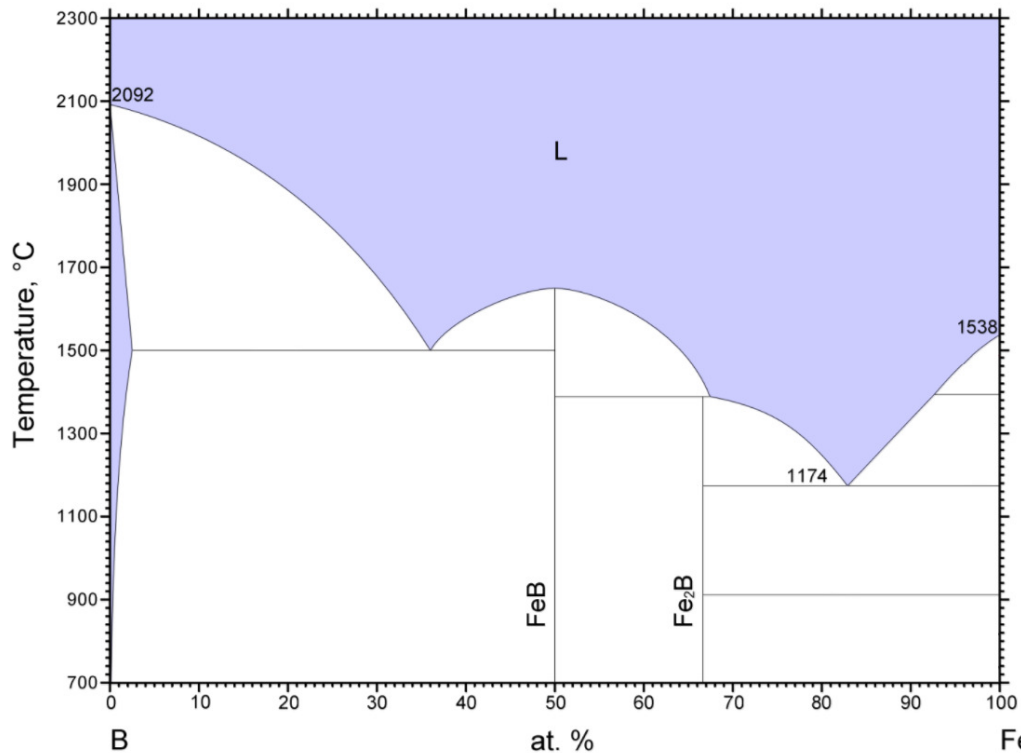


Figure 2.4: Fe-B phase diagram adapted from [68], through the use of the ASM Phase Diagram database.

From this starting point, we implemented a "biased random walk" algorithm to find local maxima in the glass forming ability. To do so, we began by adding silicon to our binary eutectic composition. Silicon is a good candidate for addition to the binary alloy since it matches most of the criteria outlined above. First of all, from analysis of ternary phase diagrams, and verification by DSC, we find that silicon decreases the melting temperature. It increases the number of components in the system and the variation in atomic radii [69], with silicon having an atomic radius of 111 pm, while Fe has a radius of 126 pm, and boron a radius of 180 pm. Silicon has also been shown to allow for boron oxide fluxing to work in alloy systems where it previously had no impact and silicon has a negative heat of mixing with iron and boron [70]. In addition to the glass forming criteria that silicon meets, it also has been shown that silicon has a slightly beneficial impact on the magnetic properties of iron alloys [71]. Finally, upon optimizing the metal-metalloid ratio we found that the optimal ratio was not at the Fe-B eutectic percentage of 17 at.% metalloids, but rather at 23 at.%. Using the following equation, we can find the theoretical eutectic composition and see how close 23% is:

$$X_a \cdot E_a + X_b \cdot E_b + X_c \cdot E_c \dots = X_t \cdot E_t \quad (2.1)$$

where  $X$  is the atomic percentage of each metalloid element and  $E$  is eutectic composition for that element and iron. Due to Fe-Si having a eutectic at  $\sim 30\%$ , as we add in more silicon to the alloy, the eutectic for the alloy should theoretically shift to a higher metalloid composition. This leads us to a theoretical eutectic composition ( $E_t$ ) of 21.5% metalloids for our final ternary composition of  $\text{Fe}_{77}\text{B}_{15}\text{Si}_8$ . While we found the optimal metal to metalloid ratio to be 77:23, this agreement suggests that the best glass former is close to, if not at, the eutectic composition. Due to the inexactness of the applied equation, along with the best glass former not always being exactly at the eutectic, this proximity satisfies our desire to have a low melting

point composition.

From here, we added ferrous metals, cobalt and nickel, in the place of iron. We chose these two metals since they are ferrous transition metals, and they have negative heats of mixing with the metalloid elements we had chosen so far. While we found nickel to have a detrimental effect on GFA, cobalt showed great promise across a broad spectrum of compositions as seen in Figure 2.5. As we follow the formula  $\text{Fe}_{77-x}\text{Co}_x\text{Si}_8\text{B}_{15}$ , cobalt improved the GFA with the optimal amount of cobalt occurring at roughly 17 at.%. If we look back at the Slater-Pauling curve in Figure 1.8, we can see that this amount of cobalt should also increase the magnetic moment of the alloy.

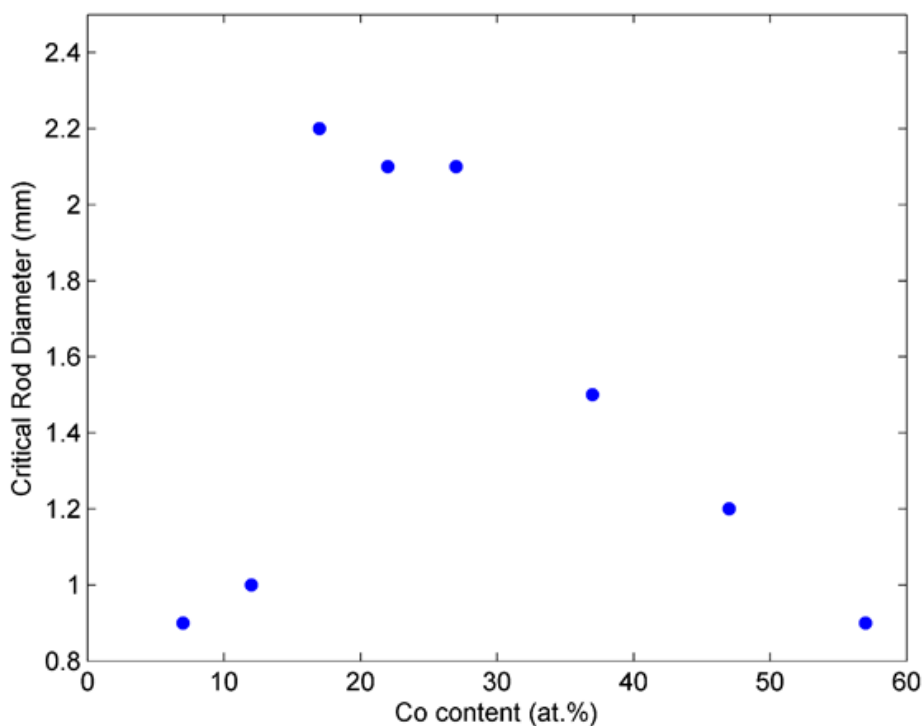


Figure 2.5: Peak in the glass forming ability of the Fe-based alloy as we vary the cobalt concentration following:  $\text{Fe}_{77-x}\text{Co}_x\text{Si}_8\text{B}_{15}$ . There is no obvious cusp in the glass forming ability as described by Na[27], but rather a plateau ranging from 17-27% Co.

After adding cobalt, we still had not achieved the glass forming ability of

greater than 3 mm<sup>4</sup> set as a primary objective. We had only reached a critical rod diameter of 2.2 mm for casting Fe<sub>60</sub>Co<sub>17</sub>Si<sub>8</sub>B<sub>15</sub> inside of a capillary(see figure 2.2). This is well below desired glass forming ability since the wall thickness of a capillary is ~0.1 mm while the wall thickness of a quartz tube is 0.5 mm. Thinner capillary walls enable the molten alloy to cool more quickly, and roughly translates to casting in a quartz tube one third the diameter of the capillary. With a greater critical rod diameter needed, and no further metal elements to explore, we returned to adjusting the metalloids, and added phosphorous to the alloy in place of boron. We had initially avoided phosphorous in our alloy since it can be problematic for processing (with the phosphorous easily sublimating before it alloys with the melt), even though it meets all the criteria for increase glass forming ability. With the addition of phosphorous we improved the glass forming ability enough to negate the side, increasing the critical rod diameter to 1.5 mm when casting Fe<sub>60</sub>Co<sub>17</sub>Si<sub>8</sub>B<sub>7</sub>P<sub>8</sub> in a quartz tube from previous maximum thickness of 2.2 mm when casting Fe<sub>60</sub>Co<sub>17</sub>Si<sub>8</sub>B<sub>15</sub> in a capillary.

From here, we wanted to once more optimize our alloy for glass forming ability, so we repeated our biased random walk approach. In Tables 2.1-2.3, some of the biased random walk results can be seen for a small selection of the alloys made. Table 2.1 shows the effect on the critical rod diameter as we increase the amount of phosphorous in substitution for equal parts boron and phosphorous. The critical rod diameter approaches a maximum of 2.5 mm as the phosphorous concentration increases before decreasing again beyond 10 at.% P. Similar maxima can be found in Tables 2.2 and 2.3. Table 2.2 shows show the effect of substituting boron for silicon, allowing for an increase in the critical rod diameter to 3 mm. Table 2.3 shows the effect of altering the metals to metalloids ratio, with the old optimized ratio still being the best. After these random-walk optimizations, we reached a critical rod

---

<sup>4</sup>As measured in a thin-walled, quartz tube.

diameter of 3 mm<sup>5</sup>, our desired goal.

Fe	Co	Si	B	P	Critical Rod Diameter [mm]
60	17	8	7	8	1.5
60	17	7.5	6.5	9	2
60	17	7	6	10	2.5
60	17	6.5	5.5	11	1.5

Table 2.1: Effect on the critical rod diameter of replacing phosphorous with silicon and boron. All reported compositions are in atomic percent and all critical rod diameters are for quartz tubes.

Fe	Co	Si	B	P	Critical Rod Diameter [mm]
60	17	6.5	6.5	10	2
60	17	7	6	10	2.5
60	17	7.5	5.5	10	3
60	17	8	5	10	1.5

Table 2.2: Effect on the critical rod diameter of replacing silicon with boron. All reported compositions are in atomic percent and all critical rod diameters are for quartz tubes.

Fe	Co	Si	B	P	Critical Rod Diameter [mm]
60.39	17.11	7.34	5.38	9.78	2
60	17	7.5	5.5	10	3
59.61	16.89	7.66	5.62	10.22	2

Table 2.3: Effect on the critical rod diameter of the metal to metalloid ratio. All reported compositions are in atomic percent and all critical rod diameters are for quartz tubes.

At this point in the alloy development we had reached our initial goals of creating a bulk metallic glass that contained no non-ferrous metals, but we had not yet explored its magnetic properties. From the Slater-Pauling curve in Figure 1.8 though, we knew that if we could increase the cobalt concentration further, then we theoretically would increase the magnetic moment of the alloy. Furthermore, looking at Figure 2.5, what appeared to be a peak in the critical rod diameter at 17 at.% Co could also be more of a plateau, with the actual peak in the middle of

<sup>5</sup>All critical rod diameters reported in Tables 2.1-2.3 are for quartz tubes.

the plateau. That being the case, we went back to our optimization of the cobalt in the system. In Figure 2.6, we plot the critical rod diameter versus the atomic concentration of cobalt. As seen in Figure 2.6, cobalt improves the critical rod diameter to 4 mm, when the cobalt concentration is adjusted to 20 at.%. Unlike in Figure 2.5, the critical rod diameter now forms an exponential cusp in accordance with Na et al's predictions[27], verifying that we have found the local maximum in glass forming ability! The lack of a cusp in the previous figure for critical rod diameter versus cobalt concentration was most likely resulting from the other unoptimized elements in the alloy, or from moving along a ridge in the glass forming ability instead of coming to a peak.

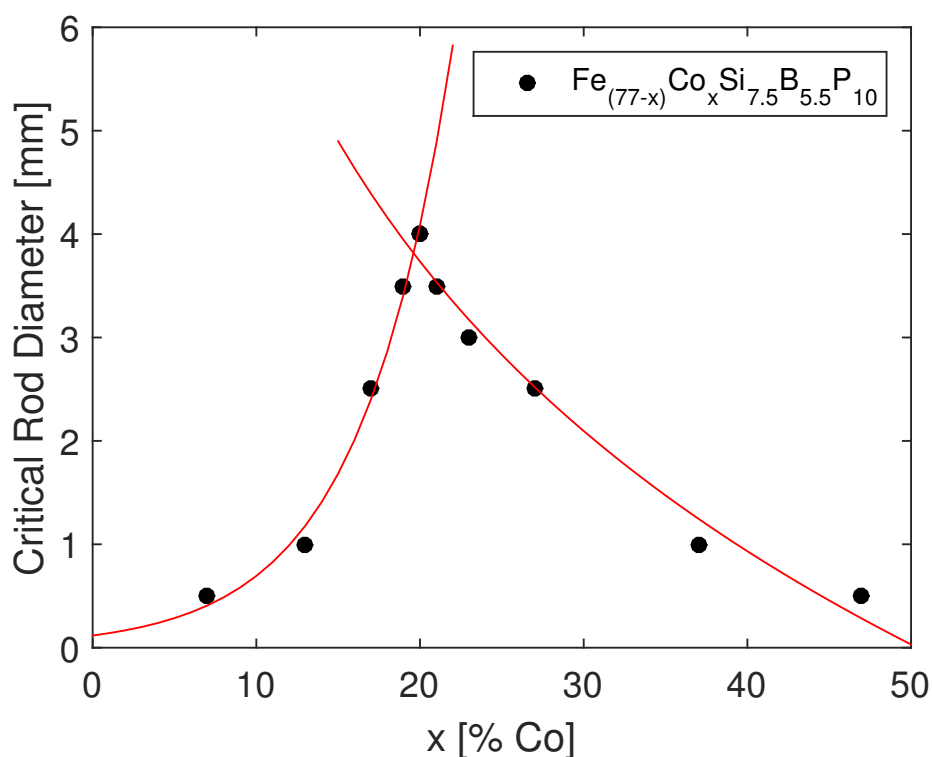


Figure 2.6: Cusp in the glass forming ability of the Fe-based alloy as we vary the cobalt concentration. We follow the formula:  $\text{Fe}_{77-x}\text{Co}_x\text{Si}_{7.5}\text{B}_{5.5}\text{P}_{10}$ .

With a final composition arrived at<sup>6</sup>, we turned to testing the magnetic properties of the alloy using a Walker AMH-200k-S Hysteresisgraph. The hysteresis

<sup>6</sup>While we had set out to optimize our alloy for glass forming ability and magnetic properties,

loop for  $\text{Fe}_{57}\text{Co}_{20}\text{Si}_{7.5}\text{B}_{5.5}\text{P}_{10}$  can be seen in Figure 2.7. Instead of the open hysteresis curves seen in Figure 1.9, this hysteresis curve is an extreme version of the soft magnet example and almost follows back along itself due to two main factors. The first of these is that we have an amorphous metal. The lack of grain boundaries, crystal orientations, and defects removes most of the pinning sites in the material, which allows the domain walls to traverse the material more easily. Secondly, the toroidal shape of the sample, as described in the section 2.3, and the low frequency of 50 Hz help to minimize the eddy current losses. In addition to the very small area inside the curve, this material exhibits a magnetic saturation of 1.57 T, well above the reported magnetic saturations of other ferromagnetic bulk metallic glasses in the literature. This is due both to the optimized ratio of Co to Fe, as well as the high percentage of ferrous metals.

In Figure 2.8 we plot the relative permeability ( $\mu_r$ ), and coercivity ( $H_c$ ) of  $\text{Fe}_{57}\text{Co}_{20}\text{Si}_{7.5}\text{B}_{5.5}\text{P}_{10}$  as functions of frequency. Both of these behave as expected from other magnetic materials with the highest permeability/lowest coercivity occurring at near DC frequency. Due to the restrictions of the measurement equipment, both of these values are measured between 100 Hz and 200,000 Hz and then extrapolated to a frequency of 0 Hz. This gives a DC relative permeability of 58,480, where relative permeability is:

$$\mu_r = \frac{\mu}{\mu_0} \quad (2.2)$$

where  $\mu$  is the permeability of the sample and  $\mu_0$  is the permeability of free space. This relative permeability is in line with other ferromagnetic, metallic glasses. The coercivity is representative of the hysteresis losses in the material and is a measure of the magnetic field required to demagnetize a ferromagnetic material.

---

we ended up only optimizing for glass forming ability. If we had reached the threshold critical rod diameter and still had more composition space left to adjust, then we would have started to look at magnetic properties sooner in our study.

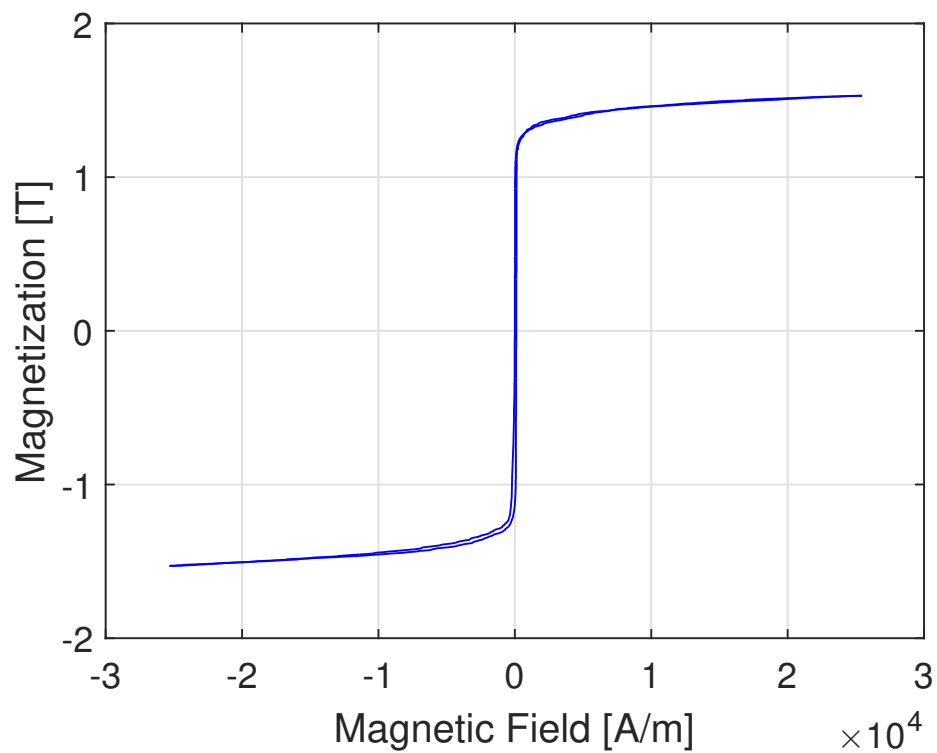


Figure 2.7: Hysteresis curve for  $\text{Fe}_{57}\text{Co}_{20}\text{Si}_{7.5}\text{B}_{5.5}\text{P}_{10}$  run at 50 Hz and 25 kA/m. This alloy has a magnetic saturation of 1.57 T.

$\text{Fe}_{57}\text{Co}_{20}\text{Si}_{7.5}\text{B}_{5.5}\text{P}_{10}$  has a coercivity of 2.3 A/m, which is comparable to other soft-magnetic metallic glasses. The change in both as the frequency increases deteriorates faster than in some comparable systems, but this can be mitigated by magnetic annealing[72].

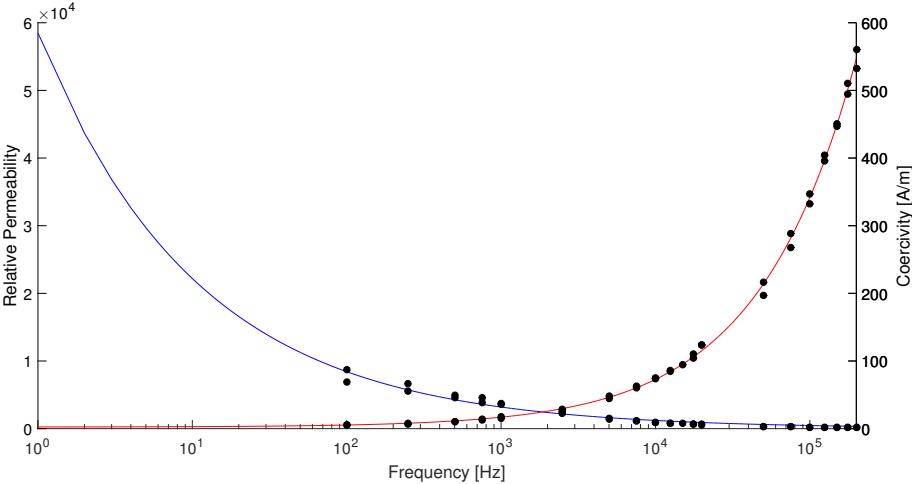


Figure 2.8: Permeability and coercivity of  $\text{Fe}_{57}\text{Co}_{20}\text{Si}_{7.5}\text{B}_{5.5}\text{P}_{10}$  as a function of frequency. At a DC frequency  $\text{Fe}_{57}\text{Co}_{20}\text{Si}_{7.5}\text{B}_{5.5}\text{P}_{10}$  has a permeability of 58,480 and a coercivity of 2.3 A/m

## 2.5 Conclusion

A few major takeaways from this chapter: (1) the addition of cobalt simultaneously increases the glass forming ability and magnetic saturation, (2) Fe-based metallic glasses can attain large glass forming ability despite a lack of glass-forming (non-ferrous) metals, and (3) the high saturation magnetization of 1.57T is higher than that for any previously reported ferromagnetic bulk metallic glass (with critical rod diameter  $\geq 3$  mm).  $\text{Fe}_{57}\text{Co}_{20}\text{Si}_{7.5}\text{B}_{5.5}\text{P}_{10}$  has a large critical rod diameter of 4 mm, does not contain any non-ferrous metals, and has a magnetic saturation of 1.57 T. In addition to this,  $\text{Fe}_{57}\text{Co}_{20}\text{Si}_{7.5}\text{B}_{5.5}\text{P}_{10}$  has a permeability of 58,480 and a coercivity of 2.3 A/m.

Despite the excellent properties of this alloy, it is an unsatisfactory material at this point. The reason for this is its lack of reproducibility. In our lab, when we develop novel alloys, we have a reproducibility at its critical rod diameter of  $\sim 90\%$ . On the other hand,  $\text{Fe}_{57}\text{Co}_{20}\text{Si}_{7.5}\text{B}_{5.5}\text{P}_{10}$  has a reproducibility of  $\sim 30\%$ . This lack of reproducibility made the alloy results unpublishable until it could be reproduced with greater success, and the reason for its poor reproducibility understood. After analyzing a number of possible problems, including the casting temperature, the loss of phosphorous, the source of our elements, leaks in our vacuum system, and quenching solution, we came upon the actual problem, which we go over in great detail in Chapter 3 of the thesis.

## *Chapter 3*

### THE AFFECT OF BORON OXIDE FLUX, $B_2O_3$ , ON GLASS FORMATION AND PROPERTIES

The breakthrough in understanding that underlies this chapter occurred while working on the Fe-based glass presented in Chapter 2. This chapter references that glass, and builds on the alloy development undertaken there. Two key incidents led to this chapter: the problems with the reproducibility of the Fe-based alloy, and from accidentally fluxing an alloy for 20 hours instead of 20 minutes, which dramatically increased its glass forming ability. Between these two factors, we were able to make the necessary discoveries to improve the understanding on fluxing. This chapter is largely taken from a paper, but has been edited to include more of the results and steps towards discovery.

#### **3.1 Abstract**

We identify a reduction reaction of boron oxide by Si during melt fluxing of the Fe-Co-Si-B-P system, which promotes an unexpected exchange of Si and B in the alloy, resulting a significant B enrichment and a significant Si depletion in the alloy. Taking this reaction into account, a unique optimization strategy is implemented enabling oxide purification of the melt along with a significant, but predictable shift in composition. This leads to an optimized Fe-Co-Si-B-P alloy free from oxide inclusions, and demonstrating a global peak in glass forming ability. This reaction also occurs, to various degrees, in other glass forming systems that contain

silicon, and no reduction reaction is seen when silicon is not present. Following a 22 hour boron oxide fluxing in the high temperature melt, alloy with composition  $\text{Fe}_{57.5}\text{Co}_{20.2}\text{Si}_{10.2}\text{B}_{2.05}\text{P}_{10.05}$  transforms to  $\text{Fe}_{57}\text{Co}_{19.2}\text{Si}_{6.8}\text{B}_{7.4}\text{P}_{9.6}$ , and its critical rod diameter increases from 1 mm to 5 mm, which is significantly higher than all neighboring compositions. The alloy also demonstrates excellent soft ferromagnetic performance characterized by a magnetic saturation of 1.53 T.

### 3.2 Introduction

Ferromagnetic metallic glasses have been of interest since their discovery in 1967 [2], due to their low coercivities and high magnetic permeabilities, arising from atomic homogeneity at length scales comparable to the magnetic correlation length [39]. These soft magnetic properties have led to their widespread use in automotive magnetics, magnetic sensors, power supplies, and power transformers [64]. Currently, commercially available ferromagnetic metallic glasses are produced via the rapid quench process of melt spinning, producing cooling rates ranging between  $10^4 - 10^6$  K/s. The requirement for such a high cooling rate limits the thickness of the quenched glassy part to micrometer-thick ribbons. To improve the glass forming ability and increase the critical process thickness of those early ferromagnetic glass formers, nonferrous metals such as Ga [46], Cr [65], Nb [55], Mo [56], and Zr [21] have been added to great effect. While being beneficial to the glass forming ability, it also comes at the expense of the magnetic saturation, as these non-ferrous metals tend to reduce the magnetic moment per atom of the alloy.

To bypass the limitations of adding nonferrous metals, alloy developers have turned to melt fluxing, a widely known purification technique for metal/metalloid glass formers. Specifically, boron oxide fluxing has been known to improve the glass forming ability of metallic glasses since 1984 [3]. Boron oxide fluxing has been reported to also improve the thermal [25], mechanical [9], and magnetic [46] properties of metallic glasses by removing oxide particles from the melt [73, 26]. This technique has been applied to ferromagnetic glass formers with good success [65, 46]. Oxide particles are generally entrained in the melt as inclusions. Such oxides are generally high melting point compounds that are chemically stable at melt processing temperatures typical for metallic glass forming alloys. They act as heterogeneous nucleation sites, catalyzing crystallization of the melt upon cooling, and thus limiting the glass forming ability [73]. In the presence of boron

oxide flux, the oxide inclusions are purged from the melt. The exact purging mechanism is not well understood, but it is thought to be driven by either a chemical reduction mechanism where the inclusion oxide reduces boron oxide to form a higher order oxide, or an equilibrium dissolution mechanism arising from an equilibrium solubility of the inclusion oxide in boron oxide.

In this study we found that in addition to oxide purification, boron oxide fluxing of a metallic glasses bearing Si gives rise to a chemical reaction by which the alloy becomes enriched in B and depleted in Si. We thoroughly studied a ferromagnetic-based glass bearing Si and B and lacking non-ferrous metals. We exploit this reduction reaction to implement a unique optimization approach by which the alloy is purified from oxide inclusions while also undergoing a large, but predictable shift in composition. With this approach, an optimum alloy composition may be identified, which in its purified (i.e. post-fluxed) form would demonstrate a global maximum in glass forming ability. This allowed us to increase the glass forming ability of the system introduced in Chapter 2. The new optimal composition transforms from a pre-flux composition of  $\text{Fe}_{57.5}\text{Co}_{20.2}\text{Si}_{10.2}\text{B}_{2.05}\text{P}_{10.05}$  to a post-flux composition of  $\text{Fe}_{57}\text{Co}_{19.2}\text{Si}_{6.8}\text{B}_{7.4}\text{P}_{9.6}$ .  $\text{Fe}_{57}\text{Co}_{19.2}\text{Si}_{6.8}\text{B}_{7.4}\text{P}_{9.6}$  has a critical rod diameter of 5 mm, and a magnetic saturation of 1.53 T.

### 3.3 Materials and Method

Metallic glass ingots were prepared by induction melting mixtures of the appropriate amounts of laboratory grade elements in sealed quartz tubes under an Ar atmospheres [67]. The ingots were fluxed with dehydrated boron oxide in a vertical tube furnace at 1350°C over various amounts of time, with the optimal fluxing time found to be 110 minutes. The molten alloy is then injected into a quartz tube, having a 0.5 mm thick wall using an argon back-pressure, where it is subsequently water quenched. This fluxing process occurred using small (5 mm) spheres of material surrounded by flux, in order to obtain a large surface area to volume ratio, and thus speeds up the kinetics of the reaction.

The alloy compositions were evaluated by secondary ion mass spectroscopy (SIMS), using oxygen ions to excite the surface and unfluxed specimens as reference [74, 75]. The amorphicity of the quenched rods was evaluated using X-ray diffraction (XRD) with Cu- $K\alpha$  radiation. Differential scanning calorimetry (DSC), at a heating rate of 20K/min, was used to determine the Curie temperature ( $T_c$ ), glass transition temperature ( $T_g$ ), crystallization temperature ( $T_x$ ), solidus temperature ( $T_s$ ), and liquidus temperature ( $T_l$ ). DSC was also used as a secondary means of identifying changes in composition by monitoring shifts in the liquidus. The Curie temperature was also evaluated using thermogravimetric analysis [76].

Magnetic testing was carried out in a similar fashion to the previous chapter, with the key difference being the geometry of the samples measured. In this instance the samples were 5 mm rods, that were electric discharge machined into toroids having outer diameters of 5.14 mm, inner diameters of 3.69 mm, and heights of 0.88 mm. The toroids were wrapped with a 30-AWG insulated copper wire producing 40 primary turns and 20 secondary turns. The magnetic properties were characterized using a Walker AMH-200k-S Hysteresisgraph at 50 Hz frequency and 25 kA/m magnetic flux.

### 3.4 Results

In this chapter, we investigate the effects of boron oxide fluxing on the Fe-Co-Si-B-P system. Selection of this system is motivated by an expectation that the lack of non-ferrous transition metals (such as Mo, Ni, Cr, Nb, etc.) would yield a high saturation magnetization, as non-magnetic transition metals tend to limit the saturation magnetization of bulk ferromagnetic glasses (typically around 1.1 T) [28]. Indeed, Li et al. [59] have demonstrated that a specific composition within this alloy system,  $\text{Fe}_{68.4}\text{Co}_{7.6}\text{Si}_9\text{B}_{10}\text{P}_5$ , is a bulk glass former with critical rod diameter of 3 mm and exhibits a saturation magnetization of 1.5 T. The objective of this work was to implement a careful compositional optimization process combined with a melt purification process that would allow us to maximize the critical rod diameter of the ferromagnetic alloy while retaining a high saturation magnetization.

Here, we implemented a "biased random walk" algorithm relying on a "steepest ascent approach", similar to that proposed by Na et al [27], to evaluate glass forming ability cusps in composition space. We performed this for fluxed and unfluxed alloys along the composition direction associated with variation of B at the expense of Si. The unfluxed alloys follow the composition formula  $\text{Fe}_{57}\text{Co}_{19.2}\text{Si}_{(14.2-x)}\text{B}_x\text{P}_{9.6}$ , while the fluxed alloys follow  $\text{Fe}_{57.5}\text{Co}_{20.2}\text{Si}_{(12.3-x)}\text{B}_x\text{P}_{10}$  (note that these composition formulas represent the as-weighed compositions prior to fluxing the alloys).

In Figure 3.1, we plot the critical rod diameter versus the atomic concentration of B for unfluxed and fluxed alloys. As seen in Figure 3.1, the GFA peak in the fluxed and unfluxed alloys appears at very different B/Si concentrations. Specifically, the peak in the unfluxed alloys appears at B and Si concentrations of 6.3% and 7.9% respectively, while that in the fluxed alloys occurs at B and Si concentrations of 2.1% and 10.2% respectively. As such, the optimum alloy in the unfluxed series is  $\text{Fe}_{57}\text{Co}_{19.2}\text{Si}_{7.9}\text{B}_{6.3}\text{P}_{9.6}$  demonstrating a critical rod diameter of 5 mm while that in the fluxed series is  $\text{Fe}_{57.5}\text{Co}_{20.2}\text{Si}_{10.2}\text{B}_{2.1}\text{P}_{10}$  and demonstrates a critical rod diameter

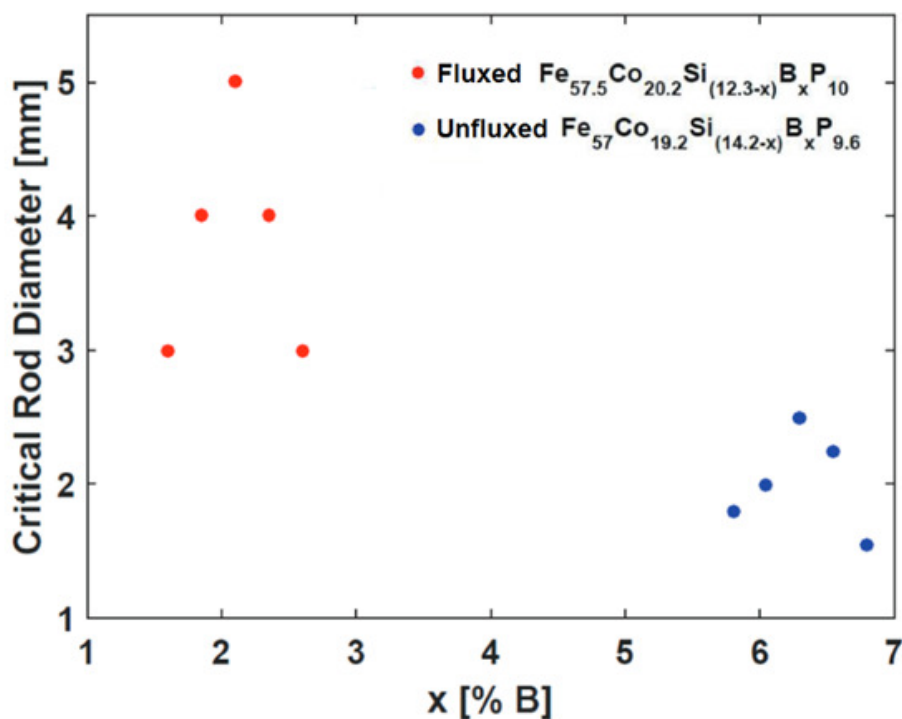


Figure 3.1: Dependence of the critical rod diameter of Fe-Co-Si-B-P alloys on the atomic concentration of B in the fluxed and unfluxed alloy with Si being substituted by B in the alloy. The unfluxed alloys follow  $\text{Fe}_{57}\text{Co}_{19.2}\text{Si}_{14.2-x}\text{B}_x\text{P}_{9.6}$  while the fluxed alloys follow  $\text{Fe}_{57.5}\text{Co}_{20.2}\text{Si}_{(12.3-x)}\text{B}_x\text{P}_{10}$ .

of 2.5 mm. Interestingly, the critical rod diameters of fluxed  $\text{Fe}_{57}\text{Co}_{19.2}\text{Si}_{7.9}\text{B}_{6.3}\text{P}_{9.6}$ , and unfluxed  $\text{Fe}_{57.5}\text{Co}_{20.2}\text{Si}_{10.2}\text{B}_{2.1}\text{P}_{10}$  are about 1 mm or less (not shown in Figure 2.2).

Through a very systematic compositional mapping, Na et al. demonstrated that unique cusps in GFA with each compositional coordinate where one element (or a group of elements) is substituted by another [27]. Here, we verified that the corresponding peaks for the fluxed and unfluxed alloys are indeed unique (i.e. the critical rod diameter is found to be essentially zero in unfluxed alloys at B and Si concentrations of 2.1% and 10.2%, and in fluxed alloys at B and Si concentrations of 6.3% and 7.9%). Here we find that this unusual compositional shift in the

GFA peak between fluxed and unfluxed alloys is attributed entirely to a chemical reaction occurring during fluxing, which contributes to significant shift in the alloy composition. Specifically, we find that the composition of the optimum alloy in the fluxed alloy series is not only purified after fluxing, but is also shifted to a composition that is roughly the composition of the optimum alloy in the unfluxed alloy series. That is, following fluxing, the two alloys at the GFA peaks in Figure 3.1 appear to have the same composition.

Using SIMS, the post-fluxed composition of the optimum alloy in the fluxed series,  $\text{Fe}_{57.5}\text{Co}_{20.2}\text{Si}_{10.2}\text{B}_{2.1}\text{P}_{10}$ , was evaluated to be  $\text{Fe}_{57}\text{Co}_{19.2}\text{Si}_{6.8}\text{B}_{7.4}\text{P}_{9.6}$ . The post fluxed composition is therefore very close to that of the optimum alloy in the unfluxed series,  $\text{Fe}_{57}\text{Co}_{19.2}\text{Si}_{6.8}\text{B}_{7.4}\text{P}_{9.6}$ . This suggests that the peak in glass forming ability in the B-Si composition vector is unique, consistent with Na et al [27]. Therefore, following fluxing, the composition of alloy  $\text{Fe}_{57.5}\text{Co}_{20.2}\text{Si}_{10.2}\text{B}_{2.1}\text{P}_{10}$  shifts to this “unique” optimum composition, and because the alloy is purified from oxide inclusions after being fluxed, the critical rod diameter of the alloy is twice as large as that of an unfluxed alloy having the same composition.

In Figure 3.2 we present a calorimetry scan at 20 K/min of the alloy having the peak GFA in the fluxed series,  $\text{Fe}_{57.5}\text{Co}_{20.2}\text{Si}_{10.2}\text{B}_{2.1}\text{P}_{10}$ , and the alloy having the peak in the unfluxed series,  $\text{Fe}_{57}\text{Co}_{19.2}\text{Si}_{6.8}\text{B}_{7.4}\text{P}_{9.6}$ . As seen, the glass-transition, crystallization, solidus and liquidus temperatures in the two alloys are very similar, thereby supporting the chemical exchange mechanism with the fluxing agent discussed above. The Curie temperature is also almost identical. Generally, for both alloys the scan reveals approximately a Curie temperature,  $T_c$ , of  $\sim 722\text{K}$ , a glass transition temperature,  $T_g$ , of  $\sim 772\text{K}$ , a crystallization temperature,  $T_x$ , of  $807\text{K}$ , a solidus temperature,  $T_s$ , of  $1254\text{K}$ , and a liquidus temperature,  $T_l$ , of  $1353\text{K}$ , identified by arrows in Figure 3.2. This gives a reduced glass transition temperature ( $T_{rg}$ ) of 0.57, close to the value Turnbull predicted for a good glass former, 0.6 [3]. The high  $T_c$  of  $722\text{K}$  for this alloy is very desirable, as it leads to less degradation of the

magnetic saturation at elevated temperatures.

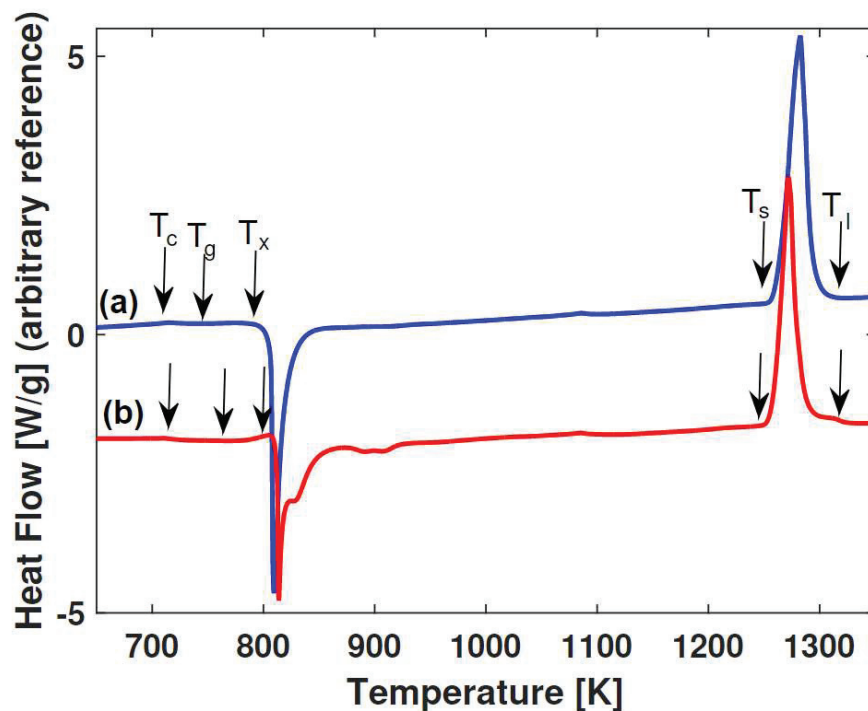


Figure 3.2: Calorimetry scans at 20 K/min of: (a) the alloy having the peak GFA in the fluxed series,  $\text{Fe}_{57.5}\text{Co}_{20.2}\text{Si}_{10.2}\text{B}_{2.1}\text{P}_{10}$ , and (b) the alloy having the peak in the unfluxed series,  $\text{Fe}_{57}\text{Co}_{19.2}\text{Si}_{6.8}\text{B}_{7.4}\text{P}_{9.6}$ . The  $T_c$ ,  $T_g$ ,  $T_x$ ,  $T_s$ , and  $T_l$  are identified by arrows.

To verify that a Si-B exchange indeed occurs during boron oxide melt fluxing, melt fluxing experiments were performed at  $1350^\circ\text{C}$  on alloy  $\text{Fe}_{57.5}\text{Co}_{20.2}\text{Si}_{10.2}\text{B}_{2.1}\text{P}_{10}$  (pre-fluxed composition). The fluxing experiments were performed at fixed time intervals, and the composition of the alloy at the end of each interval was evaluated with SIMS. The Si and B atomic concentrations in the alloy as a function of fluxing time are plotted in Figure 3.3. As seen in the plot, the concentration of Si decreases with increasing fluxing time from its initial concentration in the pre-fluxed alloy of 10.2 atomic percent to its post-fluxed concentration of 1.2 atomic percent following 21 hours of fluxing. On the other hand, the concentration of B increases from its initial pre-fluxed concentration of 2.1 to its post fluxed concentration of 7.6 atomic

percent following 22 hours of fluxing. The alloy composition after 22 hours of fluxing is  $\text{Fe}_{57.5}\text{Co}_{20.2}\text{Si}_{10.2}\text{B}_{2.1}\text{P}_{10}$ .

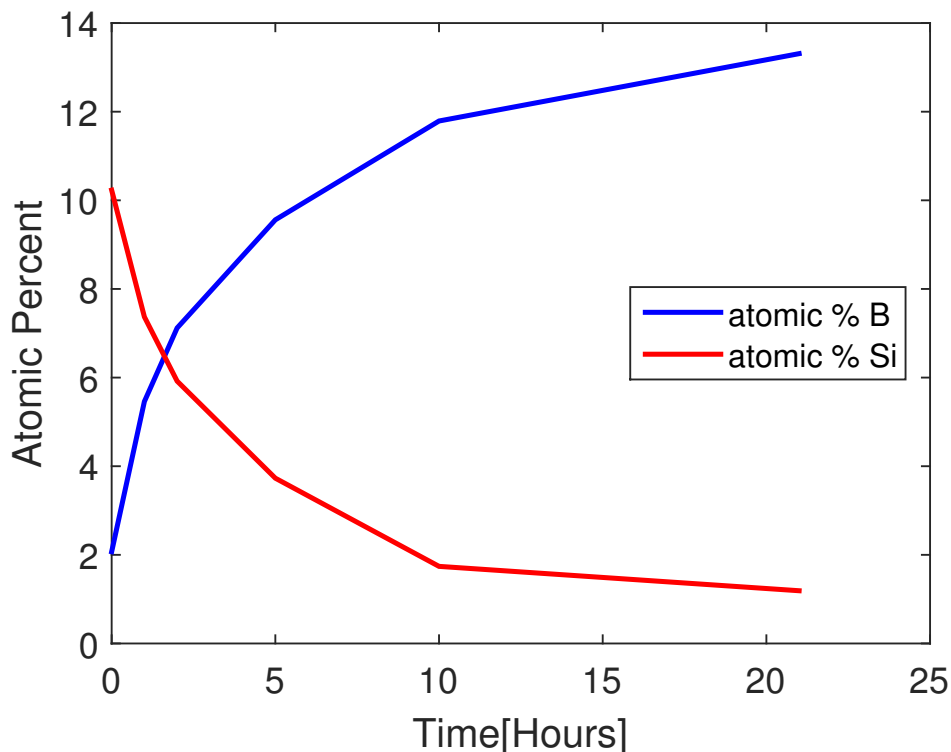


Figure 3.3: Change in boron and silicon in  $\text{Fe}_{57.5}\text{Co}_{20.2}\text{Si}_{10.2}\text{B}_{2.1}\text{P}_{10}$  as a function of fluxing time as measured by SIMS.

Such significant exchange between Si and B in the alloy cannot be explained simply by the removal of oxide inclusions from the alloy (e.g.  $\text{SiO}_2$  inclusions), as the volume fractions of such inclusions is understood to be rather small and hardly detectable [26]. Rather, such significant Si-B exchange is more likely caused by elemental depletion of Si and substitution by B through diffusion, driven by a chemical reaction in the boron oxide flux. Specifically, this exchange between B and Si should be driven primarily by the free energies of  $\text{Si} + \text{O}_2 \rightarrow \text{SiO}_2$  and  $\frac{4}{3}\text{B} + \text{O}_2(\text{g}) \rightarrow \frac{2}{3}\text{B}_2\text{O}_3$  reactions, as seen in Figure 3.4.

The Ellingham diagram for oxides [77]. In the diagram, the  $\text{SiO}_2$  line is slightly lower than the  $\text{B}_2\text{O}_3$  line, with a free energy difference of about  $30 \text{ kJ mol}^{-1}$

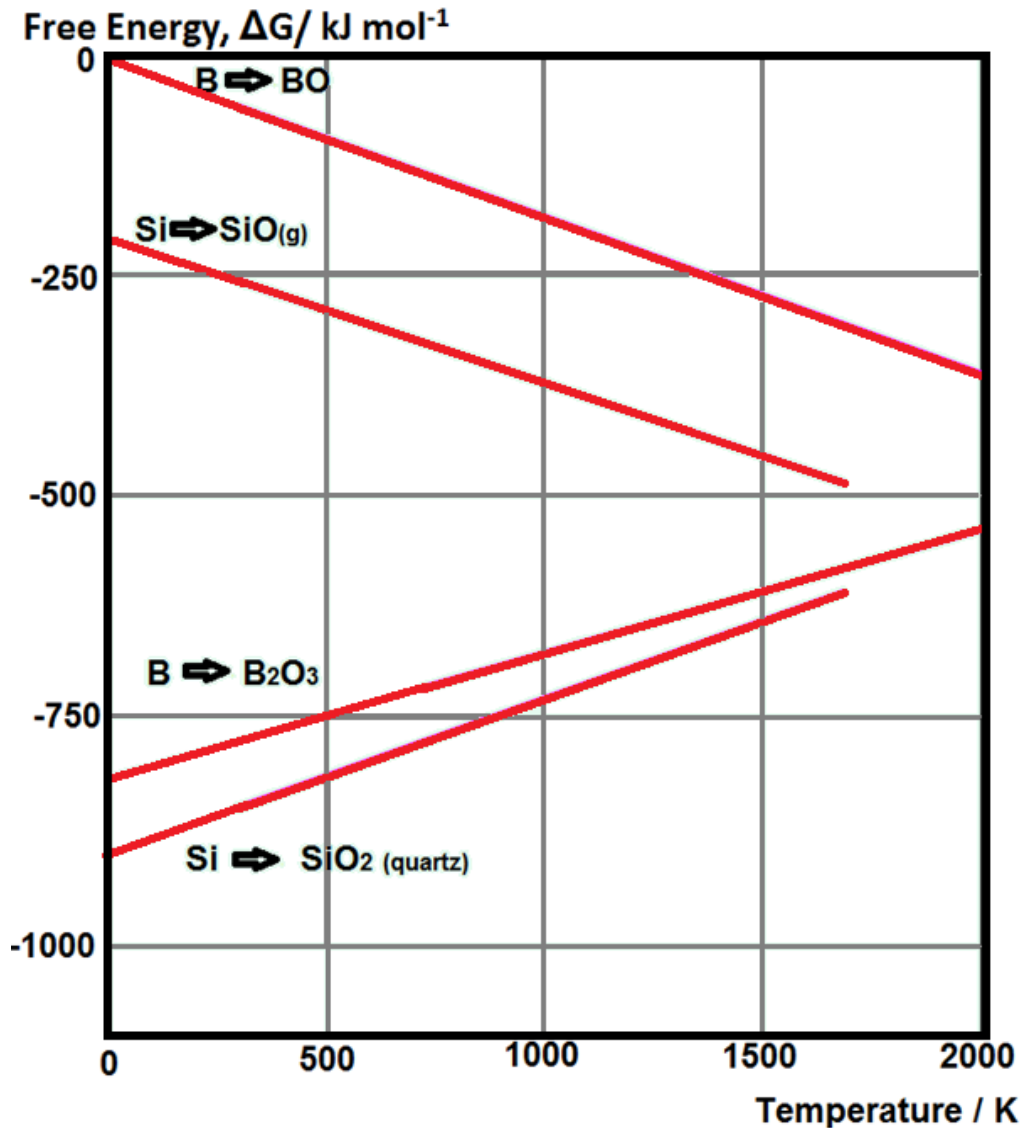
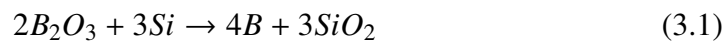


Figure 3.4: Ellingham diagram showing the free energy of boron, silicon, and their oxides over a broad range of temperatures [77].

at 1350K. This would drive the reaction:



This reaction can be seen occurring almost exactly as described by the B/Si concentration evolution plotted in Figure 3.3. The average ratio of B gained to Si lost in the alloy after 22 hours of fluxing, when the reaction is almost completed, is 1.18

(Figure 3.3). This is fairly close to the ratio of B lost to Si gained in the boron oxide flux when chemical equilibrium is established of 1.33, according to the reaction given by Equation 3.1.

This significant Si-B exchange during melt fluxing is also traceable by scanning calorimetry, as the increased B and decreased Si in the alloy contributes to a meaningful shift in the liquidus temperature of the alloy. In Figure 3.5 we present calorimetry scans for pre-fluxed composition  $\text{Fe}_{57.5}\text{Co}_{20.2}\text{Si}_{10.2}\text{B}_{2.1}\text{P}_{10}$  following the intermittent fluxing steps described above. The scans reveal that over short fluxing times (i.e. over the first hour of fluxing) the Si depletion and B enrichment cause the liquidus temperature of the alloy to drop, while having a negligible impact on the solidus temperature. This suggests that the increased B in alloy shifts the composition away from an intermetallic, possibly a silicide, and towards the eutectic composition. At longer fluxing times, the composition moves past this eutectic point, and towards a different intermetallic, possibly a boride. While part of the enhancement in glass forming ability is attributable to melt purification from oxide inclusions, a secondary part is the shift in composition which can drive the alloy composition towards a eutectic.

We investigated three other systems for which boron oxide melt fluxing has traditionally been used to purify the melt and improve the glass forming ability. The pre-fluxed compositions evaluated include:  $\text{Fe}_{68}\text{Mo}_4\text{Ni}_3\text{Co}_5\text{Si}_1\text{B}_{2.5}\text{P}_{11.5}\text{C}_5$ , whose critical rod diameter is found to increase from 2 to 12 mm with fluxing,  $\text{Pd}_{77.5}\text{Cu}_6\text{Si}_{16.5}$ , whose critical rod diameter increases from 3 to 15 mm [26], and  $\text{Pd}_{42.5}\text{Cu}_{30}\text{Ni}_{7.5}\text{P}_{20}$ , whose critical rod diameter increases from 40 [78] to 72 mm [25]. To assess the Si-B exchange during fluxing of these systems, the alloys were fluxed with boron oxide in the melt state at  $1350^\circ\text{C}$  for 22 hours in a manner similar to the Fe-Co-Si-B-P system, and their post-fluxing compositions were also evaluated using SIMS. Table 3.1 shows the compositions of these alloys before and after boron oxide fluxing, along with the change in critical rod diameter. As seen

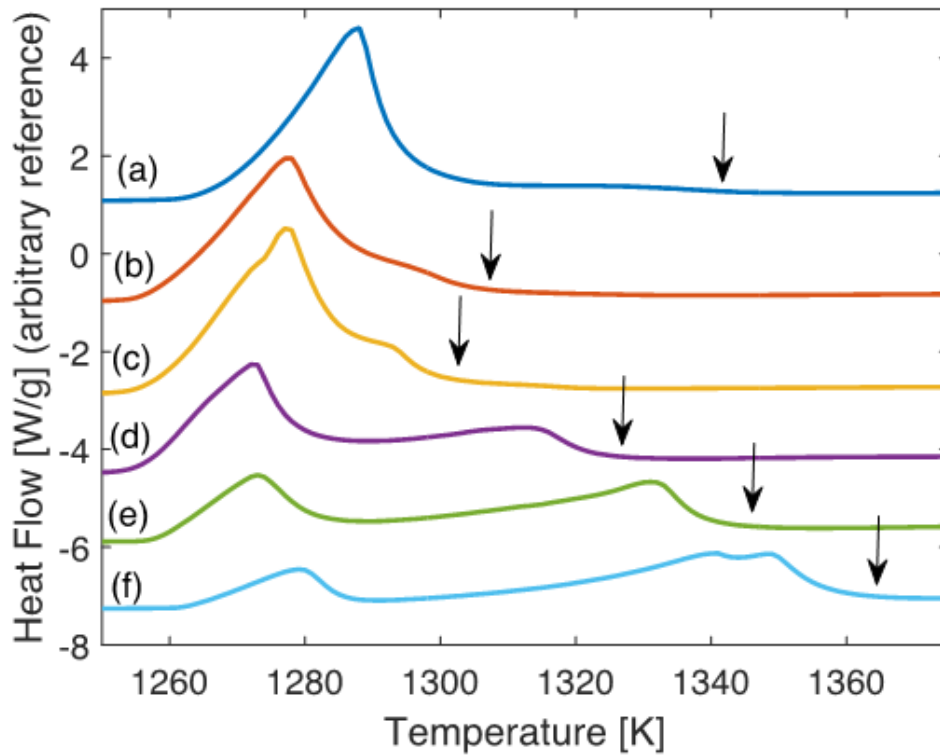


Figure 3.5: Calorimetry scans around the melting temperature of various fluxing states of alloy  $\text{Fe}_{57}\text{Co}_{19.2}\text{Si}_{6.8}\text{B}_{7.4}\text{P}_{9.6}$ : (a) no fluxing, (b) 1 hour fluxing, (c) 2 hours fluxing, (d) 5 hours fluxing, (e) 10 hours fluxing, and (f) 21 hours fluxing. The arrows designate the liquidus temperatures.

in Table 3.1, in  $\text{Fe}_{68}\text{Mo}_4\text{Ni}_3\text{Co}_5\text{Si}_1\text{B}_{2.5}\text{P}_{11.5}\text{C}_5$  the B concentration increases from 2.5 atomic percent to 2.95 while the Si concentration decreases from 1 to just 0.18 atomic percent. In  $\text{Pd}_{77.5}\text{Cu}_6\text{Si}_{16.5}$ , the B concentration increases from trace level (i.e. from the incidental impurity level of about 50 ppm [26]) to about 1.6 atomic percent, while the Si concentration decreases from 16.5 to 15.6 atomic percent. In  $\text{Pd}_{42.5}\text{Cu}_{30}\text{Ni}_{7.5}\text{P}_{20}$ , which is free of both Si and B, no enrichment of B or depletion of Si is observed after fluxing, as the concentration for both remained at the trace level.

These results suggest that in the complete absence of Si in the alloy (beyond trace level), as in  $\text{Pd}_{42.5}\text{Cu}_{30}\text{Ni}_{7.5}\text{P}_{20}$ , no detectable B dissolution takes place follow-

Composition		Critical Rod Diameter(mm)	Boron (at.%)	Silicon (at.%)
Fe <sub>57.5</sub> Co <sub>20.2</sub> Si <sub>10.2</sub> B <sub>2.1</sub> P <sub>10</sub>	unfluxed	0.5	2.05	10.2
	fluxed	5	7.4	6.85
Pd <sub>77.5</sub> Cu <sub>6</sub> Si <sub>16.5</sub>	unfluxed	3[26]	0.005	16.5
	fluxed	15[26]	1.594	15.615
Fe <sub>68</sub> Mo <sub>4</sub> Ni <sub>3</sub> Co <sub>5</sub> Si <sub>1</sub> B <sub>2.5</sub> P <sub>11.5</sub> C <sub>5</sub>	unfluxed	3[79]	2.5	1
	fluxed	12	2.95	0.18
Pd <sub>42.5</sub> Cu <sub>30</sub> Ni <sub>7.5</sub> P <sub>20</sub>	unfluxed	40[78]	0.005	0.005
	fluxed	72[25]	0.003	0.001

Table 3.1: Change in critical rod diameter, and concentrations of B and Si due to fluxing in Pd-based and Fe-based metallic glasses. All alloys were fluxed under the same conditions, and changes in composition were measured by SIMS.

ing boron oxide fluxing. However, when Si is nominally present in the alloys even in small concentrations, as in Fe<sub>68</sub>Mo<sub>4</sub>Ni<sub>3</sub>Co<sub>5</sub>Si<sub>1</sub>B<sub>2.5</sub>P<sub>11.5</sub>C<sub>5</sub>, detectable B enrichment and Si depletion occurs during boron oxide fluxing. The ratio of B gained to Si lost following fluxing in the Si-bearing alloys investigated here is not too close to the 1.33 value suggested by the equilibrium chemical reaction of Equation 3.1. In Fe<sub>57.5</sub>Co<sub>20.2</sub>Si<sub>10.2</sub>B<sub>2.1</sub>P<sub>10</sub> this ratio is 1.62, in Fe<sub>68</sub>Mo<sub>4</sub>Ni<sub>3</sub>Co<sub>5</sub>Si<sub>1</sub>B<sub>2.5</sub>P<sub>11.5</sub>C<sub>5</sub> the ratio is 0.55, while in Pd<sub>77.5</sub>Cu<sub>6</sub>Si<sub>16.5</sub> the ratio is 1.78. These values are close enough to still support the reaction of Equation 3.1 taking place, but suggest perhaps an incomplete reaction failing to attain equilibrium, or the incomplete dissolution of SiO<sub>2</sub> into the flux. Interestingly, the higher the Si content of the alloy, the higher the B gained to Si lost ratio following fluxing. However, despite the comparable B gained to Si lost ratio in all alloys, the total Si-B exchange in Fe<sub>57.5</sub>Co<sub>20.2</sub>Si<sub>10.2</sub>B<sub>2.05</sub>P<sub>10.05</sub> is significantly higher than in Fe<sub>68</sub>Mo<sub>4</sub>Ni<sub>3</sub>Co<sub>5</sub>Si<sub>1</sub>B<sub>2.5</sub>P<sub>11.5</sub>C<sub>5</sub> and Pd<sub>77.5</sub>Cu<sub>6</sub>Si<sub>16.5</sub>. Specifically, the B gained in Fe<sub>57.5</sub>Co<sub>20.2</sub>Si<sub>10.2</sub>B<sub>2.1</sub>P<sub>10</sub> is 4.2 at.%, compared to 1.6 at.% in Pd<sub>77.5</sub>Cu<sub>6</sub>Si<sub>16.5</sub>, and 0.45 at.% in Fe<sub>68</sub>Mo<sub>4</sub>Ni<sub>3</sub>Co<sub>5</sub>Si<sub>1</sub>B<sub>2.5</sub>P<sub>11.5</sub>C<sub>5</sub>. The reason for this is not quite clear from this study, but may be explained by a liquid miscibility gap in Fe<sub>68</sub>Mo<sub>4</sub>Ni<sub>3</sub>Co<sub>5</sub>Si<sub>1</sub>B<sub>2.5</sub>P<sub>11.5</sub>C<sub>5</sub> and Pd<sub>77.5</sub>Cu<sub>6</sub>Si<sub>16.5</sub>. Liquid

miscibility gaps are not unusual in metal/metalloid systems, and could potentially limit the amount of B soluble in the liquid state of these alloys (and consequently limit the amount of Si lost to complete the reaction of Equation 3.1). Nevertheless, the large amount of Si-B exchange following boron oxide fluxing observed in the Fe-Co-Si-B-P system is quite interesting, as it leads to an alloy with interesting properties.

### 3.5 Conclusion

In conclusion, we identified an exchange of Si for B occurring during boron oxide fluxing of the Fe-Co-Si-B-P system, where a significant enrichment of B in the alloy is accompanied by a significant depletion of Si. The ratio of B gained to the Si lost is roughly consistent with the reaction  $2B_2O_3 + 3Si \rightarrow 4B + 3SiO_2$ , suggesting that  $B_2O_3$  is reduced by Si extracted from the alloy to form  $SiO_2$ , resulting in the addition of B to the alloy. Other Si-bearing metal/metalloid glass forming alloys are also investigated here, and are also found to undergo such B-Si exchange, however the amounts of B gained and Si lost are significantly smaller than in the Fe-Co-Si-B-P system. Such significant Si-B exchange is utilized here in a unique optimization strategy to purify the melt while simultaneously accounting for the compositional shift thereby optimizing the Fe-Co-Si-B-P system for glass forming ability. An alloy, demonstrating a global maximum in glass forming ability is found, having a pre-fluxed composition  $Fe_{57.5}Co_{20.2}Si_{10.2}B_{2.1}P_{10}$ , with a glass forming ability of 0.5 mm, and post-fluxed composition  $Fe_{57}Co_{19.2}Si_{6.8}B_{7.4}P_{9.6}$ , with a glass forming ability of 5 mm.

*Chapter 4***PROCESSING AND MACHINING OF CORES FOR MAGNETIC TESTING**

This chapter is mostly a methods section for Chapter 5. It overviews the preparation and measurement techniques used on two separate alloys:  $\text{Fe}_{57}\text{Co}_{19.2}\text{Si}_{6.8}\text{B}_{7.4}\text{P}_{9.6}$  and  $\text{Fe}_{68}\text{Mo}_4\text{Ni}_3\text{Co}_5\text{Si}_1\text{B}_{2.5}\text{P}_{11.5}\text{C}_5$  [79]<sup>1</sup>. To test the magnetic properties of both, a toroidal sample was needed as described by Schwartz [46]. At the beginning of the project, no alloy from either alloy system could be produced with an adequate critical rod diameter to make a rod for testing. This led to extensive work with injection molding, which was ultimately abandoned due to reasons cited in this chapter. This chapter progresses in the same process order as a given sample would in order to produce a final core. Due to the variety of test conditions, not all annealing stages were carried out for every sample, but the machining and production stages are the same throughout

---

<sup>1</sup>Neither of these alloy systems were used at the beginning of the project, but were used exclusively after the fluxing knowledge from Chapter 3 was gained.

## 4.1 Injection Molding

Injection molding is a standard method for manufacturing metals and plastics. During injection molding, the material is first heated to the desired viscosity, before an applied pressure, whether it be mechanical, magnetic, or gas, pushes the material into a mold where it solidifies into its cast shape<sup>2</sup>. Injection molding has been used with varying success for the casting of metallic glass parts [80, 81]. Many metallic glass companies have begun to rapidly heat the metallic glass to its super-cooled liquid region before casting [82]. Unfortunately, we were limited to casting a molten alloy ( $T > T_l$ ) directly into a mold, due to the small  $\Delta T$ <sup>3</sup> for most Fe-based glasses, we could not process the metal in the super cooled liquid regime. We did this with the full knowledge of the problems associated with injection molding metallic glasses from the liquid state. Casting of amorphous discs was performed using custom “gas-pressure injection casting” equipment available in our lab, as shown in Figure 4.1.

This process involves inductively melting the alloy ingot in a nozzled quartz tube under an argon atmosphere. After a high temperature homogeneous melt is achieved, as measured by a pyrometer, application of an argon back-pressure injects the molten alloy into a copper mold having a desired cavity shape, see Figure 4.2. Here, you can see a well at the top of the mold, followed by the gate and mold cavity, and a vent on the bottom of the mold. The well is designed for the nozzled quartz tube to fit tightly inside of it, forcing the material into the mold, and keeping the high pressure. The vent is on the opposite side of the gate and is there to let any trapped air be released from the mold, thus enabling less porosity. The gate is designed to control the flow of the molten metal into the mold, allowing for the molten front to coalesce and removing excess gas bubbles.

---

<sup>2</sup>Depending on the material, method, and mold, the as-cast shape may not be the final geometry.

<sup>3</sup> $\Delta T$  is the difference between  $T_g$  and  $T_x$ . It is a major factor controlling the amount of time a metallic glass can spend in the super-cooled liquid region before crystallizing.

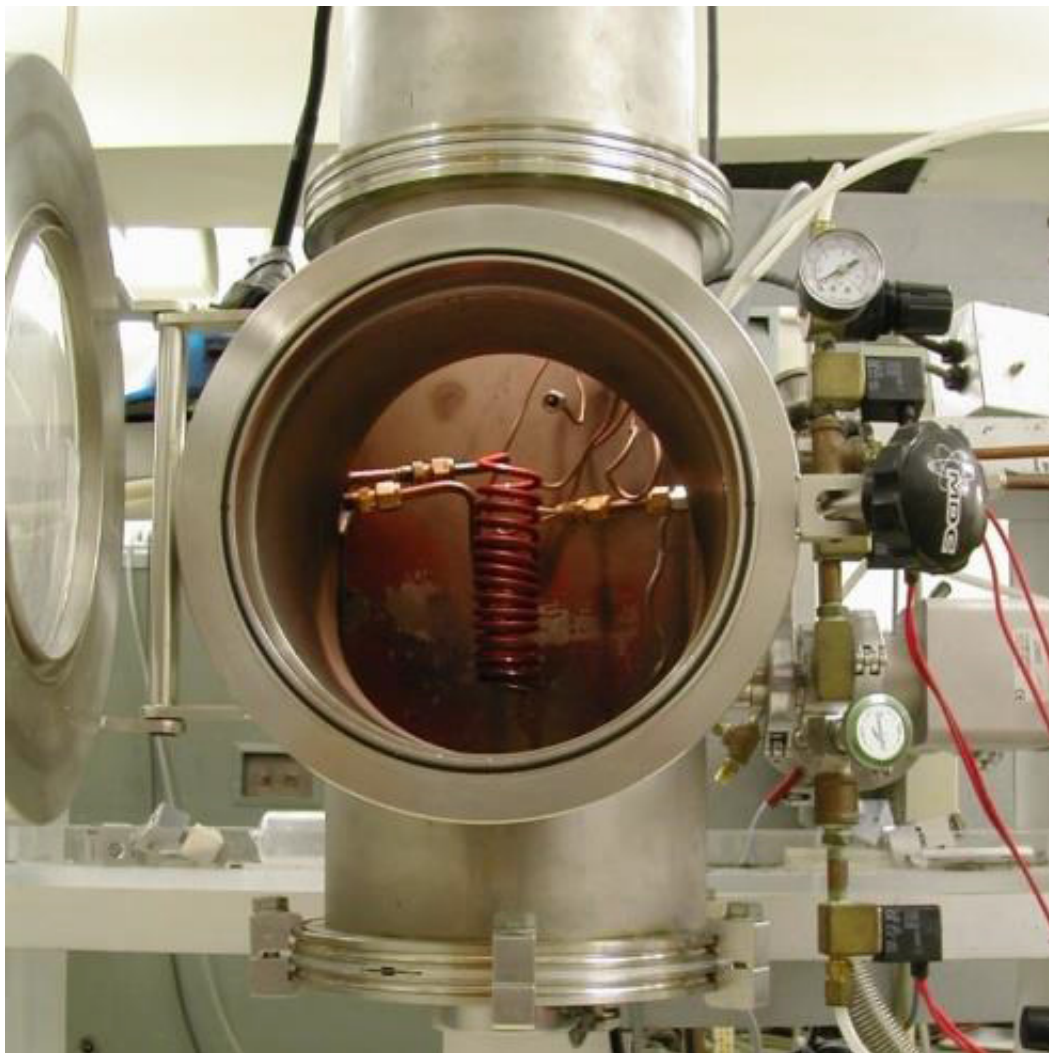


Figure 4.1: Casting box used to injection mold Fe-based samples into disc and toroidal geometries. Samples are heated by an inductive coil, while the temperature is measured by a pyrometer.

Initially we had a toroidal cavity for the molten alloy to be injected into, but this was changed to the disc shaped cavity seen in Figure 4.2. The reason for the change in shape is that we were unable to successfully cast a toroid without crystallizing the sample. If the sample was too cool, the metal would vitrify before fully forming the ring, but if it was too hot, then the flow front would break apart and the sample would cool too slowly to become a glass. This same balance of temperatures and viscosities also had to be dealt with for the disc, but the simpler geometry allowed for a wider temperature range, which could form amorphous



Figure 4.2: Copper mold used to injection mold ferromagnetic metallic glass disks.

parts. A 12-mm diameter 1-mm thick disk of a cast bulk ferromagnetic glass  $\text{Fe}_{68}\text{Mo}_4\text{Ni}_3\text{Co}_5\text{Si}_1\text{B}_{2.5}\text{P}_{11.5}\text{C}_5$  is shown in Figure 4.3.

Once the sample is cast into the mold, it must be machined into its final geometry. The gate and vent sections are cut off, while the surface flow features are polished away. While being successful, injection mold casting was no longer used once the advances in fluxing were made in Chapter 3. With the advanced fluxing procedure, we were able to cast up to 5 mm rods of  $\text{Fe}_{57}\text{Co}_{19.2}\text{Si}_{6.8}\text{B}_{7.4}\text{P}_{9.6}$  and up to 12 mm rods of  $\text{Fe}_{68}\text{Mo}_4\text{Ni}_3\text{Co}_5\text{Si}_1\text{B}_{2.5}\text{P}_{11.5}\text{C}_5$ . With this capability we settled on an external diameter of 4-5 mm for all of our tests, and stopped injection molding. The casting of rods enabled us to make tens of discs at once, instead of injection molding one sample at a time, with the only additional step for the rods being the cutting/polishing of the rod into discs of equal size. The samples are polished to ensure that all the samples have a uniform sample roughness, allowing for a better comparison of the total losses between samples since the anomalous losses are related to the surface roughness<sup>4</sup>.

<sup>4</sup>Polishing also cuts down the losses in the core, since surface roughness can act as pinning sites for the domain walls.



Figure 4.3: Injection cast metallic glass disc of  $\text{Fe}_{68}\text{Mo}_4\text{Ni}_3\text{Co}_5\text{Si}_1\text{B}_{2.5}\text{P}_{11.5}\text{C}_5$ . This sample will then be machined into a toroidal core.

## 4.2 Stress Annealing

An additional step that was added to ensure the uniformity of the discs. The cut and polished discs are stress-annealed to remove any internal stresses<sup>5</sup>. This is important for two reasons: to improve the magnetic and mechanical properties of each alloy. Neither material is a zero-magnetostriction alloy, which increases the losses of a sample when the compressive stresses in the material interact with the applied magnetic field. The stresses create an opposing magnetic field, with the strength of the field given by:

$$H_{\sigma} = \frac{3}{2} \frac{\sigma}{\mu_0} \left( \frac{d\lambda}{dM} \right)_T \quad (4.1)$$

where  $\sigma$  is the local internal stress,  $\mu_0$  is the permeability of free space, and  $\left( \frac{d\lambda}{dM} \right)_T$  is the change in magnetostriction with the magnetization of the material. By removing the quenched-in stresses from the material, the the magnetostrictive effect on the losses can be negated. The mechanical properties of both  $\text{Fe}_{68}\text{Mo}_4\text{Ni}_3\text{Co}_5\text{Si}_1\text{B}_{2.5}\text{P}_{11.5}\text{C}_5$  and  $\text{Fe}_{57}\text{Co}_{19.2}\text{Si}_{6.8}\text{B}_{7.4}\text{P}_{9.6}$  are also improved by removing the quenched-in stresses. The uneven quenched-in stresses act as stress concentrators for other applied stresses, lowering the already poor fracture toughness of the sample<sup>6</sup>[11, 65, 28, 83].

When we injection cast the molten alloy into the mold, the alloy is quenched from  $\sim 1250^\circ\text{C}$  to room temperature. This does not occur uniformly, but is instead anisotropic, cooling from the base of the mold to the top, or from the vent to the gate. In addition to this, the disc shape also causes cooling from the edges of the mold to the center<sup>7</sup>. Both of these factors cause large amounts of stresses in the injection

---

<sup>5</sup>This was later moved to before section cutting the rods to reduce the amount of surface oxidation which occurred.

<sup>6</sup>The fracture toughness of Fe-based alloys have historically been low, as compared to other metallic glasses, due to the theoretically weak bonds formed by iron in the glass.

<sup>7</sup>This assumes that the flow front was uniform, and did not break up.

molded disc, and led to a large number of failures even when a fully amorphous disc was cast. Likewise, there are large internal stresses in the rods caused by its fast cooling rate, although these stresses are much lower than those in injection molded discs.

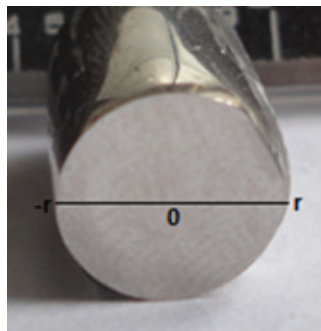


Figure 4.4: Cross section of an 11 mm cast rod of  $\text{Fe}_{68}\text{Mo}_4\text{Ni}_3\text{Co}_5\text{Si}_1\text{B}_{2.5}\text{P}_{11.5}\text{C}_5$ . This rod was cast in a quartz tube and quenched in water.

To determine the stress profile of a rod, we will look at the cooling across a cross-section. Figure 4.4 shows the cross-section of an 11 mm rod of  $\text{Fe}_{68}\text{Mo}_4\text{Ni}_3\text{Co}_5\text{Si}_1\text{B}_{2.5}\text{P}_{11.5}\text{C}_5$ , with the center of the rod being 0 and either edge having a distance of  $r$  away. This rod was cast in a quartz tube before being water quenched, enabling the fast cooling rates necessary to vitrify the melt. Unfortunately, these fast cooling rates also cause large residual stresses in the rod. The exterior is in compression since it cools first and then as the interior cools, it is pulled in and put in compression. Likewise, the interior cools last, and is pulled out to try to fill the void left by it shrinking during cooling putting it in tension [84]. A diagram of the cooling history of the rod can be seen in Figure 4.5, with the cross section being the same as in Figure 4.4. Here we progress in time with each curve, with  $t_0$  being the time before any cooling has occurred and  $t_4$  being a fully quenched sample. At time  $t_0$ , the sample has yet to be quenched and is sitting at an equilibrium temperature inside the furnace. At  $t_1$ , the sample has just been quenched, with the exterior of the rod solidifying as it cools below the glass transition temperature, and the interior of the rod remaining at the initial temperature. At  $t_2$  and  $t_3$ , the rod continues to

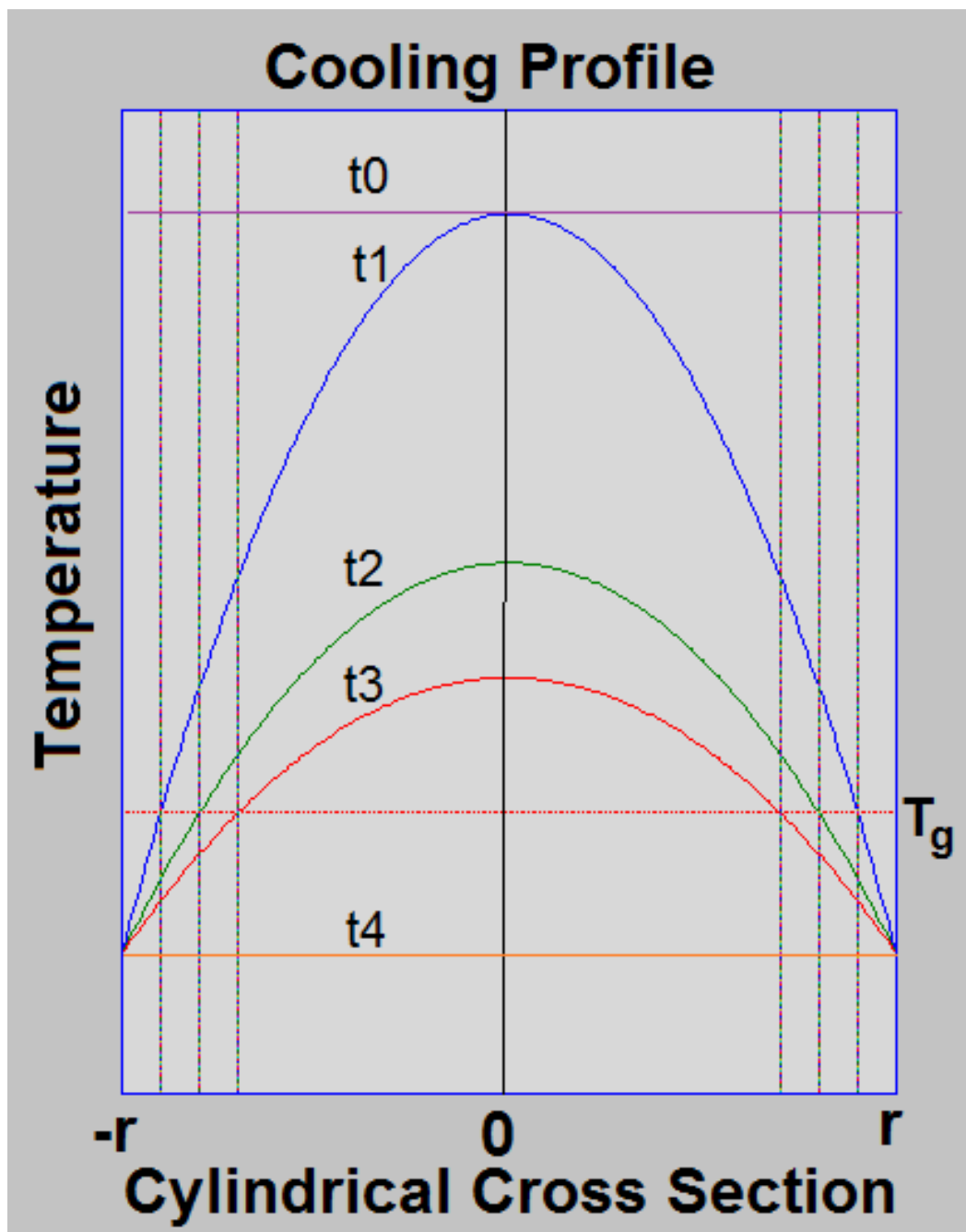


Figure 4.5: Cooling profile of a the cross section of a cylindrical rod. At time 0, the sample has et to be cooled and the temperature is constant across the rod. At time 1, the sample has been quenched and the exterior of the rod has dropped below  $T_g$  and solidified, but the interior of the rod is still molten. At time 2 and 3, the rod is still cooling, with the rod solidifying from the outside. At time 4, the rod has cooled to room temperature and is now completely solid.

cool radially, with solidification gradually progressing inwards, and the centerline temperature dropping. At  $t_4$ , the rod is fully quenched and is sitting at room temperature, and the rod has all the stresses associated with its cooling history. Cooling thicker rods, or quenching at faster rates both increase the stresses associated with cooling. Luckily the thermal expansion coefficient of the glass is quite low [85], minimizing these stresses as compared to crystalline alloys.

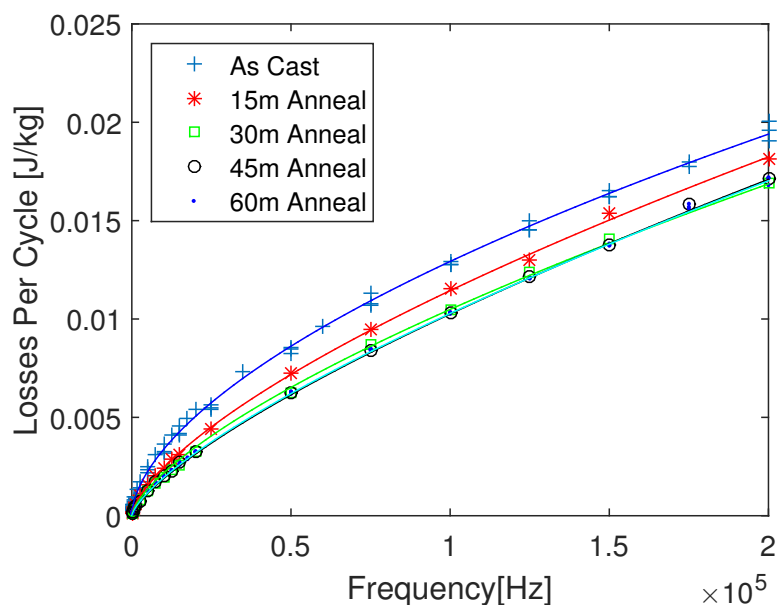


Figure 4.6: Loss curves for  $e_{68}Mo_4Ni_3Co_5Si_1B_{2.5}P_{11.5}C_5$  on a plot of total losses per kg per cycle versus the frequency. As the stress annealing time increases, the losses decrease until they reach a plateau at a stress anneal time of 30 minutes. Similar effects are seen for  $Fe_{57}Co_{19.2}Si_{6.8}B_{7.4}P_{9.6}$ .

To remove the quenched-in stresses, we adopted a stress annealing process that is a modified version of the one presented by Schwarz [46]. We followed the procedure of annealing at  $T = T_g - 60K$  that they presented, but found our optimal stress annealing time to be 45 minutes. Figure 4.6 shows what we will term a loss curve, consisting of multiple loss curves on a plot of the total losses per kg per cycle versus the frequency. This will be our standard for measurement of the efficiency for a transformer core throughout this thesis, and is one of several

standard measurements for the efficiency of a material [46, 47, 86, 87, 88]<sup>8</sup>. Stress annealing removes the quenched-in stresses in the toroidal core, these stresses affect the magnetostriction, as we described before, and the domain walls. The gradient in the stresses act as pinning sites, or defects, in the material to hamper the movement of the domain walls. As we increase the stress annealing time, the losses in our core continue to decrease until we reach an annealing time of 30 minutes, where the losses plateau. This plateau in losses should occur when the stresses in the core have been reduced to zero, but this is only a theory for our material since we did not directly measure the stresses.

The removal of stresses in the material also impacts the permeability of the material, as seen in Figure 4.7. Figure 4.7 shows the change in the permeability between an as-cast sample and a stress annealed sample. The lack of stresses in the core removes the opposing magnetic field created by magnetostriction. This in turn allows the core to see a higher magnetic field for a given applied field, thus increasing the magnetization at that field and the permeability of the material. All of this accounts for the large increase in the permeability of the core.

---

<sup>8</sup>Section 4.4 describes in detail how these curves are made.

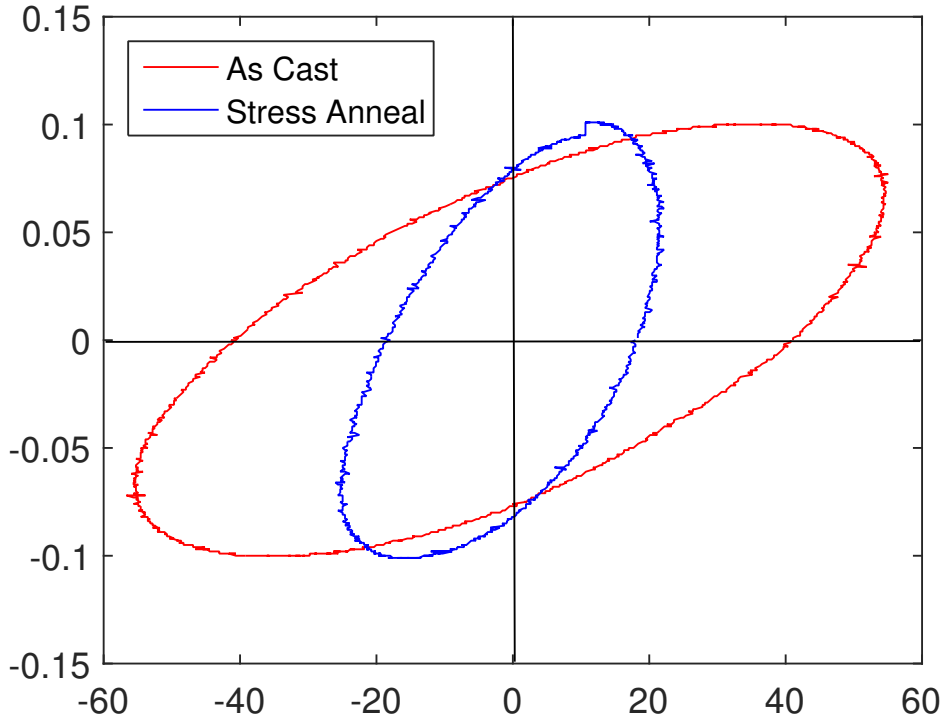


Figure 4.7: Impact of stress annealing for 45 minutes at 60K below  $T_g$  on the permeability and losses of a toroidal core of  $Fe_{68}Mo_4Ni_3Co_5Si_1B_{2.5}P_{11.5}C_5$ . Similar effects are seen for  $Fe_{57}Co_{19.2}Si_{6.8}B_{7.4}P_{9.6}$ .

### 4.3 Electric Discharge Machining

Once the samples were cast, stress-annealed, cut, and polished, we sent them out for electrical discharge machining (EDM). While the lack of an EDM on campus did increase the expense of the project, and delay any testing done, it was a necessary step due to the lack of availability of an ulterior machining method. The constraints on the machining process were threefold: low mechanical stress, low heat, and a process with tight tolerances. With this in mind we explored several other machining methods before settling on EDM. The first method examined utilized a drill press to create the center hole, but the mechanical forces exerted would be too large for our materials. The second possible method was water jet cutting, but this method does not have the tolerances required, and also has issues with mechanical forces. The third potential method was laser beam machining, while this meets the first and third criteria, it was discounted due to the heat generated in the process<sup>9</sup>. This led us to go with EDM, since it generated no mechanical forces, could cut exact cuts, and had a very small, a few microns thick, heat affected zone. The die-sink EDM process was used due to its ease of use, and no center hole needing to be pre-drilled.

After several iterations of power settings, and holders, see Figure 4.8(a) and 4.8(b), we found a holder that allowed us to cut samples on the edge of what is possible for EDM. Figure 4.8(a) is the first generation of holder for a 4 mm sample, with the notch in the ring enabling a cut sample to be extracted. This holder was abandoned since it did not enable concentric center holes to be cut, and samples would break upon extraction. This turned into the base for the final holder, with Figure 4.8(b) being the top of the final holder. There are two graphite toroids, one of which the sample sat on, and the other sitting on top of the sample. This allowed for concentric holes, and removed all forces from the extraction stage. Figure 4.8(c) shows a toroidal core with a uniform wall thickness of 250 microns. With this

---

<sup>9</sup>We later found another research group that had solved the heat issues of laser beam cutting by using the FB750 laser cutting machine from CadCam Technology.



Figure 4.8: EDM holder and cut core. (a) The steel base of the final iteration of holder and the entirety of the first iteration. (b) The graphite top of the final iteration on the sample holder. (c) A cut toroidal core with a wall thickness of 250 microns.

method, we were able to machine cores with a minimum wall thickness of 100 microns.

#### 4.4 Magnetic Measurements

As we saw in Figure 2.7, through the use of the Walker AMH-200k-S Hysteresisgraph we can assemble hysteresis loops for a given sample. Each hysteresis loop is created by winding a core, as seen in Figure 4.9, and has a given material, geometry, annealed status, temperature, frequency, and max magnetization. To create a curve, like those in Figure 2.8, or Figure 4.6, we assemble a series of hysteresis curves while only allowing one variable to change. We decided to keep one variable, the temperature, constant across all tests. We did so based on our knowledge from the Curie Curve, that as the temperature of the material increases its ferromagnetic properties decrease[45]. That forced us to negate the resistive heating in the wires wound around the core by keeping the core in a water bath. Unlike the hysteresis curve in Figure 2.7, we also limit the max magnetization to a nominal value, as seen in Figure 4.7. This is the standard procedure in the literature for measuring the losses in an alloy, due to the differing saturation magnetization of different alloys, and the impact of the test magnetization on the total losses, as seen in Equation 1.9.

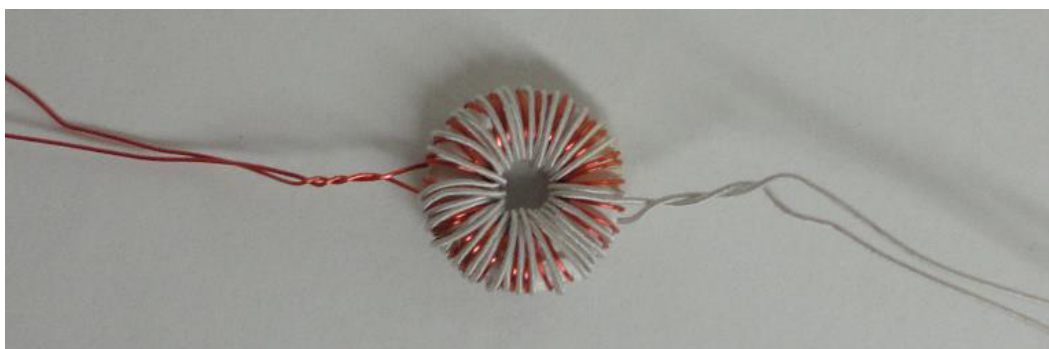


Figure 4.9: Wound toroidal core.

Once we have decided which variable that will be fluctuating, then we can assemble our total loss curve. This normally results in the frequency being allowed to vary, with the thickness of the core being a close second. To get a loss curve,

like the ones seen in Figure 4.6, we first must make individual hysteresis curves. By measuring the same core across a wide range of frequencies, we can then create a losses per kg versus frequency curve, as seen in Figure 4.10.

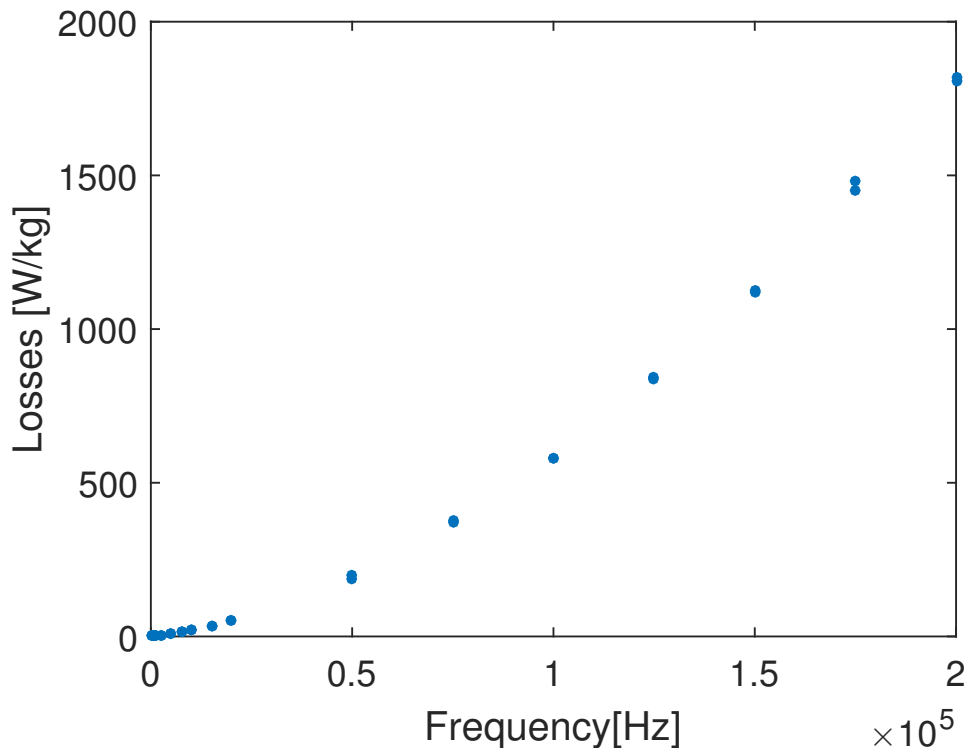


Figure 4.10: Total losses per kg versus frequency. This is the raw data assembled from the hysteresisgraph with each data point being a hysteresis curve.

Each data point in Figure 4.10 is the raw loss data outputted from the hysteresisgraph, with each of them representing the losses from a hysteresis curve for a given material, geometry, and annealing state. Here, we have plotted two data points for any given frequency, but we varied the number of test points for any given frequency to up to 7<sup>10</sup>. Once this raw data was generated, then we divide each data point by its frequency to get the losses per cycle ( $W_t$ ). We then fit this data with a 2<sup>nd</sup>-order power law generated by the curve fitting tool in Matlab and having a

<sup>10</sup>We saw very little fluctuation in the data points across our samples. In some test configurations our standard deviation did increase, and in those cases we took more data points. Unfortunately each test was quite time consuming and the number of tests which needed to be run prohibited more statistically accurate sample sizes.

general form of:

$$y = a * x^b + c \quad (4.2)$$

As seen in Figure 4.11, this allowed us to predict the losses per cycle for any given frequency, and also to find the hysteresis losses for the sample by finding the y-intercept of our fit. The blue data points are the same data points from Figure 4.10, but divided by the frequency they are measured at. The red curve is the power law fit of the losses per cycle versus frequency, and the black line is the hysteresis losses which are independent of frequency. The power law fit corresponds quite well to the losses data, giving a R-squared value greater than 0.99 for all of the losses versus frequency curves that we assembled. Unfortunately we cannot plot the theoretical eddy current loss equation set out in Equation 1.11, and therefore cannot see the portion of the losses corresponding to anomalous losses. At high frequencies, the predicted eddy current losses,  $W_e$ , overshoot the total losses even with the skin depth correction. This being an unphysical possibility, we will ignore the separation of anomalous losses and eddy current losses for these curves<sup>11</sup>. By plotting multiple losses per cycle versus frequency curves on the same plot, we can easily see the effect of varying other parameters, as we did in Figure 4.6. This is done in more detail in Chapter 5, leading to interesting results.

---

<sup>11</sup>At a later point, we will come back to analyzing the separation of eddy current and anomalous losses.

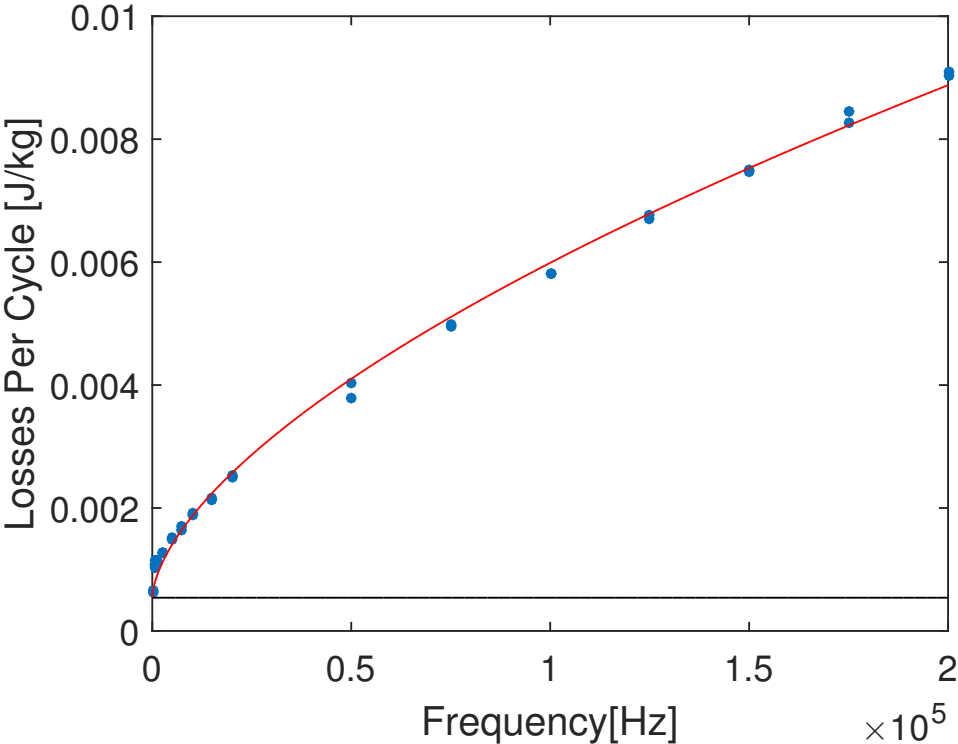


Figure 4.11: Power law fit of the losses per cycle versus frequency data is in red. Also plotted, in black, is the hysteresis losses for the sample.

## 4.5 Magnetic Annealing

<sup>12</sup>The final preparatory stage before we reach a final core that can be tested is the magnetic annealing of the core. From the literature, we know that magnetic annealing decreases the coercive field [72], increases the remnant magnetization [89], and lowers the total losses [90]. These results occur when the magnetic field anneal is applied longitudinally, or circumferentially in a toroidal core. The benefits of magnetic annealing are due to the rearrangement of the magnetic domains within the material, and their preferential orientation to the direction of the applied field after annealing. This allows the domains to be aligned in the direction of magnetization, thus requiring a smaller applied field to rotate the domains and saturate the sample. It also lessens the impact of pinning sites, since the domains walls will not have to traverse through as much of the material.

To carry out the magnetic annealing we developed a procedure adapted from our magnetic testing and stress annealing procedure, with guidelines provided by Luborsky [72]. We took a toroidal core whose magnetic properties had already been measured, wound it with a 30 AWG fiberglass insulated wire, and annealed it in a furnace while applying a DC current through the wire. The DC current in the wire also provided additional heating to the furnace, so we also wrapped a thermocouple wire with the toroidal core to measure the temperature of the additive effects. At high DC currents, the resistive heating from the wire raised the temperature above the desired annealing temperature, so instead of using a furnace, the sample was actively cooled with a flow of argon. Each anneal started at roughly 10 degrees Kelvin above the Curie temperature, and was held at that temperature for one hour. The core was then slowly cooled, 1 K/minute, through the Curie temperature, and held at 10 degrees Kelvin below the Curie temperature for 2 hours. Figure 4.12 displays the results of different currents through the wire with a plateau

---

<sup>12</sup>This section comes after magnetic measurements because it was developed and implemented quite late in our project.

in the losses occurring at 6 amps. The field applied for 6 amps is:

$$\begin{aligned}
 H &= \frac{\mu NI}{L} \\
 &= \frac{(58480 \cdot 4\pi \cdot 10^{-7}) \cdot 18 \cdot 6}{2\pi \cdot 0.002} \\
 &= 632 \frac{A}{m} = 80e
 \end{aligned} \tag{4.3}$$

which roughly corresponds to the applied field used by Luborsky [72], but with annealing occurring closer to the Curie temperature than Luborsky. The temperature relation to the Curie temperature is important since that relation controls how strong a ferromagnet the material is. In a classical view, the ferromagnetic characteristics of a material disappears at Curie temperature and are minimal just below it. This weak ferromagnetism does not require a large applied magnetic field to saturate the material, and align the domain walls.

With this in mind, the magnetic field applied by 6 Amps of electricity flowing through the wound wire is more than enough to fully saturate the material, as verified by Figure 4.12. Figure 4.12 displays the losses versus frequency of the same core with different annealed states. In between each magnetic anneal, the core was annealed with no applied field to remove the effect of the previous magnetic anneal. The stress annealed state has unaligned magnetic domain walls, and therefore has large losses due to the domain walls rotating to a large degree through pinning sites. While the 5 amp magnetically annealed state is a big improvement over the stress annealed state, it was still not fully annealed. At 6 and 7 amps, we can see that the sample is fully annealed, with the losses plateauing.

With our test methods fully developed, we now turn to the results of magnetic testing.

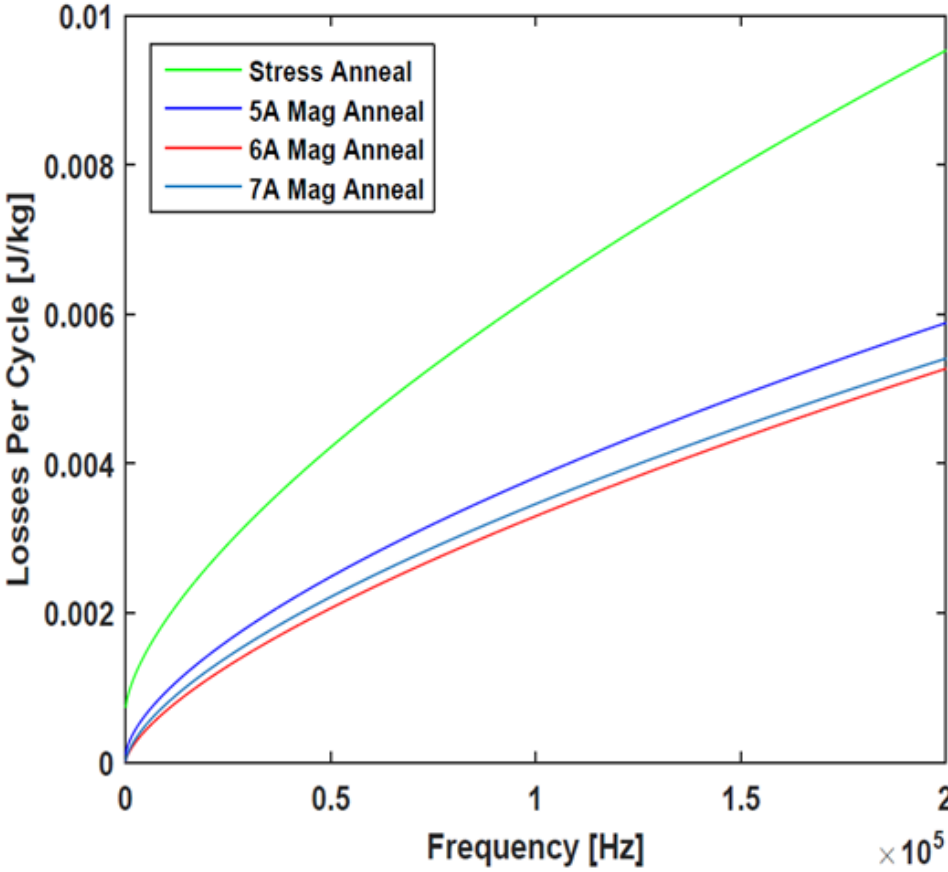


Figure 4.12: Effect of magnetic annealing on the losses per cycle in Fe<sub>68</sub>Mo<sub>4</sub>Ni<sub>3</sub>Co<sub>5</sub>-Si<sub>1</sub>B<sub>2.5</sub>P<sub>11.5</sub>C<sub>5</sub>.

## MINIMIZING LOSSES IN FERROMAGNETIC METALLIC GLASS CORES

This chapter focuses on minimizing losses in  $\text{Fe}_{68}\text{Mo}_4\text{Ni}_3\text{Co}_5\text{Si}_1\text{B}_{2.5}\text{P}_{11.5}\text{C}_5$ . The methodology behind this chapter can be found in Chapter 4, with this only having a nominal methods section. The impetus for this chapter once more came from working with the IIVI Foundation and Global Power Technology group and their desire for more efficient power transformers. The initial hypothesis though was spurred by a paper by Schwarz [46].

### 5.1 Abstract

Currently, 3% of losses in the United States' electrical grid come from power transformers. With ribbon thick metallic glasses, these losses can be significantly cut, but are metallic glass ribbons the best replacement material? We analyzed the effect of thickness on the losses in  $\text{Fe}_{68}\text{Mo}_4\text{Ni}_3\text{Co}_5\text{Si}_1\text{P}_{11.5}\text{C}_5\text{B}_{2.5}$  as a function of frequency, and found the optimal thickness that minimized the losses to exhibit a logarithmic dependency on frequency. This logarithmic relationship for  $\text{Fe}_{68}\text{Mo}_4\text{Ni}_3\text{Co}_5\text{Si}_1\text{P}_{11.5}\text{C}_5\text{B}_{2.5}$  states the optimal thickness of a core ranges from  $100\mu\text{m}$  to  $400\mu\text{m}$ , instead of in the  $<50\mu\text{m}$  range used currently. These larger optimal thicknesses are unexpected if anomalous losses are not considered, but the dominance of the anomalous losses at low frequencies validates the need for thicker power transformers. While other amorphous metals and casting techniques will yield varying results, the logarithmic dependence on frequency and the hundred micron optimal thickness range should be broadly applicable.

## 5.2 Introduction

Currently, a large majority of power transformers in the United States' energy grid is made of silicon-steel. Silicon-steel was initially developed in the 1890's, with the dominant alloys having  $\sim 4.5\%$  silicon, and rolled to a thickness of 0.014 inches for transformers [91]. Depending on the final composition of the steel, the sheets are either cold or hot rolled, to impart a grain structure that reduces the losses of the material. With the decades of development of Si-steel, the efficiency has been improved to 97% over all load capacities and frequencies used in the United States [16]. While this is highly efficient, it still accounts for roughly 150 billion kWh of energy lost each year in the U.S. These losses can be significantly reduced, up to 80%, by the use of more efficient transformer cores made of metallic glass cores, namely Metglas [16].

Unlike in other countries<sup>1</sup> where the need for power, or cost of generation is higher, the U.S. has yet to switch over to amorphous power transformers on a large scale. This has been an economic issue more than anything else, with the current generation of transformers having a lifetime of 50-60 years, and still having roughly 10 years left on their current lifetime [92]. Utility companies' willingness to switch over to amorphous power transformers could be changing though with the current generation of transformers nearing retirement, new energy mandates put out by the DOE [93], and the lower operating cost for amorphous transformers [16]. With this changeover likely happening over the next 10 to 20 years, we want to ensure that the new transformer materials are as efficient as possible.

When developing more efficient transformers, the traditional thinking has been that eddy current losses are the dominant type of loss. With that in mind, transformers have been developed to be very thin, with the  $50\mu\text{m}$  thick ribbons of Metglas being ideal. Unfortunately, the paper by Schwarz has upset this viewpoint

---

<sup>1</sup>Japan, China, and India have started to use amorphous power transformers to a greater degree than Europe or the U.S.

to some degree [46], and the effect of anomalous losses must be considered. In this chapter, we explore the conflict between  $W_e$  and  $W_a$  as the core thickness is varied in order to find an optimal thickness where  $W_t$  is minimized. We also want to investigate the frequency regimes where  $W_a$  is the dominant loss versus where  $W_e$  is dominant<sup>2</sup>.

While our initial hypothesis of a single optimal thickness is proven to be incorrect, we do discover that the optimal thickness exhibits a logarithmic dependency on frequency. The optimal thickness to minimize the total losses in a core ranges between  $150\mu\text{m}$  and  $400\mu\text{m}$  for stress annealed  $Fe_{68}Mo_4Ni_3Co_5Si_1P_{11.5}C_5B_{2.5}$ . When  $Fe_{68}Mo_4Ni_3Co_5Si_1P_{11.5}C_5B_{2.5}$  is magnetically annealed, the optimal thickness still displays a logarithmic dependency on the frequency, but its ideal range of thickness decreases to between  $100\mu\text{m}$  and  $300\mu\text{m}$ <sup>3</sup>. These optimal thickness ranges are unique to a given material with other materials appearing to have different optimal thicknesses<sup>4</sup>, but the logarithmic dependency of the optimal thickness on frequency is displayed in all tested materials.

---

<sup>2</sup>This was spurred by our grant providers at the II-VI Foundation being interested in both low frequency power transformers and high frequency transformers utilized in electric cars.

<sup>3</sup>Incidentally, the slope of the logarithmic fit does not change, but further work is needed to identify if this is an anomaly or not.

<sup>4</sup>Due to problems with both our testing equipment and the making of samples, we were limited to fully testing only one material.

### 5.3 Methods

Ingots of  $Fe_{68}Mo_4Ni_3Co_5Si_1P_{11.5}C_5B_{2.5}$  were prepared by induction melting and fluxing. The details of these procedures are described in Chapters 2 and 3. These alloys were chosen for their combination of good soft magnetic properties and good glass forming ability, with both rods being able to form 4 mm rods. The 4 mm rods were formed by the quartz quenching method, and then processed as described in Chapter 5, with toroids being formed out of the rods by EDM. The resistivity was measured using the four-point probes method with connective wires soldered onto both ends of a 2mm rod [94], and the density was measured via the Archimedes method, using distilled water as the immersive fluid [95].

To find the optimal thickness, where  $W_t$  is minimized, we kept the outer diameter and height constant across all samples, only varying the height. Primary and secondary coils were wound around the toroid using 30-AWG Cu-wire with both windings having 20 turns, and using a Walker AMH-200K-S Hysteresisgraph for all magnetic testing. After measuring the magnetic properties of these cores,  $W_t$  versus thickness curves were assembled as described in Chapter 5, using the fitted data from  $W_t$  vs  $f$  curves and the smoothing spline native to Matlab's curve fitting tool.

## 5.4 Results

We investigate the impact of toroid wall thickness on  $W_t$ . This experiment is motivated by a desire to further increase the efficiency of power transformer cores, thus enabling a more efficient energy grid. We also are hoping to gain a further understanding of anomalous losses and their contributions to the total losses. Our initial hypothesis of an optimal thickness that minimizes the total losses came from a paper by Schwarz [46]. This paper showed that the anomalous losses can play an important role in a cores efficiency, and that thicker cores could be more efficient. We want to take the conclusion of Schwarz one step further by finding an "optimal" thickness, where there is a minimum in the total losses.

To test this hypothesis we manufactured a number of toroidal cores of  $Fe_{68}Mo_4Ni_3Co_5Si_1P_{11.5}C_5B_{2.5}$ . These cores were nearly identical, with the one variable between them being their toroidal wall thicknesses. In Figure 5.1, we plot the losses per cycle versus the frequency for 6 cores<sup>5</sup> with thicknesses ranging from 0.18 mm to 0.65 mm, and heights of 0.85 mm. We plot  $W_t$  vs.  $f$ , as described in section 4.4, with  $f$  ranging from 0 Hz to 200,000 Hz. From this plot it appears that the thinnest core, at 0.18 mm, has the lowest losses, while the thickest core, at 0.65 mm, has the highest losses. This suggests that our initial hypothesis of a single thickness that minimizes the losses at some intermediary thickness is incorrect. At higher frequencies,  $W_e$  is dominates the losses as the thickness squared term in Equation 1.12 is the driving geometric term for all of the losses. This picture changes though if we examine the losses at low frequencies.

In Figure 5.2, we plot  $W_t$  vs.  $f$ , as in Figure 5.1, but now the frequency ranges from 0 Hz to 2500 Hz, instead of from 0 Hz to 200,000 Hz. The same thicknesses as in Figure 5.1, ranging from 0.18 mm to 0.65 mm, are displayed with the same color coding. At this frequency range, the traditional picture of  $W_e$  being

---

<sup>5</sup>This is a representative sample of the cores tested. The smallest wall thickness that can be made via EDM is 0.11 mm.

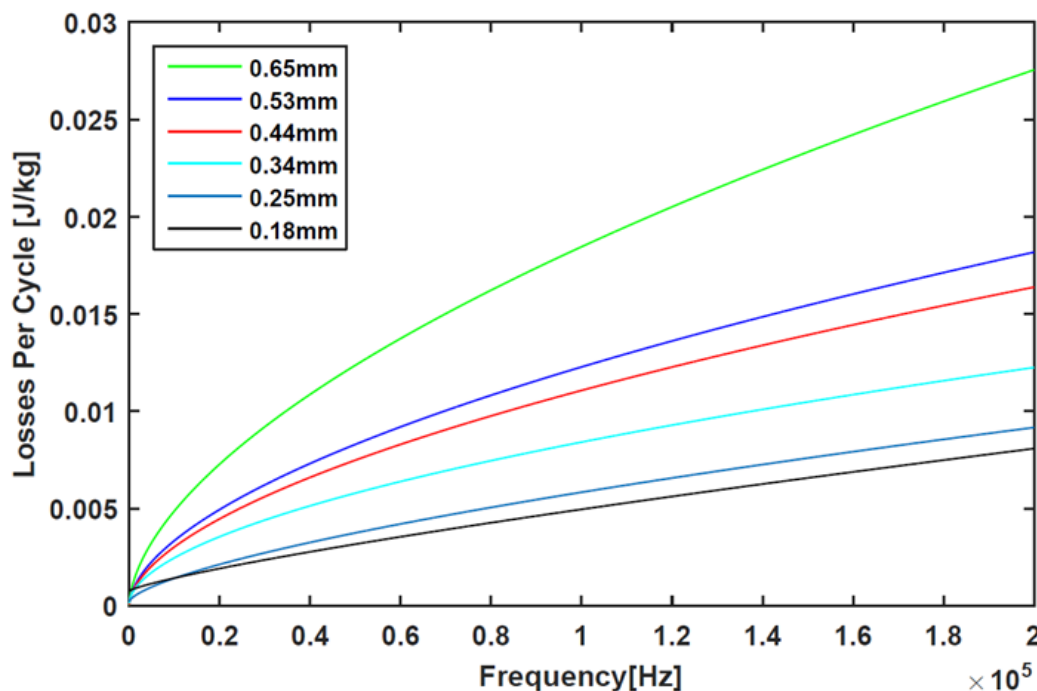


Figure 5.1: Losses per cycle as a function of frequency for  $\text{Fe}_{68}\text{Mo}_4\text{Ni}_3\text{Co}_5\text{Si}_1\text{B}_{2.5}\text{P}_{11.5}\text{C}_5$  of varying core thickness, ranging from 0.18 mm to 0.65 mm. At high frequencies the traditional viewpoint of eddy current losses dominating is correct.

the dominant loss term behind  $W_t$  is no longer applicable. We see the inverse of the loss picture at 200,000 Hz, with the 0.18 mm core having the highest losses and the 0.65 mm core having the lowest losses. This flipping in core efficiency is due to two factors: (1)  $W_h$ 's reliance on the thickness, and the differing dependence on frequency between all three loss types. In Figure 5.2, we can see that the hysteresis losses increase as the thickness decrease. This suggests that the increased surface area to volume ratio is linked to an impediment of domain wall movement, most likely due to an increase in the importance of surface pinning sites. In Figure 5.2 we also see a crossover in the loss curves. As the frequency increases, the thicker cores' losses increase at faster rates leading to the thinnest core being the most efficient at high frequencies. This is due to the differing dependency of each loss type on the frequency with  $W_h$  being independent of frequency,  $W_e$  is proportional to  $f$ , and  $W_a$  is proportional to  $f^{\frac{1}{2}}$  [63]. This differing dependence stops  $W_e$  from dominating

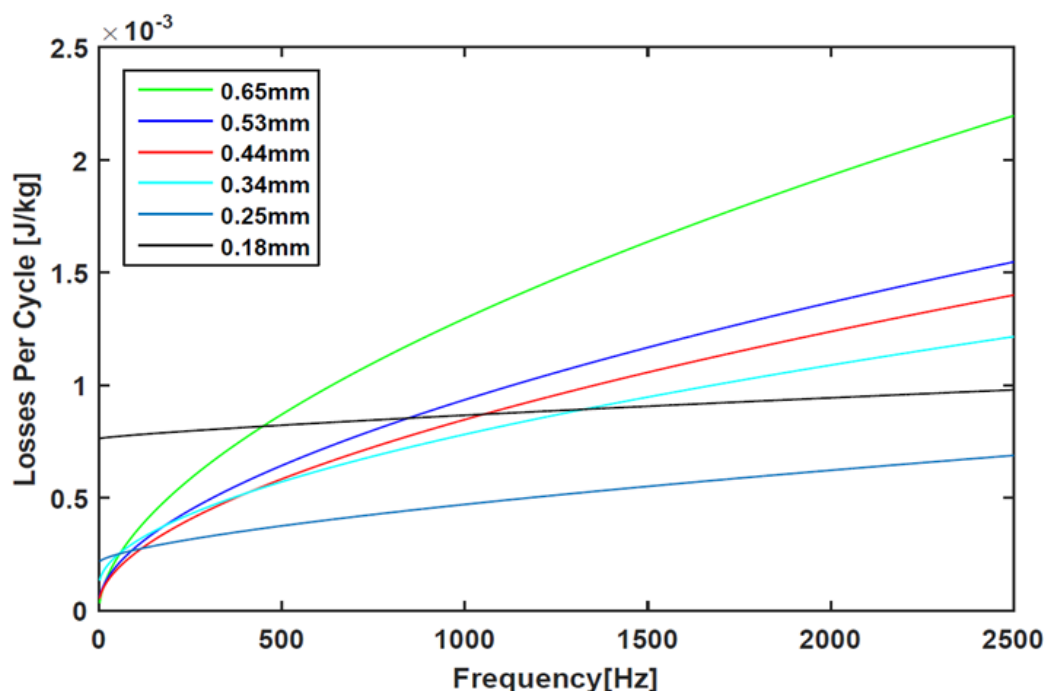


Figure 5.2: Losses per cycle as a function of frequency at low frequencies for  $\text{Fe}_{68}\text{Mo}_4\text{Ni}_3\text{Co}_5\text{Si}_1\text{B}_{2.5}\text{P}_{11.5}\text{C}_5$  of varying core thickness, ranging from 0.18 mm to 0.65 mm. The transition in efficiency begins to become apparent at these frequencies.

until higher frequencies. It also allows  $W_h$  and  $W_a$  to control the losses at lower frequencies where the losses are inversely proportional to the thickness. With this in mind, we can look at a given frequency to see which toroidal core thickness leads to a minimum in  $W_t$ .

Figure 5.3 is a cross-sectional view of the two previous plots, with the total losses plotted against the thickness,  $\tau$ , instead of against the frequency. This figure is one of many devised to find the optimal toroidal core thickness that minimizes the total losses, with the frequency being 250 Hz, and the maximum magnetization 0.1 T. Each data point in black is the losses for a given  $\tau$  is taken from the power law fit of the raw data, as seen in Figure 4.11. The red curve fits the individual data points with a smoothing spline from Matlab's curve fitting tool. A smoothing spline was necessary to fit the data due to the disparate sections. Each section is dominated by a different type of loss, and there are no representative equations to fit each of these

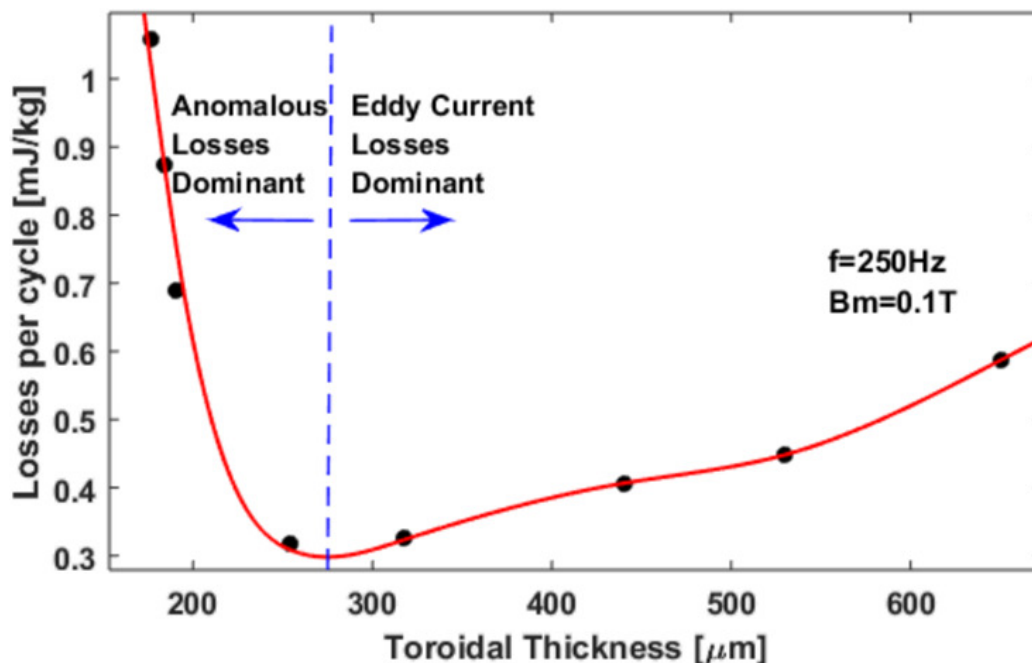


Figure 5.3: Losses per cycle versus the thickness of  $\text{Fe}_{68}\text{Mo}_4\text{Ni}_3\text{Co}_5\text{Si}_1\text{B}_{2.5}\text{P}_{11.5}\text{C}_5$  toroidal cores, at a frequency of 250 Hz and a max magnetization of 0.1 T. The minimum was found through the use of a smoothing spline.

loss types with a high enough precision.

Using the smoothing spline, we find that at 250 Hz, there is a minimum in  $W_t$  for  $\tau \approx 280$  microns. This minimum divides the fit into two sections: an anomalous loss dominant section, and an eddy current loss dominant section. The anomalous loss dominant section is a misnomer at some frequencies since this section is sometimes dominated by  $W_h$  instead of  $W_a$ <sup>6</sup>. Here, we can see that thinner cores cause large increases in  $W_a$  and  $W_h$  leading to them becoming less efficient. Similarly, if a core is too thick then  $W_e$  takes over, and the efficiency is likewise lessened. This balance between the two sections leads to the minimum in the losses, a minimum which can be found for any frequency.

<sup>6</sup>There is no reason why a third area could not exist, one that divides the current anomalous loss dominant section into one dominated by  $W_a$  and another dominated by  $W_h$ . Unfortunately we could not explore this possibility due to the limitations of our testing setup. It has also been proposed that anomalous losses are just the frequency dependent portion of the hysteresis losses and not a separate type.

With the knowledge of a minimum in the losses for a given frequency, our next step was to extend Figure 5.3 over a broad range of frequencies. To make the  $W_t$  vs.  $\tau$  curve which would show these minima, we needed to have enough data at any given frequency to create an accurate smoothing spline. This required there to be a given number of tested cores with  $\tau$ s on either side of the theoretical minimum. This requirement, along with the shortcomings of our EDM process, and the limitations of the Hysteresisgraph leads to a limited frequency range<sup>7</sup> where we can accurately find a minimum. Figure 5.4 displays the optimal thickness regime for stress annealed cores of  $\text{Fe}_{68}\text{Mo}_4\text{Ni}_3\text{Co}_5\text{Si}_1\text{B}_{2.5}\text{P}_{11.5}\text{C}_5$  over a large range of frequencies. Each of the blue data points represent the optimal thickness found by fitting  $W_t$  versus  $\tau$  data, as seen in Figure 5.3, with a smoothing spline. With the limitations listed above, optimal thickness were found for frequencies extending from 250 Hz to 20,000 Hz. We then fit these data points with the red curve, which has an equation of the form:

$$\tau_o = a \cdot \log(b \cdot f) + c \quad (5.1)$$

where  $\tau_o$  is the optimal thickness,  $f$  is the frequency, and the other variables are constants. While this gives a good fit of our data, for the data range given, it should only be extended an order of magnitude or two in either direction for any given fit. There is no rational for why the fit of the data has to stay logarithmic, and why it shouldn't change as we approach 0 Hz, or as we approach very high frequencies where a logarithmic fit would give a negative, non-physical, thickness. At high enough frequencies, we expect the fit to flatten out as some minimum optimal thickness is reached, while near zero the variable surface of the core would lead to a number of possibilities. In addition to the plot of optimal thickness vs. frequency, Figure 5.4 contains the rough thickness range that Metglas ribbons can be cast at.

<sup>7</sup>A limited thickness range usually still extends several orders of magnitudes but not the full range of frequencies at which power transformers are run.

While our tests are not made out of the same material as Metglas, they do suggest that Metglas is currently not at an optimal thickness for all applications which it is currently used for. This is especially true for low frequency power transformer applications. Unfortunately, Metglas cannot be made into thicker toroidal cores, so an alternative material would be needed to capitalize on the higher possible efficiencies.

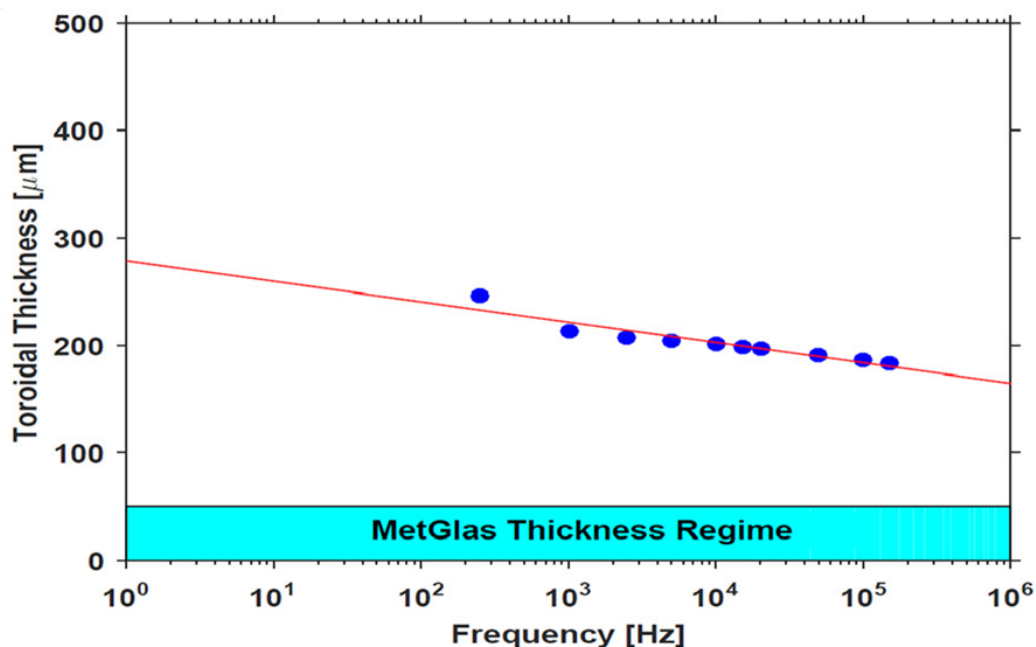


Figure 5.4: Optimal thickness of a stress annealed core made out of  $\text{Fe}_{68}\text{Mo}_4\text{Ni}_3\text{Co}_5\text{-Si}_1\text{B}_{2.5}\text{P}_{11.5}\text{C}_5$  versus the frequency that the core is run at. The fit of the data is logarithmic in nature.

In addition to finding the optimal thickness as a function of frequency, we also tested the impact of other parameters, namely the maximum magnetization, and annealed state. Figure 5.5 shows the effect of altering the maximum magnetization. Here, optimal thickness curves for maximum magnetizations of 0.15 T and 0.2 T are plotted with the same curve, for  $B_m = 0.1T$ , from Figure 5.4. From Equation 1.11, we expected the two to four times increase in  $W_e$  to lead to thinner curves being more prevalent, but Figure 5.5 tells a different story. Instead of the optimal thickness curve shifting downwards as  $B_m$  increases, the negative slope increases

in steepness. This leads to even thicker cores being desired to minimize losses at low frequency, and cores in the 10s of micron thickness range being desired at high frequencies.

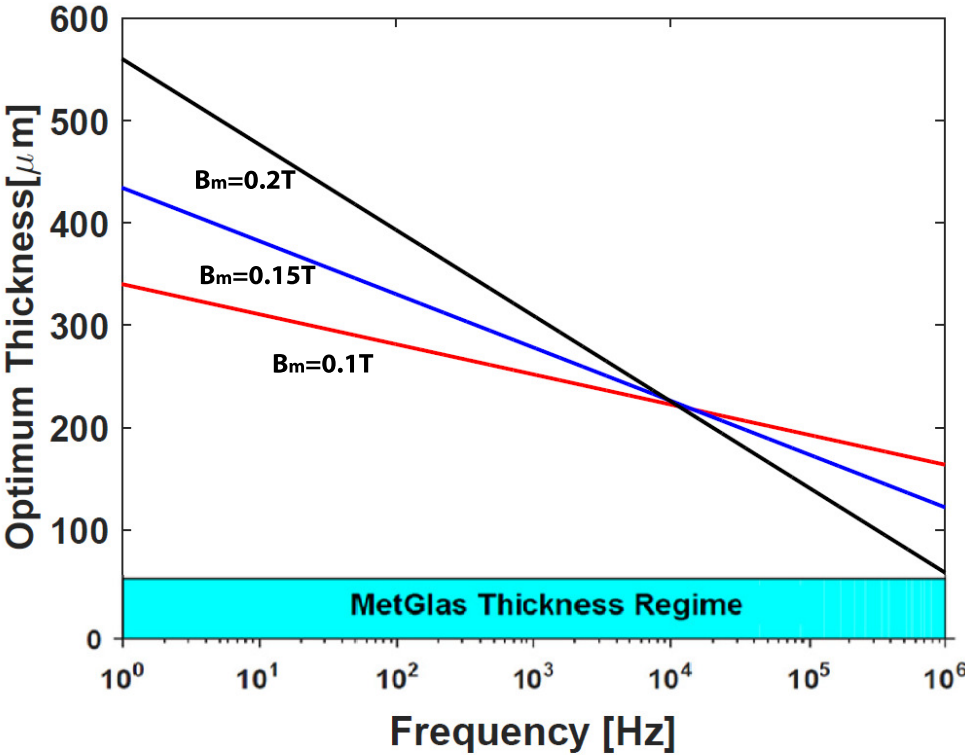


Figure 5.5: Optimal thickness as a function of the maximum magnetization. The slope of the optimal thickness curve steepens as  $B_m$  increases.

The cause of the increasing steepness with increasing  $B_m$  is the role  $B_m$  plays on the anomalous losses. It appears that  $B_m$  plays an important role in  $W_a$ , and that  $W_a$  has a squared<sup>8</sup> on the maximum magnetization. This causes the anomalous losses to become more dominant at the lower frequencies while the eddy current losses are still not a factor. Additionally, when finding the optimal thickness at these higher magnetizations, as we did in Figure 5.3, there is a much narrower well around the optimal thickness,  $\tau_o$ . This, along with the steepness of the optimal thickness curve, causes any given core to be applicable over a much small frequency range if

<sup>8</sup>Or higher.

it is used at high values of  $B_m$ . In a power transformer,  $B_m$  will be much closer to the saturation magnetization of the material than it was in these tests. The stretching  $\tau_o$  will then be even more exaggerated, leading to thick cores being optimal at low frequencies, while cores of Metglas thickness being optimal at high frequencies. However, I'd like to reiterate that while the logarithmic fits do correspond very well to the data, the optimal thickness curves are extrapolated on both ends of the frequency spectrum. The fit could easily change as the frequency approaches 0 Hz, and will have to change at high frequencies where  $\tau_o$  approaches a thickness of 0.

In addition to investigating the dependency of  $\tau_o$  on  $f$  and  $B_m$ , we also looked at the effect of annealing on the optimal thickness curve. Thus far in Chapter 5 we have only dealt with stress annealed cores made out of  $\text{Fe}_{68}\text{Mo}_4\text{Ni}_3\text{Co}_5\text{Si}_1\text{B}_{2.5}\text{P}_{11.5}\text{C}_5$ , but we will now cores that have been magnetically annealed according to the methods set out in Chapter 4.5. In Figure 5.6, we once more have a plot of  $\tau_o$  versus  $f$ , with the same data from Figure 5.4 represented by the red data points and black curve. Below that, the green points are optimal thicknesses for the same group of cores, but now magnetically annealed. The blue dotted line is the fit for the stress annealed data, but shifted down in the y direction by 50 microns<sup>9</sup>. This downwards shift in  $\tau_o$  is predictable, since the magnetic annealing will not affect  $W_e$ , and thus thinner cores will be more efficient. Magnetic annealing only lowers the hysteresis and anomalous losses, allowing for easier domain wall rotation.  $W_e$  on the other hand, is only reliant on the base material properties, which are not affected by either stress or magnetic annealing. With  $W_h$  and  $W_a$  being lowered,  $W_e$  can play a dominant role over a larger frequency range, becoming important at lower frequencies and shifting the optimal thickness curve downwards. The unexpected part of the shift, is how well the fit for the stress anneal fits the magnetic annealing data. It appears that the slope of the fit does not change at all, but with no other data to

---

<sup>9</sup>There is not a large enough range of magnetic anneal data to fit the data with a high degree of accuracy.

affirm this and no viable hypothesis for no change in the slope, we must say that this is only a coincidence at this time.

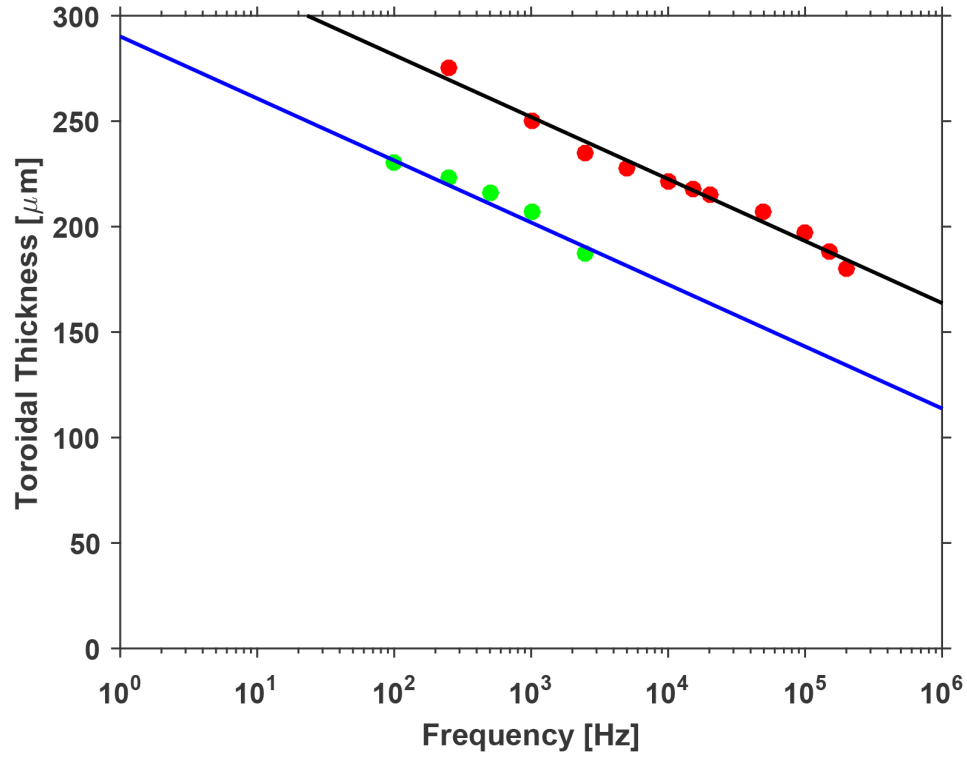


Figure 5.6: Magnetic annealing shifts the optimal thickness curve to a lower thickness range by decreasing  $W_a$ , while not affecting  $W_e$ .

## 5.5 Conclusion

The low value of the anomalous losses in annealed ferromagnetic bulk metallic glasses makes them ideal materials for low frequency applications. At high frequencies,  $W_e$  takes over as the dominant loss due to its proportionality to  $f$ , while  $W_a$  is only proportionality to  $f^{0.5}$ . This differing dependence on frequency creates a logarithmic relationship between  $\tau_o$  and  $f$ , with  $\tau_o$  ranging from 160 to  $350\mu m$ , and decreasing with increasing frequency. As  $B_m$  increases, the steepness of the logarithmic decay in  $\tau_o$  increases, favoring thicker cores at low frequencies and thinner cores at high frequencies. When  $Fe_{68}Mo_4Ni_3Co_5Si_1P_{11.5}C_5B_{2.5}$  is magnetically annealed, the optimal thickness still displays a logarithmic dependency on the frequency, but its ideal range of thickness decreases to between  $150\mu m$  and  $300\mu m$ .

If core packing density and coil losses were accounted for, the logarithmic dependencies would be shifted to higher thicknesses for all frequencies, since thicker cores are denser. Although the range of material properties, casting techniques and surface finishes between ferromagnetic metallic glass cores does vary, the idea of an optimal thickness, its logarithmic dependence, and how it varies with other variables should be broadly applicable. These optimal thicknesses suggest that the current Metglas cores at peak efficiencies, even if they are better than Si-steel. This drives forward the need for the further development, and use of ferromagnetic bulk metallic glasses as low frequency soft magnetic materials.

## CONCLUSION AND CONTINUATION OF THIS THESIS

### 6.1 Conclusion

In this thesis, we have run the gambit on how to improve the ferromagnetic metallic glass field, from alloy development, to chemical reactions in purification stages, to transformer efficiency. While working on the development of an Fe-based glass, we identified an exchange of Si for B occurring during boron oxide fluxing of the Fe-Co-Si-B-P system, where a significant enrichment of B in the alloy is accompanied by a significant depletion of Si. The ratio of B gained to the Si lost is roughly consistent with the reaction  $2B_2O_3 + 3Si \rightarrow 4B + 3SiO_2$ , suggesting that  $B_2O_3$  is reduced by Si extracted from the alloy to form  $SiO_2$ , resulting in the addition of B to the alloy. This reaction was found to occur in all other Si-bearing metallic glasses that are fluxed with boron oxide, but the rate of each reaction changed dramatically between systems. This reaction was also utilized in a unique optimization strategy to purify the melt, while simultaneously accounting for the compositional shift thereby optimizing the Fe-Co-Si-B-P system for glass forming ability. An alloy, demonstrating a global maximum in glass forming ability is found, having a pre-fluxed composition  $Fe_{57.5}Co_{20.2}Si_{10.2}B_{2.1}P_{10}$ , with a glass forming ability of 0.5 mm, and post-fluxed composition  $Fe_{57}Co_{19.2}Si_{6.8}B_{7.4}P_{9.6}$ , with a glass forming ability of 5 mm, along with a magnetic saturation of 1.53 T.

While developing  $Fe_{57}Co_{19.2}Si_{6.8}B_{7.4}P_{9.6}$ , and investigating the role fluxing plays on the composition of the alloy, we also explored the factors behind losses in a power transformer core. We found that the dominant loss type greatly depends on the frequency, with the importance of  $W_a$  making thicker cores optimal at low frequency, while  $W_e$  only takes over at higher frequencies. This change in depen-

dency is due to  $W_a$  being proportional to  $f^{\frac{1}{2}}$ , while  $W_e$  is proportional to  $f$ . This leads to a logarithmic relation between  $\tau_o$  and  $f$ , and an optimal thickness ranging from 160 to 350  $\mu\text{m}$  for stress annealed  $Fe_{68}Mo_4Ni_3Co_5Si_1P_{11.5}C_5B_{2.5}$ . When  $Fe_{68}Mo_4Ni_3Co_5Si_1P_{11.5}C_5B_{2.5}$  is magnetically annealed, the optimal thickness still displays a logarithmic dependency on the frequency, but its ideal range of thickness decreases to between 100  $\mu\text{m}$  and 300  $\mu\text{m}$ .

These experiments have shown that we have yet to reach a peak in efficiency for amorphous power transformers, and more research is still required to do so. Below I will outline 3 separate projects that I feel could further advance the use and production of amorphous power transformers. Each of these projects could be a thesis in themselves, and all of them would advance the metallic glass field as well as the power transformer field. For those of you who have read this thesis in its entirety<sup>1</sup>, I'd like to thank you, and invite you to work on any ideas or problems this thesis has brought to mind.

---

<sup>1</sup>Or even just a part of it.

## 6.2 Development of Amorphous, Ferromagnetic Wires

The first proposed project may seem like low hanging fruit, but it has vexed the metallic glass community for some time, that is the casting of metallic glass wires. Amorphous metal wires are an ideal target for production due to the high aspect of the wire allowing for very high cooling rates. This led to work on these wires as early as 1979 [96]. These early wire drawing experiments showed that the mechanical properties of an alloy would be improved by wire drawing due to a "work hardening" process that occurred due to intersecting shear bands, but the poor tensile mechanical properties of metallic glasses limited their uses. In 1981, a secondary wire manufacturing method was developed which was a variant of the traditional spin casting process [97]. This method was a large improvement over the drawn wires as it could be done from a liquid state, and it could continuously cast wires. Unfortunately it could only cast wires between 0.08 mm and 0.5 mm, and it did not improve the mechanical properties. While the first metallic glass wires were Pd-based, metallic glass wires soon moved towards Fe-based wires for their magnetic applications [98], but they were never looked at for power transformers, only the pulse effects and magnetomechanical effects were studied in detail. While this is true, there has continued to be limited interest in Fe-based metallic glass wires over the years, researching oxide layer formation [99], and the further optimization of the casting process [100].

With this background in mind, it appears to me that ferromagnetic metallic glass wires would be a perfect opportunity for further optimizing amorphous power transformers. From our work on optimizing the efficiency of transformers, we can see that the thickness regime that amorphous wires can be cast would be ideal for most frequencies. In addition to this, the circular cross-section of the wire would be ideal for lowering all three types of losses.  $W_h$  should be lowered by the lack of pinning sites on the surface of the wire, negating some of the disadvantages of

making thinner cores.  $W_a$  should be lower as well, looking at volume to surface area ratio of a circle:

$$\left(\frac{V}{A}\right)_c = \frac{\pi r^2 \cdot l}{2\pi r \cdot l} = \frac{\pi r}{2} \quad (6.1)$$

Versus that of a square<sup>2</sup>:

$$\left(\frac{V}{A}\right)_s = \frac{s^2 \cdot l}{4s \cdot l} = \frac{s}{4} \quad (6.2)$$

and setting their volumes to be equal:

$$\begin{aligned} V_c &= V_s \\ \pi r^2 \cdot l &= s^2 \cdot l \\ r &= \frac{s}{\sqrt{\pi}} \end{aligned} \quad (6.3)$$

then we find that the volume to surface area ratio of a circle is greater than that of a square, theoretically reducing  $W_a$ :

$$\begin{aligned} \left(\frac{V}{A}\right)_c &> \left(\frac{V}{A}\right)_s \\ \frac{\pi r}{2} &> \frac{s}{4} \\ \frac{\sqrt{\pi}s}{2} &> \frac{s}{4} \\ \sqrt{\pi} &> \frac{1}{2} \end{aligned} \quad (6.4)$$

$W_e$  would also be lower if the cross-section of a transformer core were circular, with  $\beta$ , the geometrical term in the denominator Equation 1.11 reaching a minimum of 6 for a ribbon, while attaining a value of 16 for a circular cross-section.

Not only would a wire transformer decrease  $W_t$ , but it would also provide an

---

<sup>2</sup>A square is assumed versus a rectangle for simplicities sake.

avenue for commercially manufacturing toroids in the optimal thickness range for a number of frequencies. Currently, there are only two commercial casting techniques for metallic glasses: spin-casting, and the Liquidmetal Engel machine. While spin-casting is limited to thickness ranges of up to  $\sim 100$  microns, the Engel machine is limited to a minimum thickness of 1 mm [101]. This leaves wire casting as one of the few possible processes which can access the optimal casting window without additional machining steps. Metallic glass wires could also be easily magnetically annealed, more so than cast rings, since the annealing process could be done while the wires are drawn and wound. The third benefit of wire casting is the oxidization of the surface of the wires [99], this layer would act as a nonconducting medium, separating each wind of amorphous wire to prevent large eddy currents, but without the need to coat the wires as is done with metallic glass ribbons. Last of all, the wires could be continuously cast with an already proven technology, allowing for the quick scale up of this technology to meet commercial demand.

While amorphous wires have existed for quite some time, they have not been utilized due to a lack of purpose. With the need to cast amorphous toroids in a thickness range accessible to wire casting though, and with the benefits listed above, ferromagnetic amorphous wires could easily supplant other materials for low frequency applications. Continued research in this field is needed though to confirm the theoretical benefits, but the possible commercial and scientific benefits should make that research worthwhile.

### 6.3 Mechanics of Fe-based metallic glasses

My second proposed project for a future researcher is the study of the mechanical behavior of Fe-based metallic glasses, specifically looking at why fracture toughness in Fe-based alloys is much lower than in other metallic glasses [65]. One of the major things limiting Metglas and other Fe-based amorphous ribbons to such low thicknesses is their low fracture toughness, and lack of overall ductility. When too thick of a ribbon is wound, instead of bending, it catastrophically fractures and caps the overall thickness at roughly 50 microns. If metallic glass wires were to be developed, this same problem could be run into, although the geometry of the wire would lend itself to more ductility and the casting procedure could be tailored to impart a desired radius of curvature on the wire without imparting additional stresses. While this project is much less fleshed out than the previous, the study of the mechanical properties of metallic glasses is already a very active field and research could be continued from there.

The three proposed mechanisms for this study are alloy development, mechanical testing to develop theory, and theoretical modeling. The alloy development path is the most traditional, having the researcher follow the data to reach an alloy which hopefully has good mechanical properties. This method though has been tried for quite some time and has yet to yield any clues on how to mitigate the brittleness of Fe-based metallic glasses. The second method of mechanical testing and theory development is still in its nascence. Good theory for the mechanics of metallic glasses have yet to be developed and a comprehensive theory would have immense implications well beyond the field of Fe-based metallic glass. Finally, the modeling of metallic glasses and their properties has been attempted for some time, and is barely making any headway in more basic systems [102]. While this would be the best method for overcoming the limitations in toughness, this avenue will most likely have to wait for advancements in theory, or advances in computing

power.

## 6.4 Modeling of Losses

While there exists models for losses in some scenarios, there has yet to be any model that can predict the total losses for a given set of parameters. Without this, development of amorphous power transformer cores is stuck to empirical testing and the limitations that go along with it. Unfortunately, the issues with this prediction mainly stem from our understanding, or lack thereof, of anomalous losses. Without an actual understanding of what is occurring in anomalous losses, there is no way to predict the total losses. This project is mostly outside of my wheelhouse, being more for a computational electrical engineer than for an experimental material scientist, but I press those in the community who better understand this field to tackle it with gusto.

## BIBLIOGRAPHY

- [1] E. Ma and Z. Zhang. “Amorphous Alloys: Reflections from the glass maze”. In: *Nat. Mat.* 10 (2011), pp. 10–11.
- [2] W. Klement, R.H. Willens, and P. Duwez. “Non-crystalline Structure in Solidified Gold–Silicon Alloys”. In: *Nat.* 187 (1960), pp. 869–870.
- [3] H.W. Kui, A.L. Greer, and D. Turnbull. “Formation of bulk metallic glass by fluxing”. In: *Appl. Phys. Lett.* 45 (1984), pp. 615–616.
- [4] H.S. Chen. “Thermodynamic considerations on the formation and stability of metallic glasses”. In: *Acta Metal.* 22 (1974), pp. 1505–1511.
- [5] A. Peker and W.L. Johnson. “A highly processable metallic glass:  $Zr_{41.2}Ti_{13.8}Cu_{12.5}Ni_{10.0}Be_{22.5}$ ”. In: *Appl. Phys. Lett.* 63 (1993), pp. 2342–2344.
- [6] A. Inoue, T. Zhang, and T. Masumoto. “Al-La-Ni Amorphous Alloys with a Wide Supercooled Liquid Region”. In: *Mat. Trans., JIM* 30 (1989), pp. 965–972.
- [7] D. Turnbull. “Kinetics of Heterogeneous Nucleation”. In: *J. Chem. Phys.* 18 (1950), pp. 198–203.
- [8] D. Turnbull and J.C. Fisher. “Rate of Nucleation in Condensed Systems”. In: *J. Chem. Phys.* 17 (1949), pp. 71–73.
- [9] M. Demetriou, M. Launey, G. Garrett, J. Schramm, D. Hofmann, W. Johnson, and R. Ritchie. “A damage-tolerant glass”. In: *Nat. Mat.* 10 (2011), pp. 123–128.
- [10] J. Scully, A. Gebert, and J. Payer. “Corrosion and related mechanical properties of bulk metallic glasses”. In: *J. Mat. Res.* 22 (2007), pp. 302–313.
- [11] H. Warlimont. “The Impact of Amorphous Metals on the Field of Soft Magnetic Materials”. In: *Mat. Sci. Eng.* 99 (1988), pp. 1–10.
- [12] C. Kittel, ed. *Introduction to Solid State Physics, 8th Edition*. John Wiley and Sons, 2004.
- [13] R. Umetsu, R. Tu, and T. Goto. “Thermal and Electrical Transport Properties of Zr-Based Bulk Metallic Glassy Alloys with High Glass-Forming Ability”. In: *Mat. Trans.* 53 (2012), pp. 1721–1725.
- [14] T. Egami, P.J. Flanders, and C.D. Graham. “Low-Field Magnetic-Properties of Ferromagnetic Amorphous Alloys”. In: *App. Phys. Let.* 26 (1975), pp. 128–130.
- [15] “Metglas”. In: <http://www.metglas.com/> (Accessed: 2017-05-26).

- [16] C.W. Gellings. *The Smart Grid. Enabling energy efficiency and demand response*. The Fairmont Press, 2009.
- [17] W.L. Johnson. “Bulk amorphous metal—An emerging engineering material”. In: *JOM* 54 (2002), pp. 40–43.
- [18] W.L. Johnson and J. Plummer. “Is metallic glass poised to come of age?” In: *Nat. Mater.* 14 (2015), pp. 553–555.
- [19] M.H. Cohen and D. Turnbull. “Composition Requirements for Glass Formation in Metallic and Ionic Systems”. In: *Nat.* 189 (1961), pp. 131–132.
- [20] T.D. Shen and R.B. Schwarz. “Bulk ferromagnetic glasses prepared by flux melting and water quenching”. In: *Appl. Phys. Lett.* 75 (1999), pp. 49–51.
- [21] A. Inoue, T. Zhang, H. Koshiba, and A. Makino. “New bulk amorphous Fe–(Co,Ni)–M–B (M=Zr, Hf, Nb, Ta, Mo, W) alloys with good soft magnetic properties”. In: *J. Appl. Phys.* 83 (1998), pp. 49–51.
- [22] A. Inoue. “High Strength Bulk Amorphous Alloys with Low Critical Cooling Rates (Overview)”. In: *Mat. Trans.* 36 (1995), pp. 866–875.
- [23] Y.S. Yun, H.S. Nam, P.-R. Cha, W.T. Kim, and D.H. Kim. “Effects of Atomic Size Difference and Heat of Mixing Parameters on the Local Structure of a Model Metallic Glass System”. In: *Met. Mater. Int.* 20 (2014), pp. 105–111.
- [24] M. Shimono and H. Onodera. “Geometrical and Chemical Factors in the Glass-Forming Ability”. In: *Scripta Mat.* 44 (2001), pp. 1595–1598.
- [25] A. Inoue, N. Nishiyama, and H. Kimura. “Preparation and Thermal Stability of Bulk Amorphous Pd<sub>40</sub>Cu<sub>30</sub>Ni<sub>10</sub>P<sub>20</sub> Alloy Cylinder of 72 mm in Diameter”. In: *Mat. Trans., JIM* 38 (1997), pp. 179–183.
- [26] D. Granata, E. Fischer, V. Wessels, and J.F. Löffler. “Fluxing of Pd–Si–Cu bulk metallic glass and the role of cooling rate and purification”. In: *Acta Mat.* 71 (2014), pp. 145–152.
- [27] J.H. Na, M. Demetriou, M. Floyd, A. Hoff, G. Garrett, and W.L. Johnson. “Compositional landscape for glass formation in metal alloys”. In: *Proc. Natl. Acad. Sci.* 111 (2014), pp. 9031–9036.
- [28] F. Li, B. Shen, A. Makino, and A. Inoue. “Excellent soft-magnetic properties of (Fe,Co)–Mo–(P,C,B,Si) bulk glassy alloys with ductile deformation behavior”. In: *Appl. Phys. Lett.* 91 (2007), pp. 234101-1–234101-3.
- [29] B.D. Cullity and C.D. Graham. *Introduction To Magnetic Materials*. John Wiley and Sons, 2009.

- [30] P. Weiss. “The variation of ferromagnetism with temperature”. In: *Comptes Rendus Hebdomadaires des Seances de l’Academie des Sciences* 143 (1906), pp. 1136–1139.
- [31] J.C. Slater. “Atomic shielding constants”. In: *Phys. Rev.* 36 (1930), pp. 57–64.
- [32] E.C. Stoner. “Atomic moments in ferromagnetic metals and alloys with non-ferromagnetic elements”. In: *Phil. Mag.* 15 (1933), pp. 1018–1034.
- [33] M. Bañobre-López, C. Vázquez-Vázquez, J. Rivas, and M.A. López-Quintela. “Magnetic properties of chromium (III) oxide nanoparticles”. In: *Nanotech.* 14 (2003), pp. 318–322.
- [34] S. Chikazumi. *Physics of Ferromagnetism*. Oxford University Press, 1997.
- [35] A.I. Gubanov. “Quasi-Classical Theory of Amorphous Ferromagnetics”. In: *Sov. Phys.-Sol. State* 2 (1960), pp. 468–471.
- [36] P. Duwez and S.C.H. Lin. “Amorphous Ferromagnetic Phase in Iron-Carbon-Phosphorus Alloys”. In: *J. Appl. Phys.* 38 (1967), pp. 4096–4097.
- [37] R.J. Gambino, P. Chaudhari, and J.J. Cuomo. “Amorphous Magnetic Materials”. In: *AIP Conf. Proc.* 18 (1974), pp. 578–592.
- [38] Y.Q. Cheng, E. Ma, and H.W. Sheng. “Atomic Level Structure in Multi-component Bulk Metallic Glass”. In: *Phys. Rev. Lett.* 102 (2009), pp. 245501-1–245501-4.
- [39] H. Warlimont. “The Impact of Amorphous Metals on the Field of Soft Magnetic Materials”. In: *Mat. Sci. Eng.* 99 (1988), pp. 1–10.
- [40] A. Tschumi, T. Laubscher, R. Jeker, E. Schupfer, H.U. Kunzi, and H.J. Guntherodt. “Electrical resistivity and Hall coefficient of glassy and liquid alloys”. In: *J. Non-Cryst. Solids* 61–62 (1984), pp. 1091–1096.
- [41] P.J. Cote. “Electrical resistivity of amorphous nickel phosphorus alloys”. In: *Solid State Comm.* 18 (1976), pp. 1311–1313.
- [42] O. Haruyama, N. Annoshita, H. Kimura, N. Nishiyama, and A. Inoue. “Anomalous behavior of electrical resistivity in glass transition region of a bulk Pd<sub>40</sub>Ni<sub>40</sub>P<sub>20</sub> metallic glass”. In: *J. Non-Cryst. Solids* 312 (2002), pp. 552–556.
- [43] F. L. Cumbreira, H. Miranda, A. Conde, R. Márquez, and P. Vigier. “Crystallization kinetics of Fe<sub>40</sub>Ni<sub>38</sub>Mo<sub>4</sub>B<sub>18</sub> and Fe<sub>80</sub>B<sub>20</sub> metallic glasses”. In: *J. Mat. Sci.* 17 (1982), pp. 2677–2686.
- [44] M.N. Chandrasekhariah. *Magnetic properties and applications*. Trans Tech Publications, 1984.

- [45] D. Jiles. *Introduction to Magnetism and Magnetic Materials*. Chapman and Hall, 1991.
- [46] T.D. Shen, U. Harms, and R.B. Schwarz. “Bulk Fe-Based Metallic Glass with Extremely Soft Ferromagnetic Properties”. In: *J. Meta. Nano. Mats.* 13 (2002), pp. 441–446.
- [47] T.D. Shen, S.W. Xin, and B.R. Sun. “Low power loss in  $\text{Fe}_{65.5}\text{Cr}_4\text{Mo}_4\text{Ga}_4\text{P}_{12}\text{B}_{5.5}\text{C}_5$  bulk metallic glasses”. In: *J. Alloy. Compd.* 658 (2016), pp. 703–708.
- [48] J. Gyselinck, L. Vandeveldel, J. Melkebeek, P. Dular, F. Henrotte, and W. Legros. “Calculation of Eddy Currents and Associated Losses in Electrical Steel Laminations”. In: *IEEE Trans. Magn.* 35 (1999), pp. 703–708.
- [49] F.E. Luborsky. “Applications of Amorphous Alloys”. In: *IEEE Trans. Magn.* 14 (1978), pp. 1008–1012.
- [50] M. N. Chandrasekharaiah. *Metallic glasses: production, properties and applications*. Trans Tech Publications, 1984. Chap. Magnetic properties and applications.
- [51] S. Hatta, T. Egami, and C.D. Graham. “Amorphous Alloys with Improved Room-Temperature Saturation Induction”. In: *IEEE Trans. Magn.* 14 (1978), pp. 1013–1015.
- [52] J. Li, H. Men, and B. Shen. “Magnetic and corrosion properties of  $\text{Fe}_{56}\text{Co}_7\text{M}_2\text{Mo}_5\text{Zr}_{10}\text{B}_{20}$  (M = W or Ni) bulk metallic glasses”. In: *J. All. Com.* 422 (2006), pp. 28–31.
- [53] J. Li, H. Men, and B. Shen. “Soft-ferromagnetic bulk glassy alloys with large magnetostriction and high glass-forming ability”. In: *AIP Adv.* 1 (2011), pp. 042110-1–042110-7.
- [54] T.D. Shen, B.R. Sun, and S.W. Xin. “Effects of metalloids on the thermal stability and glass forming ability of bulk ferromagnetic metallic glasses”. In: *J. All. Com.* 631 (2015), pp. 60–66.
- [55] H.Y. Jung and S. Yi. “Enhanced glass forming ability and soft magnetic properties through an optimum Nb addition to a Fe-C-Si-B-P bulk metallic glass”. In: *Intermet.* 18 (2010), pp. 1936–1940.
- [56] B. Shen, M. Akiba, and A. Inoue. “Excellent soft-ferromagnetic bulk glassy alloys with high saturation magnetization”. In: *Appl. Phys. Lett.* 88 (2006), pp. 131907-1–131907-3.
- [57] Z. Long, Y. Shao, G. Xie, P. Zhang, B. Shen, and A. Inoue. “Enhanced soft-magnetic and corrosion properties of Fe-based bulk glassy alloys with improved plasticity through the addition of Cr”. In: *J. All. Com.* 462 (2008), pp. 52–59.

- [58] F.L. Kong, C.T. Chang, A. Inoue, E. Shalaan, and F. Al-Marzouki. “Fe-based amorphous soft magnetic alloys with high saturation magnetization and good bending ductility”. In: *J. All. Com.* 615 (2014), pp. 163–166.
- [59] X. Li, Y. Zhang, H. Kato, A. Makino, and A. Inoue. *Key Engineering Materials: The effect of Co addition on glassy forming ability and soft magnetic properties of Fe-Si-B-P bulk metallic glass*. Trans Tech Publications, 2012.
- [60] C. Chang, T. Kubota, A. Makino, and A. Inoue. “Synthesis of ferromagnetic Fe-based bulk glassy alloys in the Fe–Si–B–P–C system”. In: *J. All. Com.* 473 (2006), pp. 368–372.
- [61] J. Goodenough. “Summary of Losses in Magnetic Materials”. In: *IEEE Trans. Magn.* 38 (2002), pp. 3398–3408.
- [62] H.J. Williams, W. Shockley, and C. Kittel. “Studies of the Propagation Velocity of a Ferromagnetic Domain Boundary”. In: *Phys. Rev.* 80 (1950), pp. 1090–1094.
- [63] G. Bertotti. “General Properties of Power Losses in Soft Ferromagnetic Materials”. In: *IEEE Trans. Magn.* 24 (1988), pp. 621–630.
- [64] R.C. O’Handley, R. Hasegawa, R. Ray, and C.-P. Chou. “Ferromagnetic properties of some new metallic glasses”. In: *Appl. Phys. Lett.* 29 (1976), pp. 330–332.
- [65] M.D. Demetriou, G. Kaltenboeck, J. Suh, G. Garrett, M. Floyd, C. Crewdson, D.C. Hofmann, H. Kozachkov, A. Wiest, J.P. Schramm, and W.L. Johnson. “Glassy steel optimized for glass-forming ability and toughness”. In: *Appl. Phys. Lett.* 95 (2009), pp. 041907-1–041907-3.
- [66] J.H. Na, M. Floyd, D. Lee, M.D. Demetriou, W.L. Johnson, and G. Garrett. *Melt Overheating Method for Improved Toughness and Glass-Forming Ability of Metallic Glasses*. US Patent US 2014/0202596 A1, 7/24/14.
- [67] M.D. Demetriou, M. Floyd, C. Crewdson, J.P. Schramm, G. Garrett, and W.L. Johnson. “Liquid-like platinum-rich glasses”. In: *Scripta Mat.* 65 (2011), pp. 799–802.
- [68] P.K. Liao and K.E. Spear. *Binary Alloy Phase Diagrams*. ASM International, 1990.
- [69] L. Pauling. “Atomic Radii and Interatomic Distances in Metals”. In: *J. Am. Chem. Soc.* 69 (1947), pp. 542–553.
- [70] A. Takeuchi and A. Inoue. “Classification of Bulk Metallic Glasses by Atomic Size Difference, Heat of Mixing and Period of Constituent Elements and Its Application to Characterization of the Main Alloying Element”. In: *Mat. Trans.* 46 (2005), pp. 2817–2829.

- [71] K. Hoselitz. “Magnetic properties of iron-boron-silicon metallic glasses”. In: *J. Mag. Mag. Mat.* 20 (1980), pp. 201–206.
- [72] F. Luborsky, J.J. Becker, and R.O. McCary. “Magnetic Annealing of Amorphous Alloys”. In: *IEEE Trans. Mag.* 11 (1975), pp. 1644–1649.
- [73] J. Schroers. “Processing of Bulk Metallic Glass”. In: *Adv. Mat.* 22 (2010), pp. 1566–1094.
- [74] P. Williams. “Secondary Ion Mass Spectroscopy”. In: *Annu. Rev. Mater. Sci.* 15 (1985), pp. 517–548.
- [75] M. Riedel, H. Gnaser, and F.G. Ruclenauer. “Comparison of Secondary Ion Yield Data from Amorphous and Polycrystalline Iron-Based Alloys”. In: *Anal. Chem.* 54 (1982), pp. 290–294.
- [76] S.D. Norem, M.J. O'Neill, and A.P. Gray. “The use of magnetic transitions in temperature calibration and performance evaluation of thermogravimetric systems”. In: *Thermo. Acta.* 1 (1970), pp. 29–38.
- [77] D. Lynch. “Winning the global race for solar silicon”. In: *JOM* 61 (2009), pp. 41–48.
- [78] A. Inoue, N. Nishiyama, and T. Matsuda. “Preparation of bulk glassy Pd<sub>40</sub>Ni<sub>10</sub>Cu<sub>30</sub>P<sub>20</sub> alloy of 40 mm in diameter by water quenching”. In: *Mat. Trans., JIM* 37 (1996), pp. 181–184.
- [79] S. Kim, M.D. Demetriou, and W.L. Johnson. *Tough Iron-Based Bulk Metallic Glass Alloys*. US Patent US8,911,572 B2, 5/07/14.
- [80] E.J. Vinarcik. *High Integrity Die Casting Processes*. John Wiley and Sons, 2002.
- [81] A. Wiest, J.S. Harmon, M.D. Demetriou, R.D. Conner, and W.L. Johnson. “Injection molding metallic glass”. In: *Scripta Mat.* 60 (2009), pp. 160–163.
- [82] W.L. Johnson, M.D. Demetriou, C.P. Kim, and J.P. Schramm. *Forming of metallic glass by rapid capacitor discharge*. US Patent US 8613813 B2, 5/07/14.
- [83] B. Shen and A. Inoue. “Superhigh strength and good soft-magnetic properties of (Fe,Co)–B–Si–Nb bulk glassy alloys with high glass-forming ability”. In: *App. Phys. Lett.* 85 (2004), pp. 4911–4913.
- [84] F. Hosseinzadeh, A.H. Mahmoudi, C.E. Truman, and D.J. Smith. “Prediction and Measurement of Through Thickness Residual stresses in Large Quenched Components”. In: *Proc. World Cong. Eng.* 2 (2009), pp. 1526–1531.
- [85] H. Kato, H.S. Chen, and A. Inoue. “Relationship between thermal expansion coefficient and glass transition temperature in metallic glasses”. In: *Scripta Mat.* 58 (2008), pp. 1106–1109.

- [86] K.V. Namjoshi, J.D. Lavers, and P.P. Biringer. “Eddy-Current Power Loss in Toroidal Cores with Rectangular Cross Section”. In: *IEEE Trans. Mag.* 34 (1998), pp. 636–641.
- [87] M.T. Kakhki, J. Cros, and P. Viarouge. “New Approach for Accurate Prediction of Eddy Current Losses in Laminated Material in the Presence of Skin Effect With 2-D FEA”. In: *IEEE Trans. Mag.* 52 (2016), pp. 6300604–6300607.
- [88] M.T. Kakhki, J. Cros, and P. Viarouge. “Fe<sub>76</sub>Si<sub>9.6</sub>B<sub>8.4</sub>P<sub>6</sub> glassy powder soft-magnetic cores with low core loss prepared by spark-plasma sintering.pdf”. In: *Mat. Sci. Eng. B* 176 (2011), pp. 1247–1250.
- [89] T. Kulik, H. Matyja, and B. Lisowski. “Influence of Annealing on Magnetic Properties of Co-based Metallic Glasses”. In: *J. Mag. Mag. Mat.* 43 (1984), pp. 135–142.
- [90] H.S. Chen, S.D. Ferris, E.M. Gyorgy, H.J. Leamy, and R.C. Sherwood. “Field heat treatment of ferromagnetic metallic glasses”. In: *Appl. Phys. Lett.* 26 (1975), pp. 405–406.
- [91] F. Bralsford. *Magnetic Materials*. John Wiley and Sons, 1948.
- [92] B. Poston and D. Smith. “Massive Valley blackout again puts spotlight on L.A.’s failing infrastructure”. In: *Los Angeles Times* (2017, July 10).
- [93] *Energy Conservation Program for Commercial Equipment: Distribution Transformers Energy Conversion Standards; Final Rule*. Tech. rep. 10 CFR Part 431. Federal Register, Vol. 72, No. 197, 58189, Oct. 2007.
- [94] J.G. Webster, ed. *Electrical Measurement, Signal Processing, and Displays*. CRC Press, 2003.
- [95] *Standard Test Method for Density of Glass by Buoyancy*. Tech. rep. ASTM. C 693-93, 2003.
- [96] S. Takayama. “Drawing of Pd<sub>77.5</sub>Cu<sub>6</sub>Si<sub>16.5</sub> Metallic Glass Wires”. In: *Mat. Sci. Eng.* 38 (1979), pp. 41–48.
- [97] T. Masumoto, I. Ohnaka, A. Inoue, and M. Hagiwara. “Production of Pd-Cu-Si Amorphous Wires by Melt Spinning Method using Rotating Water”. In: *Scripta Met.* 15 (1981), pp. 293–296.
- [98] P.T. Squire, D. Atkinson, M.R.J. Gibbs, and S. Atalay. “Amorphous wires and their applications”. In: *J. Mag. Mag. Mat.* 132 (1994), pp. 10–21.
- [99] A.O. Olofinjana and H.A. Davies. “Determination of the static and dynamic mechanical properties of Fe-Cr-Si-B metallic glass wire”. In: *Mat. Sci. Eng.* 186 (1994), pp. 143–149.
- [100] A.O. Olofinjana, J.H. Kern, and H.A. Davies. “Effects of process variables on the multi-strand casting of high strength sub-millimetre metallic glass wire”. In: *J. Mat. Proc. Tech.* 155 (2004), pp. 1344–1349.

- [101] “Engel”. In: <https://www.engelglobal.com/en/at.html> (Accessed: 2017-07-17).
- [102] Q. An, K. Samwer, M.D. Demetriou, M.C. Floyd, D.O. Duggins, W.L. Johnson, and W.A. Goddard. “How the toughness in metallic glasses depends on topological and chemical heterogeneity”. In: *Proc. Nat. Acad. Sci.* 113 (2016), pp. 7053–7058.

## INDEX

### A

Alloy Development, 10, 36

Amorphous Wires, 106

### B

bibliography, 119

### C

Casting Box, 71

Commercialization, 7

Conclusion, 104

Contributions, 34

Cusps, 13

### E

Eddy Currents, 24

Electric Discharge Machining, 81

Equations, xviii

### F

Ferromagnetism, 17

Figures, xvi

Fluxing, 54

### H

Hysteresis Curve, 50, 79

### I

Injection Molding, 71

### M

Magnetic Annealing, 87, 102

Magnetic Measurements, 83

Magnetostriction, 75

Max Magnetization, 100

Mechanical Properties, 109

Metglas, 2, 7

Modeling, 111

N

Nomenclature, xxi

O

Optimal Thickness, 90, 98, 99

Overheating, 41

Q

Quenched-in Stresses, 76

Quenching, 39

S

Silicon-Steel, 91

Stress Annealing, 75

T

Table of Contents, xi

Tables, xvii

Transformers, 26